

Master's thesis

Rashad Naghiyev

Elastic anisotropy prediction using wellbore velocity measurements

Master's thesis in Petroleum Geophysics

Supervisor: Kenneth Duffaut

June 2022

NTNU
Norwegian University of Science and Technology
Faculty of Engineering
Department of Geoscience and Petroleum

Rashad Naghiyev

Elastic anisotropy prediction using wellbore velocity measurements

Master's thesis in Petroleum Geophysics
Supervisor: Kenneth Duffaut
June 2022

Norwegian University of Science and Technology
Faculty of Engineering
Department of Geoscience and Petroleum

Abstract

Every day the world is evolving, new knowledge, new views are introduced. Developing better techniques for enhancing exploration, production, and discovery of energy sources has been in the limelight for the industry. For these purposes, it is necessary to ensure that the reservoir is characterized and modeled as realistic as possible. The subsurface is understood and studied by means of seismic wave propagations, so interpreting the wave response as precisely as possible will shape how the reservoir is described. Since the breakthrough of subsurface characterization, the Earth has been modeled as an elastically isotropic medium, meaning that the properties of the medium do not vary depending on the direction of propagation. However, it is broadly accepted that this theory is not always true, and the medium is highly dependent on which direction it is studied (Armstrong et al. 1994). This has introduced a famous theory of elastic anisotropy. The elastic anisotropy is more pronounced in the velocities of the medium. The elastic anisotropy suggests that the wave can travel at different velocities in different directions depending on the medium's elasticity. Considering a medium being isotropic or anisotropic affects all the practical applications from interpretation to processing. Although the assumption of elastic anisotropy has a great influence, the application of elastic anisotropy is a difficult task to do. In this respect, Thomsen 1986's research has thoroughly described elastic anisotropy. Thus, in order to define elastic anisotropy, one would need three small quantities called Thomsen parameters ϵ , γ , δ that are dependent on horizontal and vertical components of velocities. Generally, in conventional well logging where the subsurface information is acquired, the measurements are performed vertically. Because of the lack of horizontal (for ϵ and γ) and diagonal (for δ) measurements, it is not possible to generate anisotropic information (ϵ , γ , δ) logs. Although the empirical methods have been suggested by other authors, their performance and background theory do not suffice them to be accepted as reliable methods. This thesis suggests a new model of generating anisotropic information logs considering the theoretical factors. Because the model is based on P- and S-wave propagation, the practical elements have also been included. The model has been verified using the three adjacent wells (well 7220/8-1, well 7220/7-1, and well 7220/10-1) in the Barents Sea. A reliable reference γ has been extracted by combining Norris 1990's theory and Sonic Scanner measurements available in the wells. The verification references for ϵ and δ have been obtained from Walk-Away Vertical Seismic Profiling (WAVSP). Because WAVSP is only available in well 7220/8-1, the verification in well 7220/7-1 and well 7220/10-1 has only been done using γ . The validation has shown encouraging results. For further analysis, the forward seismic modeling for each well has been performed considering isotropic and anisotropic media. Based on the synthetic seismic data, AVO/AVA responses have been analyzed, and the results have shown an anisotropic effect in mid-to-far angles. Overall results of this thesis have verified the proposed anisotropy prediction model. Thus, this model can be applied in order to introduce elastic anisotropy into subsurface models.

Hver dag utvikler verden seg, nye kunnskaper, nye synspunkter introduseres. Utvikling av eksisterende teknikker for å forbedre leting, produksjon og oppdagelse av energikilder er sentalt for industrien. For disse formålene er det nødvendig å sikre at reservoaret karakteriseres og modelleres så realistisk som mulig. Undergrunnen blir undersøkt og studert ved bruk av seismisk bølgeforplantning og tolkning av seismisk respons er viktig for å oppnå en nøyaktig beskrivelse av undergrunnen og reservoarer. En karakterisering av undergrunnen gjennom en antagelse om at lagene er elastisk isotrope er overforenkelet. Det er imidlertid bredt akseptert i forskning og industrien at denne antakelsen ikke alltid er gyldig, men heller at lagenes elastiske egenskaper er svært retningsavhengig. Lagenes elastiske anisotropi medfører at bølgene propagerer med retningsavhengige hastigheter. Om å vurdere om et medium er isotropt eller anisotropt påvirker alle praktiske steg i prosesseringen og tolkningen av seismiske data. Selv om antagelsen om elastisk anisotropi har stor innflytelse, er elastisk anisotropi parameter kostbare og vanskelig å måle og samle inn. Thomsen (1986) presenterte en grundig beskrivelse av elastisk anisotropi for undergrunnen. For å definere elastisk anisotropi ved antagelsen om et trancers isotropt medium vil man således trenge tre parametre, ϵ , γ , δ (Thomsen parametre) som er avhengige av horisontale og vertikale komponenter av hastigheter. Som regeli konvensjonell brønnlogging måles undergrunnsegenskaper vertikalt i brønner. I fravær av mangelhorisontale målinger er det ikke mulig å beregne anisotropien ϵ , γ , δ ved bruk av hastighetslogger. Empiriske og teoretiske metodene har blitt foreslått gjennom publikasjoner, er deres ytelse eller teoretiske kompleksitet ikke tilstrekkelig eller for komplekse å benytte. Denne oppgaven foreslår en ny bergartsmodell til å prediktere anisotropilogger ved bruk av hastighetslogger målt i vertikal retning. Fordi modellen er basert på P- og S-bølgeutbredelse, er de praktiske elementene også tatt med. Verifikasjonen av modellen er utført ved bruk av de tre tilstøtende brønnene (brønn 7220/7-1, brønn 7220/8-1, brønn 7220/10-1) i den norske delen av Barentshavet. Ved å kombinere en teoretisk modell for rørbølger med Sonic Scanner-loggemålinger tilgjengelig i brønnene, gir dette oss en pålitelig referanse γ til å kvalifisere modellprediksjonene. Verifikasjonsreferansene for Thomsen's ϵ og δ er hentet fra Walk-Away Vertikal Seismisk Profiering (WAVSP). Fordi WAVSP kun er tilgjengelig i brønn 7220/8-1, har verifisering i brønn 7220/7-1 og brønn 7220/10-1 kun blitt utført mot Thomsen γ parameter estimert fra sonic scanner data. Valideringen har vist oppmuntrende resultater. For videre analyse er den fremre seismiske modelleringen for hver brønn utført med tanke på isotrope og anisotrope medier. Basert på de syntetiske seismiske dataene er AVO/AVA-responser analysert, og resultatene har vist anisotropisk effekt i vinkler fra midten til langt. Samlede resultater av denne oppgaven har bekreftet den foreslåtte anisotropi prediksjonsmodellen. Dermed kan denne modellen brukes for å introdusere elastisk anisotropi i undergrunnsmodeller.

Preface

This MSc. thesis contains the results and discussions of the research in elastic anisotropy prediction within Petroleum Geophysics master's degree at the Norwegian University of Science and Technology (NTNU). The desire for this study has come from my long-time appetite of contributing to the science world to practically overcome some challenges such as those associated with elastic anisotropy. The need for the study was realized after the specialization project "A review of models for wellbore elastic anisotropy analysis" conducted in the autumn semester. I would have never reached the point of completing my master's degree with such a thesis without extensive support and help.

These two years of master's education have been a challenging period of my life with lots of ups and downs. Starting a master's degree during an outbreak of the corona pandemic, where most of the studying has been conducted online had been a sometimes exciting and sometimes depressing experience for me. Fortunately, I was not alone during this time. Being accompanied by highly skilled and experienced professors who are always eager to teach, coach, and motivate was a great opportunity that I am grateful for. I would like to thank Alexey Stovas, Rune Martin Holt, Børge Arntsen, Erik Skogen, Carlos Alberto Aizprua Luna, Arve Næss, and many others who have helped and supported me during this period of my life.

One of the most influential people who supported me during my specialization project and master's thesis was my supervisor, Kenneth Duffaut. I want to express my gratitude for his patience and guidance during last year. The idea that shapes this master's thesis belongs to him, and I am grateful to him for relying on me, sharing this innovative idea, and allowing me to be a part of this innovation. I would also like to thank him for always being there for me, especially for understanding and moral support during stressful periods. During our meetings, he and I shared our thoughts in an open environment where every idea was heard and assessed. I am grateful to Kenneth Duffaut for his readiness to assist me in every obstacle I encounter.

Special thanks go to Erik Skogen and Michinori Asaka for their insightful comments and suggestions during informal meetings.

I would also love to thank my colleagues and friends, Joxongir Khayrullayev, Carlos Alexandre Pereira de Macedo, and Karl Jørgen, for our daily talks, sharing ideas and thoughts, and fun times. Debating the functionality with them gave me new ideas for further steps.

I also owe deep gratitude to my family: my mother, Aytan, my father, Rafael, and my sister, Narmin, who have always supported and motivated me unconditionally. Undoubtedly, my girlfriend, Aygul, deserves a special word of appreciation for her encouragement, emotional support, and love.

Finally, I would like to thank the Norwegian University of Science and Technology for bringing me valuable learning opportunities, enabling me to embark on a new platform and start a new life!

I hope you will enjoy reading!

Rashad Naghiyev.

Trondheim, June 16, 2022.

Table of Contents

Abstract.....	1
Preface	3
Table of Figures.....	6
Abbreviations	10
Introduction	14
Chapter 1. Theory	16
1.1. The basics of anisotropy	16
1.2. Weak Anisotropy.....	20
1.3. Physical causes.....	24
1.4.1. Intrinsic Anisotropy.....	24
1.4.2. Stress-induced anisotropy	24
1.4.3. Layer-induced anisotropy	28
Chapter 2. Model	31
2.1. Vertical P-wave propagation and influencing factors.....	32
2.2. Vertical S-wave propagation and influencing factors	35
2.3. Last Thomsen parameter	37
2.4. Predicting elastic anisotropy in non-zero angles	39
Chapter 3. Supporting parametrization	40
3.1. Vertical stiffness coefficients	40
3.2. Horizontal-to-vertical stress ratio: K_0	43
3.3. Clay content V_{cl}	45
3.4. Implementation of the model.....	47
Chapter 4. Validation & Performance.....	47
4.1. Sonic Scanner	47
4.1.1. Gamma measurement	49
4.2. Walk-Away Vertical Seismic Profiling.....	50
4.3. Validation results	51
4.3.1. Well 7220/8-1	51
4.3.2. Well 7220/7-1	60
4.3.3. Well 7220/10-1	65
Chapter 5. Impact of anisotropy on seismic response.....	70

5.1. Forward seismic modelling	70
5.2. Amplitude-versus-angle analysis	72
5.3. Modelling and analysis results	73
Chapter 6. Discussion	81
A quick note on further works	86
Chapter 7. Conclusion	88
Acknowledgement	90
Appendices.....	91
A. Sayers 1999: Contribution of stress into the overall anisotropy	91
B. Li 2006's model and its theory.....	93
C. Propagation of error in proposed models	94
D. Zoeppritz equation.....	95
References	100

Table of Figures

Figure 1. Wave velocity equations.....	21
Figure 2. P-wavefront comparison (Thomsen 2014)	23
Figure 3. SEM image of clay - Intrinsic anisotropy (Sayers & den Boer 2019, Hornby et al. 1994)	24
Figure 4. Stress test. σ_V – vertical stress, σ_H – horizontal stress	25
Figure 5. Velocities (a) and ε (b) as a function of mean effective stress for shale sample, where the core plug is cut normal to bedding (Raven et al. 2011).	27
Figure 6. Layer – Induced Anisotropy (Hall 2016).	28
Figure 7. Layer-Induced anisotropy: a medium composed of finely layered isotropic layers (left) is equivalent to homogenous anisotropic medium with the symmetry axis normal to the layers (Grechka 2009).	29
Figure 8. P-wave propagation in clayey medium.....	34
Figure 9. SV-wave propagation in clayey medium.....	36
Figure 10. Estimation of V_{SV} (left). Red: Well measurement, Blue: Estimated V_S . Estimation of ρ (left). Red: Well measurement, Blue: Estimated ρ . Grey area is hydrocarbon filled reservoir	38
Figure 11. Estimation of V_{SV} (left). Red: Well measurement, Blue: Estimated V_S . Estimation of ρ (left). Red: Well measurement, Blue: Estimated ρ . Grey area is hydrocarbon filled reservoir	42
Figure 12. Volumetric rock volume (Ezekwe 2010).....	43
Figure 13. Comparison of clay content calculation from Spectroscopy log and Neutron-Density porosity method proposed by La Vigne 1994 using well 7220/8-1	46
Figure 14. Sonic Scanner tool provides axial, azimuthal and radial information from both the monopole and the dipole measurements for near-wellbore and far-field slowness information (Schlumberger, 2005). ...	48
Figure 15. Overview of well 7220/8-1. From left to right: Caliper (brown) & Bit size (black), Clay content (green), density porosity (black), Vertical P-wave velocity (orange), SV-wave velocity (dark green), Formation density (blue). Hydrocarbon zones are highlighted in gray.....	52
Figure 16. Well log data from 7220/8-1 including vertical stiffnesses (C_{33} and C_{44}). From left to right: Caliper (brown) & Bit size (black), Clay content (green), Density porosity (black), Vertical P-wave stiffness	

(C33) (orange), SV-wave stiffness (C44) (dark green), Formation density (blue). Hydrocarbon zones are highlighted in gray.	53
Figure 17. VSV analysis. VSV with polarization angle = 0° (red), VSV with polarization angle = 90° (green)	54
Figure 18. Well log data from 7220/8-1 including Stoneley wave and reference γ . From left to right: Caliper (brown) & Bit size (black), Clay content (green), Density porosity (black), Stoneley-wave velocity (red), Formation γ generated by Stoneley wave (blue). Hydrocarbon zones are highlighted in gray.	55
Figure 19. Vertical velocities (VP and VS) including data from Walkaway Vertical Seismic Profiling. VPV from well (1 st track, orange), VPV from WAVSP (1 st track, brown), VSV from well (2 nd track, green), VSV from WAVSP (2 nd track, brown). WAVSP ϵ (3 rd track, brown), WAVSP δ (4 th track, brown).....	56
Figure 20. Prediction results of well 7220/8-1. From left to right: Caliper (brown) & Bit size (black), Clay content (green), Density porosity (black), VP/VS ratio (light blue), γ , ϵ , δ . Hydrocarbon zones are highlighted in gray.	59
Figure 21. Overview of well 7220/7-1. From left to right: Caliper (brown) & Bit size (black), Clay content (green), density porosity (black), Vertical P-wave velocity (orange), SV-wave velocity (dark green), Formation density (blue). Hydrocarbon zones are highlighted in gray.....	61
Figure 22. Well log data from 7220/7-1 including vertical stiffnesses (C33 and C44). From left to right: Caliper (brown) & Bit size (black), Clay content (green), Density porosity (black), Vertical P-wave stiffness (C33) (orange), SV-wave stiffness (C44) (dark green), Formation density (blue). Hydrocarbon zones are highlighted in gray.	62
Figure 23. Well log data from 7220/7-1 including Stoneley wave and reference γ . From left to right: Caliper (brown) & Bit size (black), Clay content (green), Density porosity (black), Stoneley-wave velocity (red), Formation γ generated by Stoneley wave (blue). Hydrocarbon zones are highlighted in gray.	63
Figure 24. Prediction results of well 7220/7-1. From left to right: Caliper (brown) & Bit size (black), Clay content (green), Density porosity (black), VP/VS ratio (light blue), γ , ϵ , δ . Hydrocarbon zones are highlighted in gray.	64
Figure 25. Overview of well 7220/10-1. From left to right: Caliper (brown) & Bit size (black), Clay content (green), density porosity (black), Vertical P-wave velocity (orange), SV-wave velocity (dark green), Formation density (blue). Hydrocarbon zones are highlighted by gray.....	66
Figure 26. Well log data from 7220/10-1 including vertical stiffnesses (C33 and C44). From left to right: Caliper (brown) & Bit size (black), Clay content (green), Density porosity (black), Vertical P-wave stiffness	

(C33) (orange), SV-wave stiffness (C44) (dark green), Formation density (blue). Hydrocarbon zones are highlighted by gray.	67
Figure 27. Well log data from 7220/7-1 including Stoneley wave and reference γ . From left to right: Caliper (brown) & Bit size (black), Clay content (green), Density porosity (black), Stoneley-wave velocity (red), Formation γ generated by Stoneley wave (blue). Hydrocarbon zones are highlighted by gray.	68
Figure 28. Prediction results of well 7220/10-1. From left to right: Caliper (brown) & Bit size (black), Clay content (green), Density porosity (black), VP/VS ratio (light blue), γ , ε , δ . Hydrocarbon zones are highlighted by gray.	69
Figure 29. A process of convolution.....	71
Figure 30. 40 Hz Ricker wavelet	71
Figure 31. AVO analysis: Dependence of P-wave reflection coefficient on angle at 4 AVO classes (Rutherford & Williams 1989, Ross & Kinman 1995) (figure courtesy Duffaut & Holt, 2021).....	73
Figure 32. AVO classification: Intercept – Gradient crossplot Rutherford & Williams 1989 and Castagna & Swan 1997.....	73
Figure 34. Behavior of the VP/VS and ZP in sand-shale pack	75
Figure 33. A comparison panel between isotropic and anisotropic synthetic seismic data in well 7220/8-1.	74
Figure 35. AVA responses of well 7220/8-1: top left – response from clay-to-sand boundaries, top right – response from sand-to-clay boundaries, bottom – response from clay-to-clay boundaries.	76
Figure 36. A comparison panel between isotropic and anisotropic synthetic seismic data in well 7220/7-1.	77
Figure 37. AVA responses of well 7220/7-1: top left – response from clay-to-sand boundaries, top right – response from sand-to-clay boundaries, bottom – response from clay-to-clay boundaries.	78
Figure 38. A comparison panel between isotropic and anisotropic synthetic seismic data in well 7220/10-1.	79
Figure 39. AVA responses of well 7220/10-1: top left – response from clay-to-sand boundaries, top right – response from sand-to-clay boundaries, bottom – response from clay-to-clay boundaries.	80

- Figure 40. Comparison of prediction results for well 7220/7-1. From left to right: Caliper (brown) & Bit size (black), Clay content computed by ECS log (green), Density porosity (black), γ . Hydrocarbon zones are highlighted by gray. 84
- Figure 41. Prediction results of well 7220/7-1. From left to right: Caliper (brown) & Bit size (black), Clay content by ECS log (green), Density porosity (black), VP/VS ratio (light blue), γ , ε , δ . Hydrocarbon zones are highlighted by gray. 85
- Figure 42. A schematic view of two spheres with a radius R . A deformation has been seen at their contact subjected by contact forces and displacement during compression tests done by Hertz 1882 (normal compression, FN) and Mindlin 1949 (tangential compression, FT)..... 86
- Figure 43. The effect of anisotropy on stress-stiffness relationship. In the isotropic case, Hertz-Mindlin contact theory have results $1/3$ dependency (red line). The blue line is when anisotropy is added in the form of Vcl 87

Abbreviations

$A^{(r)}$ – area of contact plane

AVO/AVA – Amplitude versus offset/angle

$B_T^{(r)}$ – shear compliances at r-th contact

$B_N^{(r)}$ – normal compliances at r-th contact

CBW – clay bound water

C_P – coordination number

C_{66}^* – effective stiffness from Stoneley wave

C_{ij} – stiffness matrix of a material

C_{ijkl} – stiffness tensor of a material

ECS – elemental capture spectroscopy

f – volume fraction of the logging tool occupies the borehole

f_{Dom} – dominant frequency

f_T – volume fraction of inner part of the logging tool

G – rigidity – shear modulus

G – shear modulus of solid sphere

GOC – gas-oil contact

GR – gamma ray

K – incompressibility – bulk modulus

K_0 – horizontal-to-vertical stress ratio

K_{BF} – bulk modulus of borehole fluid

M_F – formation stiffness

M_H – a modulus in vertical direction

M_T – logging tool's stiffness

M_V – a modulus in horizontal direction

$n_i^{(r)}$ – i-th component of unit normal to r-th contact,

NPD – Norwegian Petroleum Directorate

OWC – oil-water contact

TH – thorium

t – temporal component

S_{ijkl} – compliance tensor of a material

u – velocity

x – spatial component

VTI – vertically transverse isotropy

V_{NMO} – Normal moveout velocity

V_P – P-wave velocity

V_{P0} – vertical P-wave velocity

$V_{Pquartz}$ – P-wave velocity of quartz

V_{Pwat} – water velocity

V_{S0} – vertical S-wave velocity

V_{SH} – SH-wave velocity

V_{SV} – SV-wave velocity

$V_{Squartz}$ – S-wave velocity of quartz

$V_{Stoneley}$ – Stoneley wave velocity

V_{cl} – clay volume of the rock

V_{min} – minimum velocity

$V_{non-clay}$ – non-clayey volume of the rock

V_{sh} – shale volume of the rock

V_{silt} – silt volume of the rock

W_{cl} – clay content weight fraction

W_{200} – orientation distribution function coefficient

W_{400} – orientation distribution function coefficient

Z_P – acoustic impedance

α_{ij} – second-rank tensor

β_{ijkl} – forth-rank tensor

$\hat{\gamma}$ – predicted γ

γ – Thomsen anisotropic parameter

$\hat{\varepsilon}$ – predicted ε

ε – Thomsen anisotropic parameter

λ_{Dom} – dominant wavelength

μ_T – shear modulus of elastic shell in logging tool

ν – Poisson ratio

ν_s – Poisson ratio of solid sphere

ν_T – Poisson's ratio of elastic shell in logging tool

ρ – density

ρ_{BF} – density of borehole fluid

ρ_{clay} – matrix density

ρ_{fluid} – fluid density

ρ_{log} – formation density reading

ρ_{mat} – matrix density

σ' – net stress

σ_h – horizontal stress

σ'_h – effective horizontal stress

σ_V – vertical stress

σ'_V – effective vertical stress

σ_{ij} – stress of the material

σ_m – mean stress

ε_{ij} – strain of the material

ε_{33} – strain in the vertical direction at P-wave propagation

ε_h – strain in the horizontal direction

ε_V – strain in the vertical direction

ϕ – porosity

ϕ_D – density porosity

ϕ_N – neutron porosity

ϕ_{N-clay} – neutron porosity in clay

ϕ_T – total porosity

δ – Thomsen anisotropic parameter

δ_{ij} – Kronecker delta

η – anellipticity

λ – Lamé parameter

μ – Lamé parameter

Introduction

Advances in the last half century made us accept the phenomenon called elastic anisotropy. Nowadays, it is broadly accepted that elastic isotropy, which assumes that the waves propagate at the same speed in all directions, is not always true (Armstrong et al. 1994). The waves can travel at different speeds in different directions, which supports the anisotropic medium theory. The medium being isotropic or anisotropic depends on the elasticity of the medium. Although the findings of numerous scientific research have confirmed that the propagation of waves in the solids should be described by more complex functions or parameters, the oil and gas industry chose to ignore the existence of anisotropy, relying on the fact that the effect is negligible. Because the processing of data considering isotropy was already not easy, the assumption of anisotropy should have been justified by a good reason to avoid the cost of complications. The main obstacle to not considering an anisotropic media is that the elastic coefficients which fully describe the anisotropy are not easy to obtain (Bhuiyan & Holt 2016). Although the effect was considered negligible, the errors encountered, which cannot be explained in the past, arose from disregarding elastic anisotropy. For example, the difficulties in achieving reliable well-to-seismic ties were due to the errors from wrong time-to-depth conversions, which have been purely influenced by taking no notice of elastic anisotropy (Okorie et al. 2016). Thus, we can confidently say that anisotropy significantly affects seismic processing and interpretation. So, in order to enhance subsurface description and successfully image the subsurface, we need detailed information about wave propagation behavior through strata as realistic as possible (Hornby et al. 2003). That's why the anisotropy is required to improve seismic imaging, processing, interpretation like 4D seismic, quantitative amplitude versus offset (AVO) interpretation, and pre-stack seismic modeling (Bhuiyan & Holt 2016, Hornby et al. 2003, Li & Pickford 2002), and the quality of pre-stack seismic analysis for ray tracing, amplitude analysis, and rock property inversion (Li & Xu 2001, Alkhalifah & Rampton 2001). In addition, Larner 1993 and Larner & Cohen 1993 discuss that anisotropy may also have a direct influence on the migration of seismic reflection profiles. It can also be a reliable lithology diagnostic in reservoir description (Jones & Wang 1981, Byun et al. 1989, Vernik & Nur 1992). Especially for deviated wells in offshore fields, the analysis mentioned above can yield in totally unrealistic results if isotropy is considered.

The type of rock in the elastic medium is one of the bullet points when estimating anisotropy. The research shows that not all types of rocks indicate a higher degree of anisotropy, so, having a full control on rock types, it is possible to acquire a general trend of elastic anisotropy. Li 2006 suggests that two main factors can affect the anisotropy in the rock: the volume of clay and the degree of compaction. The volume of clay constitutes the physical basis of elastic anisotropy (intrinsic). It purely depends on the clay platelets in the rock (Li 2006), so it is not affected by any external processes. On the other hand, compaction is in itself an external force. It makes the minerals align in a preferred direction depending on which direction it is applied. It eventually decreases the porosity while increasing the velocity in the direction of compaction (Li 2006). This introduces a difference in velocities in different directions, so velocity anisotropy. As an example,

we can take a look at unconsolidated ocean bottom deposits (Li 2006). Li 2006 discusses that they can show very little or no indication of anisotropy even though they have high clay content. Because the platelets align in the perpendicular direction to stress during the compaction, the velocity becomes higher in the direction of bedding forms. Sayers 1994's work proved that the compaction could be calculated by W_{200} and W_{400} ** orientation distribution function coefficients. Additionally, the research done by Wang 2002 shows that if the rock is unfractured such as clay-free massive reservoir sands, it can be assumed as isotropic rock, yet a sandstone containing a large amount of authigenic clays will become intrinsically anisotropic. Research also shows that the anisotropic effect of detrital clays is not significant as they fill in the pores (Wang 2002). Carbonate rocks behave isotropic as long as they become fractured or finely layered. Normally, reservoir carbonate rocks do not show an obvious layering, that's why they can be treated as isotropic for seismic processing and interpretation (Wang 2002). Nevertheless, assuming isotropy for the rock types like shale is not a good idea. Shales mainly consist of clay minerals, and clay minerals have an intensely layered structure. This structure results in a large elastic anisotropy because of the existence of strong covalent bonds within layers and weaker electrostatic bonds between layers (Sayers & den Boer 2016). Wang 2002 also supports that the anisotropy of shale is dependent on compaction history and the type of clay in the shale. Overall, in order to consider the rock types, the degree of compaction, the clay content, and the type of clay in the rock, as well as the secondary factors such as porosity, need to be closely investigated.

Because the shales are highly anisotropic compared to other types of rocks, overlooking elastic anisotropy in shales can cause severe problems in analysis. As we know, shales are an essential part of most hydrocarbon reservoirs because it works as seal rock. Additionally, from the well logs, we know that most parts of the sedimentary basins are actually shales. Generally, the elastic properties of shales are assumed anisotropic (Miller & Chapman 1991, Vernik & Nur 1992, Kaarsberg 1958, McDonal et al. 1958, Banik 1984, Jones & Wang 1981, Lo et al. 1989, Tosaya & Nur 1989, White et al. 1989, Winterstein & Paulsson 1990, Hornby et al. 1994, Johnston & Christensen 1995). The recent growth of interest in the exploration and exploitation of unconventional shale/gas reservoirs like the Bakken, Barnett, Fayetteville, Haynesville, Marcellus, Wolfcamp, and Woodford increased the importance of shale anisotropy than that before (Horne 2013, Sayers & den Boer 2019). Also, shales can be a host lithologies for radioactive waste repositories and natural seals in CO₂ geo-sequestration projects.

Although there has been a half-century of research on the elastic properties of shales, they are not well-understood, often because of poorly preserved samples or time-consuming laboratory tests because of the low permeability of shales (Raven et al. 2011). In order to estimate elastic properties of shales, first, we have to estimate the elastic properties of clay. Yet, the laboratory experiments show that the reliable moduli of pure clay crystals are difficult to obtain, considering the technical difficulties caused by the small grain size of crystals (Sayers & den Boer 2020). The

** these coefficients are only valid for VTI medium, in a more complicated medium, more coefficients need to be introduced

studies done by Rothbauer 1971, Tosaya 1982, Katahara 1996 suggest that it is possible to assume the moduli of mica muscovite and the illite (the most abundant clay type) as the same due to the similarities in the crystallographic structures and compositions. Also, the moduli of muscovite have already been experimentally known (Alexandrov & Ryzhova 1961, Vaughan & Guggenheim 1986, McNeil & Grimsditch 1993). There have been few attempts to fully estimate the elastic properties of shale, yet a solid theoretical background is still under discussion.

Therefore, the elastic anisotropy estimation is a crucial part of the seismic analysis. As Thomsen's 1986 study discusses, estimating anisotropy has to be done through the elastic properties of rocks. That's why scientists have conducted a vast amount of research on anisotropy, elastic properties of rocks, as well as the means of modeling the anisotropy. For this purpose, my specialization paper (Naghiyev, 2021) focuses on the performances of some prominent, cost-effective, and easy-to-use anisotropy prediction models in the literature. The work has concluded that when compared with the reference measurements, the best representative model for γ and ε is the study done by Li 2006. For the third anisotropic parameter, Li 2006 has used a rough linear dependency between δ and ε . Although Li 2006's δ estimation is based on pure linear relation ($\delta = 0.32\varepsilon$), in practice, it performs reasonably well when compared Walk-Away Vertical Seismic Profiling data.

Even though based on Naghiyev 2021, the performance of some models is pretty good, the three classical anisotropy causes were not outlined. The best model – Li 2006's model assumes only intrinsic anisotropy, and layer-induced anisotropy was added through Backus theory. Thus, stress-induced anisotropy was missing. Now, in the light of Naghiyev 2021, this master thesis takes a further step and introduces a model that also considers stress-induced anisotropy. This model is also theoretically more advanced than previous equivalents because its basics rely on practical applications. The model has been validated using well 7220/8-1, well 7220/7-1, and well 7220/10-1. A representative γ measurement is acquired by Norris 1990's Stoneley wave assumption using Sonic Scanner data. The ultimate goal of this thesis is to generate anisotropic information logs (ε , γ and δ) which are not easily accessible from conventional logging tools. Additionally, prediction results have been used in a forward seismic modeling scheme. Using synthetic seismic sections assuming an isotropic and anisotropic media and extracting AVO/AVA responses have benefitted to practically proving the effect of elastic anisotropy. It will also underline the importance of anisotropy by comparing anisotropic and isotropic sections. The results will be discussed in further chapters.

Chapter 1. Theory

1.1. The basics of anisotropy

In order to start to work with anisotropy, first, it is necessary to understand what we mean by "anisotropy" in practice; therefore, its theory needs to be explored. For a detailed treatment of anisotropy, readers are referred to the work of Thomsen 1986, which is one of the fundamental

studies characterizing elastic anisotropy. This paper is the one of the first works that fully explain the anisotropy in most cases of interest and discusses its application.

In general, elastic anisotropy is caused by the waves (elastic or seismic) traveling in different directions with different velocities. So, our focus is to obtain how the waves travel, which brings us to define the motion of the waves. In order to understand wave motion, we start with Newton's Second Law of Motion. Equation 1.1 illustrates Second Law written in 3 D continuum. Note that each direction is represented by values 1, 2, 3 for x, y, z, respectively.

$$\rho \frac{\partial^2}{\partial t^2} u_i = \sum_j^{j=3} \frac{\partial}{\partial x_j} \sigma_{ij}$$

Equation 1.1

$u(x, t)$ is a displacement of a particle at time t and position x , and $\sigma(x, t)$ is the stress field. The aim is to understand wave motion in terms of velocity, so the stress component needs to be characterized. Hooke's law (Hooke, 1678) which relates stress and strain, thoroughly explains the stress space in the medium.

$$\sigma_{ij} = \sum_k^{n=3} \sum_l^{n=3} C_{ijkl} \epsilon_{kl} \quad i, j = 1, 2, 3$$

Equation 1.2

Equation 1.2 describes Hooke's law where σ is stress, ϵ is strain. The elastic modulus tensor – stiffness tensor, C_{ijkl} relates strain to stress. This tensor fully characterizes the elasticity of the medium. C_{ijkl} has 81 coefficients as it is a 3x3x3x3 tensor. Taking the symmetry of stress ($\sigma_{ij} = \sigma_{ji}$) and strain ($\epsilon_{kl} = \epsilon_{lk}$) into consideration, the coefficients are reduced to 21 (Thomsen 1986). For simplicity, if Voigt notation is used:

$$ij \rightarrow \alpha; kl \rightarrow \beta$$

So,

$$11 \rightarrow 1; 22 \rightarrow 2; 33 \rightarrow 3; 32 = 23 \rightarrow 4; 31 = 13 \rightarrow 5; 12 = 21 \rightarrow 6$$

Equation 1.3

C_{ijkl} becomes $C_{\alpha\beta}$

$$\begin{bmatrix} C_{11} & C_{12} & C_{13} & & & & \\ C_{12} & C_{22} & C_{23} & & & & \\ C_{13} & C_{23} & C_{33} & & & & \\ & & & C_{44} & & & \\ & & & & C_{55} & & \\ & & & & & C_{66} & \end{bmatrix}$$

to be aligned in the same direction. As the compaction acts normal to the bedding, the platelets are aligned parallel, satisfying a VTI medium assumption.

The stiffness matrix in VTI media has five independent components.

$$\begin{bmatrix} C_{11} & C_{11} - 2C_{66} & C_{13} & & & & \\ C_{11} - 2C_{66} & C_{11} & C_{13} & & & & \\ C_{13} & C_{13} & C_{33} & & & & \\ & & & C_{44} & & & \\ & & & & C_{44} & & \\ & & & & & C_{44} & \\ & & & & & & C_{66} \end{bmatrix}$$

Equation 1.8

The solutions resulting from wave equation (Equation 1.6) using this stiffness matrix will explain the propagation of different wave modes. There are three solutions – one with quasi – normal (P), one with transverse (SH), and one with quasi – transverse (SV) (Thomsen 1986, Daley & Hron 1977). Considering VTI medium, the solutions are:

$$\begin{aligned} \rho v_P^2 &= \frac{1}{2} [C_{33} + C_{44} + (C_{11} - C_{33}) \sin^2 \theta + D(\theta)] \\ \rho v_{SV}^2 &= \frac{1}{2} [C_{33} + C_{44} + (C_{11} - C_{33}) \sin^2 \theta - D(\theta)] \\ \rho v_{SH}^2 &= C_{66} \sin^2 \theta + C_{44} \cos^2 \theta \end{aligned}$$

Equation 1.9

ρ – density, θ – phase angle between wavefront normal and the vertical axis.

$$\begin{aligned} D(\theta) &= ((C_{33} - C_{44})^2 + 2(2(C_{13} + C_{44})^2 - (C_{33} - C_{44})(C_{11} + C_{33} - 2 * C_{44})) \sin^2 \theta \\ &\quad + ((C_{11} + C_{33} - 2C_{44})^2 - 4(C_{13} + C_{44})^2) \sin^4 \theta)^{\frac{1}{2}} \end{aligned}$$

Equation 1.10

The algebraic difficulty of the D-factor is the main barrier when implementing anisotropic models (Thomsen 1986). To make the implementation a bit easier, Thomsen 1986 suggested modifying Equations 1.9 and making them dependent on only two elastic moduli of main wave types (P- and S-wave velocities) and 3 “anisotropic parameters”. P- and S-wave velocities should be chosen as the ones that are in the same direction as the symmetry plane. Because of the VTI medium's vertical symmetry plane, the velocities should be selected as vertical. He suggested the following combinations, which later on are called anisotropic or Thomsen parameters:

$$\begin{aligned} \varepsilon &= \frac{C_{11} - C_{33}}{2C_{33}} \\ \gamma &= \frac{C_{66} - C_{44}}{2C_{44}} \end{aligned}$$

$$\delta = \frac{(C_{13} + C_{44})^2 - (C_{33} - C_{44})}{2C_{33} (C_{33} - C_{44})}$$

Equation 1.11

This combination turns out very useful in terms of defining elastic anisotropy (Thomsen, 2002). These three parameters have properties of simplifying the wave equations, being nondimensional, and becoming zero in the degenerate case where the VTI medium is reduced to an isotropic medium (Thomsen 1986, Thomsen 2014). In the formations where these combinations are less than 1, it is possible to assume these formations have weak elastic anisotropy. One can use these anisotropy parameters to assess whether any TI anisotropy case is weak or not. So, they have become the conventional anisotropy measures used to characterize anisotropic formations in most geophysical contexts (Thomsen 2014).

Besides simplifying the wave equations and defining elastic anisotropy, these three parameters eliminate the inconvenience of using stiffness coefficients for the applications such as seismic processing or inversion (Tvaskin et al. 2010). They provide useful information about transverse anisotropy (with chosen symmetry plane), which guides inversion and processing algorithms (Tvaskin et al. 2010). Tvaskin et al. 2010 also argue that these parameters are particularly convenient for reflection data processing as they simplify the essential expressions such as NMO velocity, quartic moveout coefficient, AVO response, and geometrical spreading.

1.2. Weak Anisotropy

By substituting Thomsen parameters directly to Equations 1.9, we will have full equations considering all degrees of anisotropy (Equations 1.12).

$$\begin{aligned} v_P^2(\theta) &= V_{P0}^2 * [1 + \varepsilon \sin^2 \theta + D'] \\ v_{SV}^2(\theta) &= V_{S0}^2 * \left[1 + \varepsilon \frac{V_{P0}}{V_{S0}} \sin^2 \theta - \frac{V_{P0}}{V_{S0}} D' \right] \\ v_{SH}^2(\theta) &= V_{S0}^2 (1 + 2\gamma \sin^2 \theta) \end{aligned}$$

with

$$D' = \frac{1 - \left(\frac{V_{P0}}{V_{S0}}\right)^2}{2} \left[\left(1 + \frac{4(2\delta - \varepsilon)}{1 - \left(\frac{V_{P0}}{V_{S0}}\right)^2} \sin^2 \theta \cos^2 \theta + \frac{4\varepsilon \left(1 - \left(\frac{V_{P0}}{V_{S0}}\right)^2 + \varepsilon\right)}{\left(1 - \left(\frac{V_{P0}}{V_{S0}}\right)^2\right)^2} \sin^4 \theta \right)^{-1} - 1 \right]$$

Equation 1.12

Regardless of the algebraic complexity of equations, progress can be made. However, by testing and observing, most geophysical formations have a range of anisotropic parameters that do not exceed 0.3 – 0.4, implying a weak anisotropy ($\varepsilon, \gamma, \delta \ll 1$). For example, even though the

minerals in the rock are highly anisotropic by nature, the rock itself can exhibit weak anisotropy. That's why until a half century ago (until the anisotropy was discovered), the anisotropy was ignored because the analysis based on isotropy had yielded good results in production and exploration (Thomsen 2014). So, when considering weak anisotropy and substituting the above equations to Equations 1.9, it will yield:

$$\begin{aligned}v_p(\theta) &= V_{P0}(1 + \delta \sin^2 \theta \cos^2 \theta + \varepsilon \sin^4 \theta) \\v_{SV}(\theta) &= V_{S0} \left[1 + \frac{V_{P0}}{V_{S0}} (\varepsilon - \delta) \sin^2 \theta \cos^2 \theta \right] \\v_{SH}(\theta) &= V_{S0}(1 + \gamma \sin^2 \theta)\end{aligned}$$

Equation 1.13

where $V_{P0} = \sqrt{\frac{C_{33}}{\rho}}$ - vertical P-wave velocity, $V_{S0} = \sqrt{\frac{C_{44}}{\rho}}$ - vertical S-wave velocity.

By investigating these equations further, we can draw interesting conclusions which can be useful in practice. First let's take $\theta = 0^\circ$, vertical incidence case. $\sin 0^\circ = 0$, so, these means, the outputs are the equations of vertical velocities (V_{P0} and V_{S0}). The same can be drawn from horizontal incidence ($\theta = 90^\circ$). $\sin 90^\circ = 1, \cos 90^\circ = 0$, so, now we have the equations for horizontal velocities (Figure 1).

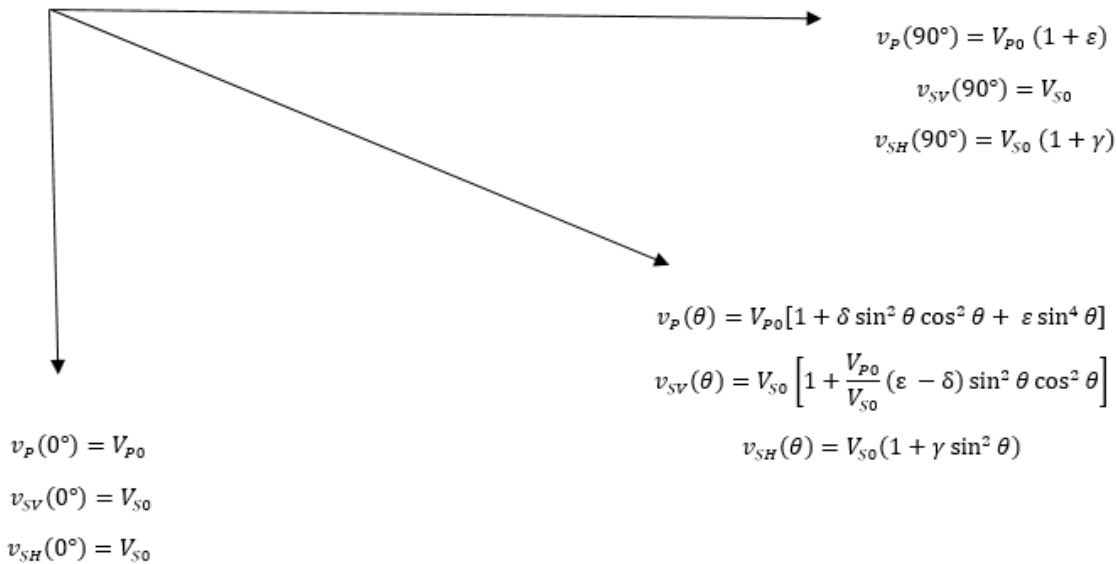


Figure 1. Wave velocity equations

From horizontal velocity equations, we can easily extract the definitions of ε , and γ .

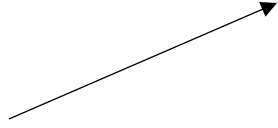
$$\varepsilon = \frac{v_P(90^\circ) - V_{P0}}{V_{P0}} \text{ and } \gamma = \frac{v_S(90^\circ) - V_{S0}}{V_{S0}}$$

Equation 1.14

Thus, ε is the difference between horizontal and vertical P-wave velocity, and γ is the same for S – wave. For detailed information, we can start looking at Equation 1.12. The wave velocity expression for SH-wave is precisely the equation of elliptical wavefront. The corresponding expression in Equation 1.13 is just a linearized version (Thomsen 2014). From this, the conclusion is γ is the ellipticity of SH wavefront and the vertical S-velocity (V_{S0}) is just the short axis of the ellipse. Yet, we cannot draw a similar conclusion for ε . From the expression of v_P , we can see that P-wavefront is not an ellipse, because the equation depends on three terms – V_{P0} , δ , ε (in the case of weak anisotropy – Equations 1.13), however, elliptical expressions only need two dependent terms. Actually, it is possible to approximate P-wavefront to an ellipse if we ignore the non-elliptic part of the equation. Yet, this can lead us to serious problems conceptually and operationally (Thomsen 2014). The question here is how can we assess this non-ellipticity? To view this non-ellipticity, we can rewrite v_P expression:

$$v_P(\theta) = V_{P0}[1 + \delta \sin^2 \theta \cos^2 \theta + \varepsilon \sin^4 \theta] = V_{P0}[1 + \delta \sin^2 \theta + (\varepsilon - \delta) \sin^4 \theta]$$

Equation 1.15

$$\eta' = \varepsilon - \delta$$


The new expression reveals that the non-ellipticity part is controlled by the difference between ε and γ which is denoted here as η' . This parameter characterizes weak anellipticity. Note that in the case of small angles, this term can be neglected (Thomsen 2014). Additionally, this expression is only true when weak anisotropy is assumed. In the case of strong anisotropy, the anellipticity parameter is in Equation 1.16.

$$\eta = \frac{\varepsilon - \delta}{1 + \delta}$$

Equation 1.16

But what happens if we approximate P-wavefront to an ellipse? At the horizontal direction, V_{P0} would be the short axis of the ellipse and $V_P(90^\circ)$ would be the long axis of the ellipse. Then, ε would be its ellipticity (Equation 1.17). However, we rarely have near-horizontal rays in exploration geophysics, most of the time, we use near-vertical rays (Thomsen 2014).

$$V_P^2(90^\circ) = V_{P0}^2 (1 + 2\varepsilon)$$

Equation 1.17

Then, let's try to fit at vertical direction. At the vertical direction, we still have V_{P0} as the short axis of the ellipse, but now, δ would be its ellipticity (Equation 1.18).

$$V_P^2(\theta) = V_{P0}^2(1 + \delta \sin^2 \theta)$$

Equation 1.18

The true P-wavefront will be in between these ellipses at mid-angles (Figure 2) (Thomsen 2014).

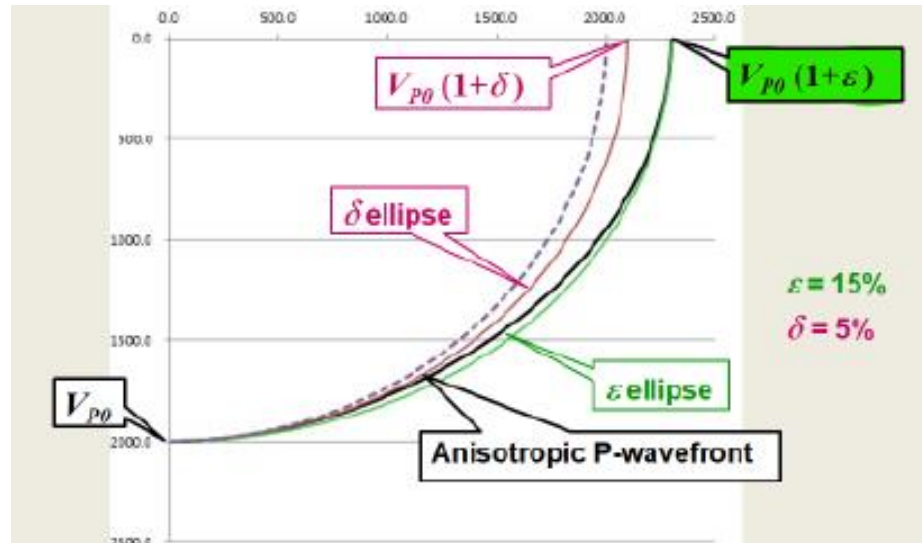


Figure 2. P-wavefront comparison (Thomsen 2014)

We can elaborate more on the physical meanings of these parameters analytically. According to Thomsen 1986's reliable data, the majority of the samples have a positive ϵ , and γ , this means the both horizontal velocities are greater than the vertical velocities, in other words, the stiffnesses that control the horizontal propagation is greater than those that controls the vertical propagation ($C_{11} > C_{33}$ and $C_{66} > C_{44}$) (Thomsen 1986, Postma 1955). Yet, this has no applicability in nearly vertical P – wave propagation which is the most encountered case in exploration geophysics (Thomsen 1986). The reason is that if we consider nearly vertical propagation ($\theta \approx 0$), based on Equations 1.13, $\sin^2 \theta \cos^2 \theta$ will not be as small as $\sin^4 \theta$ (Thomsen 1986). On the other hand, if we consider horizontal P-wave propagation ($\theta \approx 90^\circ$), because of $\cos \frac{\pi}{2} = 0$, δ term will be removed. These two cases coincide with what we discussed in P-wavefront comparison. Therefore, combining these two analyses, we can confidently say that in nearly vertical P – wave propagation, δ controls the elastic anisotropy, while in nearly horizontal P – wave propagation, ϵ is a controlling factor in anisotropy (Thomsen 1986). When it comes to γ , as mentioned above it controls the anisotropy of SH-wave.

1.3. Physical causes

In order to fully understand the elastic anisotropy, the causes should also be investigated. In theory, there are three main causes of anisotropy: Intrinsic, Stress – induced, and layer – induced anisotropy.

1.4.1. Intrinsic Anisotropy

The common constituents of shales are clay minerals (e.g., biotite, smectite, kaolinite, illite, muscovite) that have sheet-like/platelet-like structures. Several studies done on these clay platelets (Alexandrov & Ryzhova 1961; Belikov et al., 1970, Katahara, 1996) have shown that the ratio of horizontal and vertical P-wave velocities of platelets often results in 1.5, the ratio for S-waves can reach 3.5 (Grechka 2009). This natural velocity anisotropy is thought to be related to the sedimentation process. As the clays are deposited, they are arranged into their most stable and suitable position because of the depositional energy, which results in preferential alignment. This means that the anisotropy during deposition develops when the grains have a degree of directionality, either in composition, size, shape, orientation, or packing (Melaku 2007). Therefore, shale and its clay platelets are anisotropic in nature without any external forces.

Hornby et al. 1994's study confirmed the preferential alignment theory by investigating SEM (Scanning Electron Microscope) images (Li, 2006). The fine intrinsic layering is clearly seen from the SEM image of clay mineral, which displays an intrinsic anisotropy in Figure 3. These proved that one of the fundamental causes of elastic anisotropy is the preferential alignment during deposition, which forms intrinsic anisotropy (Wang 2002).

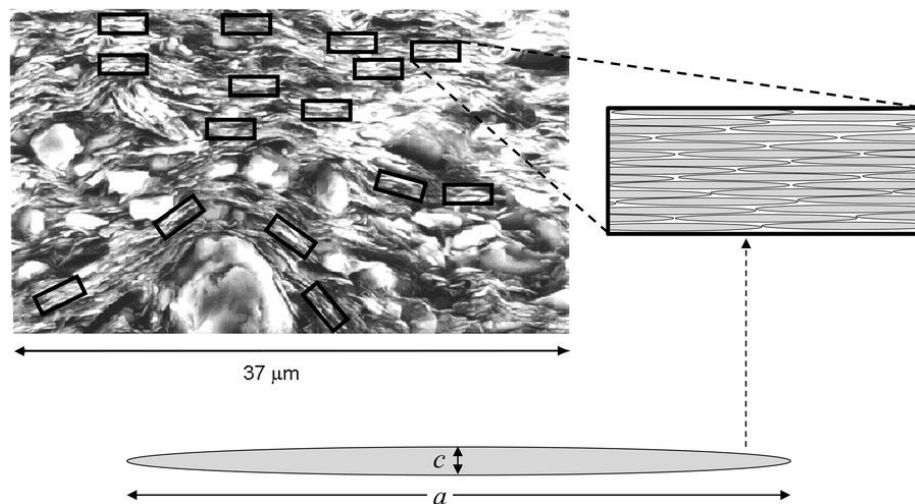


Figure 3. SEM image of clay - Intrinsic anisotropy (Sayers & den Boer 2019, Hornby et al. 1994)

1.4.2. Stress-induced anisotropy

Another important type of anisotropy is stress-induced anisotropy. Here the most influencing factor is the porosity of the rock. The porosity evolution in shales can be a clear indicator of stress-

induced anisotropy. Due to the high porosity, young shales have less lamination, indicating a minor degree of intrinsic anisotropy (Wang 2002). When mechanical and diagenetic compaction occurs, this high porosity starts to decrease, and platelets start to be more compacted (Raven et al. 2011, Wang 2002). This results in a new type of anisotropy – stress-induced anisotropy developing. Depending on the stress applied, the anisotropy can be increased or decreased. Therefore, stress-induced anisotropy is created by applied stress and causes orientational changes in rock fabric. Thus, the preferred orientation of minerals or cracks (parallel or vertical) results from stress-induced anisotropy (Raven et al. 2011, Thomsen 1986). Additionally, after the section is cored, the rocks under in-situ overburden stress are exposed to stress release, generating microcracks in the rock, which also adds external anisotropy. In order to understand stress-induced anisotropy, it is necessary to pre-stress the rock into in-situ stress and saturation conditions (Wang 2002).

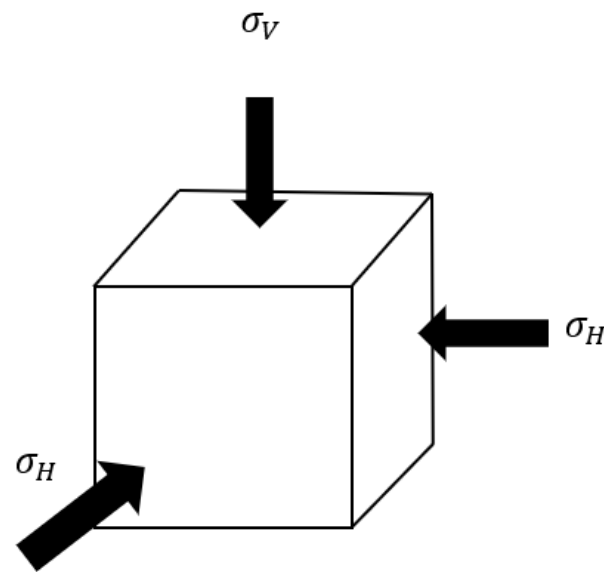


Figure 4. Stress test. σ_V – vertical stress, σ_H – horizontal stress

We can observe the stress-induced anisotropy by a simple laboratory test. Figure 4 illustrates a cube that can be assumed as a core sample and is exposed to vertical and horizontal stresses. In theory, if we increase the net stress (Equation 1.19), the microcracks that existed in the rock tend to close, and the rock grains will be in better contact. This is directly related to vertical velocity. As we increase net stress, the vertical stress also increases and closes the microcracks. This will increase the vertical velocity, and the difference between horizontal and vertical velocity (intrinsic anisotropy) becomes smaller. Thus, the overall anisotropy is expected to decrease as net stress increases. Yet, in another case, if the horizontal stress is increased, the overall elastic anisotropy will be diminished.

$$\sigma' = \frac{\sigma_V - 2\sigma_H}{3}$$

Equation 1. 19

In order to comprehend the importance of stress-induced anisotropy, we can look at a simple case, a rock with a random distribution of cracks embedded in an isotropic medium. The rock is isotropic in the initial state when no stress is applied. If hydrostatic stress (average stress of all directions) is introduced, all cracks in different directions will respond similarly, and the rock becomes stiffer but still remains as isotropic. Nevertheless, if uniaxial stress is introduced, the cracks parallel to the stress axis will tend to close, and the rock will take on transversely isotropic symmetry (Mavko et al. 2009). That's why Mavko et al. 2009 argues that a wave is most sensitive to cracks when its direction of propagation is perpendicular to the crack faces.

Nur & Simmons 1969, Lockner et al. 1997, Zamora & Poirier 1990, Sayers et al. 1990, Yin 1992, Cruts et al. 1995 have discussed the demonstration of this anisotropy through laboratory tests (Mavko et al. 2009). The laboratory tests done by Wang 2002 and Raven et al. 2011 have resulted in clear patterns to prove the theory. Wang 2002 reports that in hard shale samples, it is possible to see a decrease in ϵ , yet, this effect is also observed in γ , but with smaller percentages. In soft shales, both reductions are significant as net stress increases (Wang 2002). Additionally, Raven et al. 2011 performed a sequence of laboratory tests to observe the clear patterns in brine-saturated shale samples. The test consists of 6 cycles in which net stress is increased during and between cycles. The whole stress range used was 10 – 73 MPa. The result of Raven et al. 2011's laboratory test on vertical shale plugs with net stress normal to the bedding is in Figure 5. In each cycle, as the net stress increases, the vertical velocities (black ones in Figure 5) start to increase monotonically while ϵ decreases (Raven et al. 2011). At high-stress ranges, the increase is little, but the overall increase in vertical velocities is evident. Anisotropic parameter ϵ decreases as net stress increases with the starting point, indicating intrinsic ϵ from clay platelets. Note that these findings are consistent with what's discussed above. A similar test was conducted for horizontal plugs. The results are more complicated, but the overall stress patterns are evident. In conclusion, with horizontal plugs where net stress is parallel to the bedding, grain contacts and dilatancy are destroyed, which leads to an increase in elastic anisotropy (Raven et al., 2011). While, with vertical plugs where net stress is normal to the bedding, pre-existing fractures and fissures tend to close, leading to a decline in anisotropy (Raven et al. 2011).

Sayers 1999 has successfully extracted a stress contribution of anisotropy in terms of compliance tensor, which is an inverse version of stiffness tensor. He assumed that the deformation of contact regions between clay platelets causes the stress dependence of elastic properties of shale. These contacts are assumed to close at high-stress regimes, and the shale can be treated as a homogenous anisotropic medium. At the intermediate regimes, the contact regions between clay platelets will be partly open (Sayers 1999).

$$S_{ijkl} = S_{ijkl}^0 + \Delta S_{ijkl}$$

Equation 1. 20

Here, S_{ijkl} is total compliance, S_{ijkl}^0 – compliance at high stress regimes (when all contacts are closed – intrinsic), ΔS_{ijkl} – excess compliance by stress contribution. A full overview of estimating the excess compliance is in Appendix A.

A study done by Sayers 1999 once proved that the definition of stress-induced anisotropy is not easy to acquire or handle. Based on Sayers 1999's method, a series of laboratory tests are required in order to obtain a reliable set of the necessary parameters.

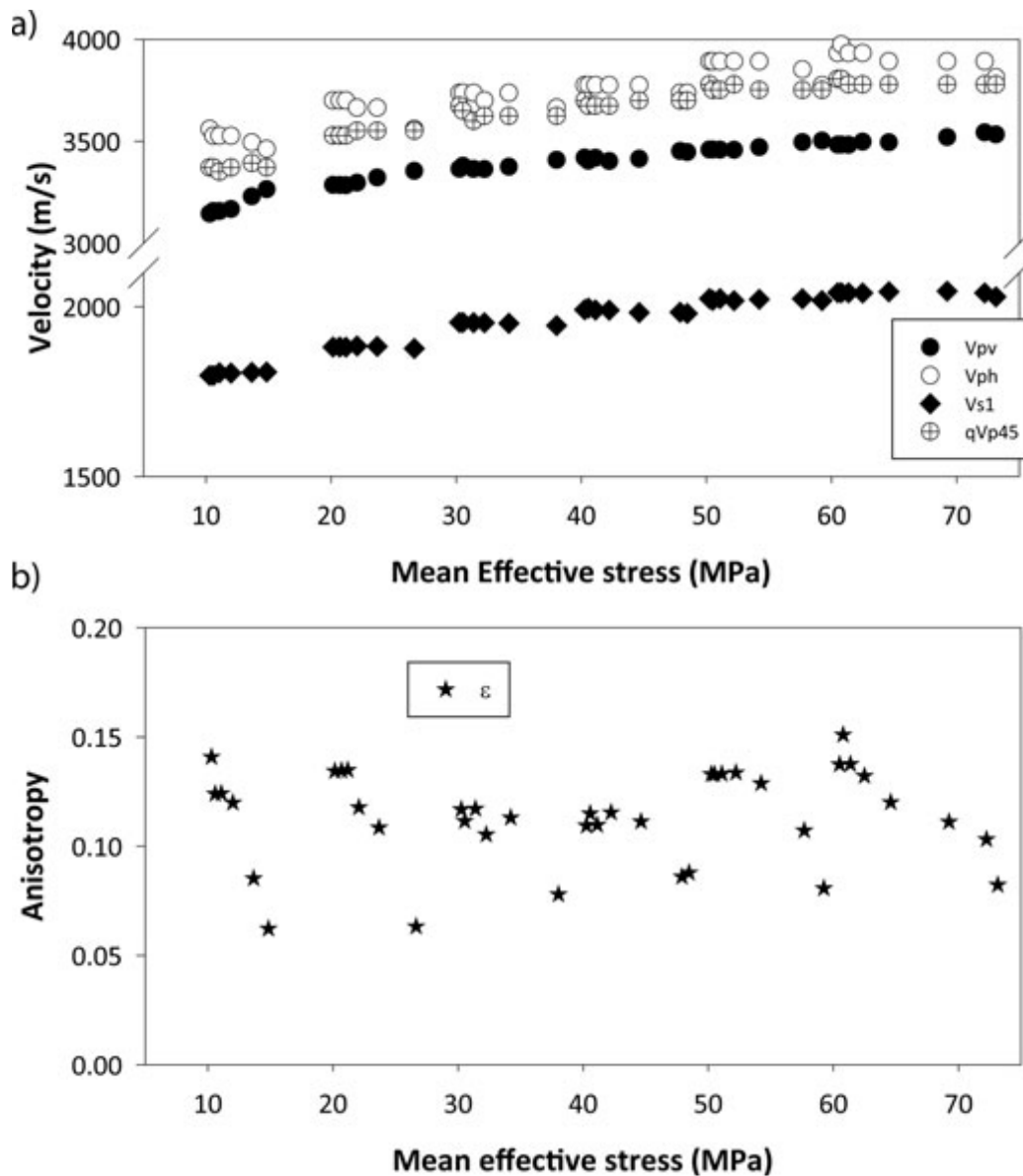


Figure 5. Velocities (a) and ϵ (b) as a function of mean effective stress for shale sample, where the core plug is cut normal to bedding (Raven et al. 2011).

1.4.3. Layer-induced anisotropy

The third cause of anisotropy is the fine layering of the rock layers, yet, here, the scale is much larger than preferential alignment, which causes intrinsic anisotropy. This type of anisotropy is the primary cause of the difference between sonic and seismic experiment results. When a subsurface section is logged, if the thickness of a layer is smaller than the wavelength used in the logging, the device will not “see” this layer. The tool will take several layers and treat them as one stack layer. The anisotropy caused by this layering is called layer – induced anisotropy. Layer-induced anisotropy is actually a first cause of anisotropy that had been examined and proved the effective anisotropy theory (Riznichenko, 1949).

In nature, such fine layering can be associated with alternating layers of sand-shale or layers of hard and soft sands (Wang 2002). An important constraint in layer-induced anisotropy is that the thickness of an individual fine layer must be much smaller than the seismic wavelength used. Therefore, the whole sequence of layers is considered one homogenous but anisotropic layer (Figure 6).

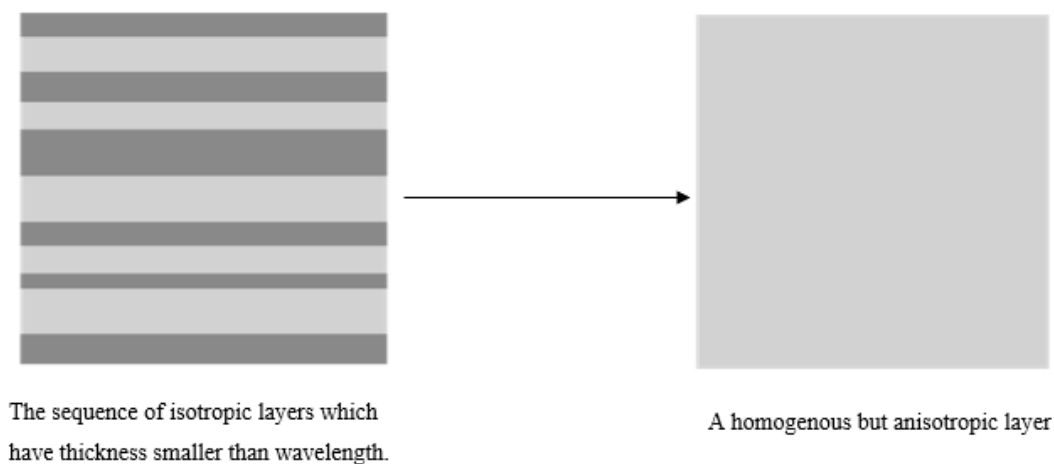


Figure 6. Layer – Induced Anisotropy (Hall 2016).

The fundamentals of layer-induced anisotropy are summarized in Backus 1962’s paper. Backus 1962 proved that in the long-wavelength limit, any stratified medium composed of fine isotropic layers is an effective anisotropic medium with a symmetry axis normal to the layers (Figure 7) (Grechka 2009).

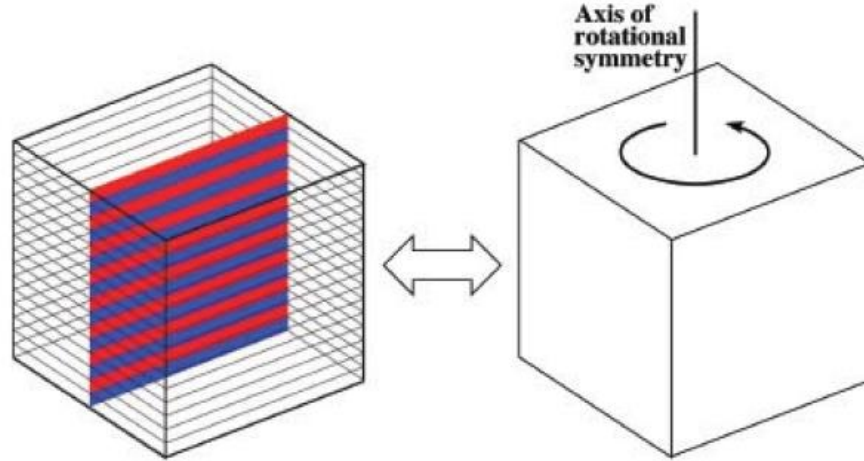


Figure 7. Layer-Induced anisotropy: a medium composed of finely layered isotropic layers (left) is equivalent to homogenous anisotropic medium with the symmetry axis normal to the layers (Grechka 2009).

The effective stiffnesses are averaged along predefined window by their volumetric proportions (Mavko et al. 2009, Backus 1962). If we follow the stiffness matrix in Equation 1.8 which represents elastic stiffnesses of a fine layer, the effective stiffnesses will be as follows:

$$\begin{bmatrix} C_{11B} & C_{11B} - 2C_{66B} & C_{13B} & & & & \\ C_{11B} - 2C_{66B} & C_{11B} & C_{13B} & & & & \\ C_{13B} & C_{13B} & C_{33B} & & & & \\ & & & C_{44B} & & & \\ & & & & C_{44B} & & \\ & & & & & C_{44B} & \\ & & & & & & C_{66B} \end{bmatrix}$$

where,

$$\begin{aligned} C_{11B} &= \langle C_{11} - C_{13}^2 C_{33}^{-1} \rangle + \langle C_{13} C_{33}^{-1} \rangle^2 \langle C_{33}^{-1} \rangle^{-1} \\ C_{13B} &= \langle C_{33}^{-1} \rangle^{-1} \langle C_{13} C_{33}^{-1} \rangle \\ C_{33B} &= \langle C_{33}^{-1} \rangle^{-1} \\ C_{44B} &= \langle C_{44}^{-1} \rangle^{-1} \\ C_{66B} &= \langle C_{66} \rangle \end{aligned}$$

Equations 1. 21

$\langle \cdot \rangle$ indicates averages by volumetric proportions. This average is called Backus average.

If an individual fine layer is isotropic, the number of independent stiffnesses are reduced to 2. Note that the resulting effective medium is still TI medium.

$$C_{11} = C_{33} = \lambda + 2\mu, \quad C_{13} = \lambda, \quad C_{44} = C_{66} = \mu$$

$$\begin{aligned}
C_{11B} &= \left\langle \frac{4\mu(\lambda + 2\mu)}{\lambda + 2\mu} \right\rangle + \left\langle \frac{\lambda}{\lambda + 2\mu} \right\rangle^2 \left\langle \frac{1}{\lambda + 2\mu} \right\rangle^{-1} \\
C_{13B} &= \left\langle \frac{1}{\lambda + 2\mu} \right\rangle^{-1} \left\langle \frac{\lambda}{\lambda + 2\mu} \right\rangle \\
C_{33B} &= \left\langle \frac{1}{\lambda + 2\mu} \right\rangle^{-1} \\
C_{44B} &= \left\langle \frac{1}{\mu} \right\rangle^{-1} \\
C_{66B} &= \langle \mu \rangle
\end{aligned}$$

Equation 1. 22

Additional to layer thickness constraint, in order to use the Backus theory, two more assumptions should be fulfilled. The layers should be linearly elastic and there should not be any source of intrinsic energy dissipation, namely, friction or viscosity.

Furthermore, in order to perform Backus averaging, a representative averaging window should be set. The averaging window defines how many small layers should be included to average. Backus 1962 suggests that to average over a small individual layer to obtain a homogenous but anisotropy layer, the averaging window should also be smaller than the dominant wavelength considered (Equation 1.23).

$$\text{Averaging window } (d) \leq \frac{\lambda_{Dom}}{N} = \frac{V_{min}}{Nf_{Dom}}$$

Equation 1. 23

where, λ_{Dom} – dominant wavelength, f_{Dom} – dominant frequency. V_{min} – minimum velocity.

There have been many discussions about which order this window should be smaller than the dominant wavelength to get reasonable outputs. As a rule of thumb, it was accepted $N = 10$, but considering a layer thickness ten times smaller than the dominant wavelength became inconvenient in implementation. Liner & Fei 2006's study came up with a solution to achieve precise results. The study suggests and successfully proves that it is enough to consider N equal to 3. In other words, the window should be less than or equal to one-third of the dominant wavelength.

Therefore, as seen above, none of these causes are not easy to determine. Although, the laboratory results show that the major anisotropic plays in the rock are intrinsic and layer – induced causes ([Wang 2002](#)), designing an anisotropy prediction model that assumes all three causes is something that scientists are still working on. The model suggested in the later chapters is formulated to solve this problem and provide the anisotropic information in full scope.

Chapter 2. Model

Although Thomsen's definition of elastic anisotropy gives a proper explanation, the practical means of acquiring these parameters has been debated for years in the geophysics community. Because acquiring a horizontal well reading is not usual in conventional logging, Thomsen's anisotropy parameters (ϵ , γ and δ) should have been defined by other sources (δ additionally require measurements at 45°). Several authors have introduced various anisotropy models using nearly vertical wells to better predict the elastic anisotropy. Naghiyev 2021 has summarized several prominent anisotropy models – Sayers & den Boer 2020, Yan et al. 2016, Li 2006, Ryan-Grigor 1997, Horne 2013, Pervukhina & Rasolofosaon 2017, and aimed to define the most cost-effective and user-friendly model by comparing estimated results and well log readings. The best model should link conventional well logging to generate anisotropic information logs, as well as horizontal velocity logs. According to the analysis done in Naghiyev 2021, Li 2006's ϵ , and γ models have performed best compared to real well log data. Although the results of Naghiyev 2021 show that the previously introduced anisotropic models have performed reasonably well, the common problem with all suggested models is the assumptions considered. In studied models, the cause of anisotropy is explained by the intrinsic nature of the rock. Although layer-induced effects can be added to the models in implementation, the studies ignore the stress contribution of elastic anisotropy. Besides that, some models derived from regression studies (Sayers & den Boer 2020) or specific datasets (Horne 2013) add additional uncertainties to the prediction. Therefore, the ultimate model also needs to be in the frame of scientific definitions. Although works such as Li 2006, Sayers 1994 did successfully define intrinsic anisotropy by theoretical means (Li 2006 have described it using clay content and Sayers 1994 used the orientation of clay platelets), the addition of stress-induced anisotropy has always been a difficult part. Sayers 1999 has attempted stress-induced anisotropy in terms of elastic compliances (Appendix A). Although the theory has successfully addressed the stress contribution, the implementation is not straightforward.

That's why there is a need for a model based on theoretical background and takes stress contribution into account along with the intrinsic nature of the rock. Then, the layer-induced effects can be added by selecting an appropriate averaging window.

In this chapter, I will present a model that theoretically (practically in late chapters) achieves and fulfills this aim. We are taking a different approach and claiming that it is possible to define an anisotropic prediction model by presenting a full understanding of wave propagation. Our ultimate goal is to deduce horizontal stiffnesses (or velocities) and Thomsen parameters which are not feasible to acquire by conventional logging tools. The basic idea is to extract the horizontal information using vertical information. This means we assume a direct link exists between the rock's vertical and horizontal properties. Thus, if we can successfully identify and understand the factors affecting the vertical propagation of the waves, it would be possible to describe the horizontal propagation by projecting vertical propagation. This link was also the core assumption in anisotropic prediction models such as Li 2006, Sayers & den Boer 2020, Horne 2013, and so on. Additionally, since the vertical data is generally available in most wells, they would be

appropriate inputs to our prediction model. In summary, our model is going to deduce stiffnesses in the horizontal direction (C_{11} for ε , and C_{66} for γ) using the vertical propagation data. Ultimately, we expand the model's utilities and suggest predicting anisotropy in a non-zero propagation angle.

Before going into the detail of propagation, we need a functional way to project vertical data into horizontal data. Assuming the bounds such as Reuss-Voigt (Voigt 1889, Reuss 1929) can help perform this transition along with including the influencing factors. Since, in the physical media, the rocks cannot be as stiff as Voigt's upper bound, by taking Reuss's lower bound as a baseline of the prediction models, the model becomes as close as possible to reality (Mavko et al. 2009). Additionally, the primary assumption behind the Reuss bound is fulfilled in vertical propagation. Thus, one of the main assumptions in our prediction model is that all constituents of the rock are experiencing the same directional stress in the same plane. The expression of Reuss bound is in Equation 2.1, where M_H , and M_V are the moduli in horizontal and vertical directions, respectively.

$$M_H = \left(\frac{f}{M_V} \right)^{-1}$$

Equation 2. 1

2.1. Vertical P-wave propagation and influencing factors

We start with a vertical P-wave propagation. As discussed, the influencing factors of P-wave vertical propagation will define the P-wave horizontal component of stiffness - C_{11} . The vertical P-wave propagation in clayey media is sketched in Figure 8. The blue arrow indicates the direction of propagation while the black arrow is the vertical cartesian coordinate Z . Red arrows represent all three stresses. As the propagation is in the vertical plane, the wave propagates through the oriented clay platelets, represented by the black bars.

By definition, the deposition or orientation of these clayey platelets is the direct cause of intrinsic anisotropy. Thus, this means, from the deposition, we already have a difference in velocities ($V_{PH} > V_{PV}$) (See Figure 8). This has been broadly discussed by Sayers & den Boer 2020 and Hornby 1994. So, intrinsic anisotropy can be addressed by taking the clay content (V_{cl}) into consideration. According to the Reuss average, it is a must to divide the vertical response to the appropriate clay fractions. Yet, the analyses have shown that different clay types influence anisotropy differently. For example, despite authigenic clays having a strong anisotropic response, the effect of anisotropy in detrital clays is not noteworthy (Wang, 2002). Additionally, the orientation of these clay particles also has a great influence on the outcome. Since intrinsic anisotropy is not solely dependent on clay content, using clay content alone as a decisive factor will introduce several uncertainties and shortcomings to the prediction model. It might be a good idea to look for answers by taking the whole rock into account. From petrophysical point, the rock consists of the pore volume (ϕ_T), non-clayey matrix volume ($V_{non-clay}$), and clay volume (V_{cl}) (Equation 2.2). This model suggests that all the factors affecting the clays including orientation and type, are summarized under V_{cl} . Thus, by considering "1 - V_{cl} " - anisotropy-free volume (stress-induced anisotropy still applicable), we are accessing the intrinsic nature of the anisotropy

without worrying about the factors contributing to the intrinsic anisotropy. Thereby, if more clay is added to the available pore volume, a new intrinsic anisotropy is going to be built by a decrease in porosity. Because the porosity is going down in the right part of Equation 2.3, the left part, which represents the anisotropy-free volume, also starts to be diminished. Additionally, in construction of new prediction model, we have to take the anisotropic response of rocks into account. As discussed, the effect of elastic anisotropy is more spoken when the medium is becoming clayey. Hence, in the case of sandstone, the prediction should lead to negative anisotropy, which means the estimated horizontal stiffness coefficient should be lower than the vertical stiffness coefficient. Since we are diving the vertical propagation measurements into the intrinsic anisotropy indicator, including " $1 - V_{cl}$ " will help to consider these effects. Consequently, in order to lower the theoretical uncertainties and boost the model's performance, the intrinsic anisotropy is addressed using the non-clay volume ($V_{non-clay} + \phi_{total}$).

$$V_{cl} + V_{non-clay} + \phi_{total} = 1$$

Equation 2. 2

$$1 - V_{cl} = V_{non-clay} + \phi_{total}$$

Equation 2. 3

Now, we can continue with the second and mostly ignored cause of anisotropy – stress-induced anisotropy. As we suggest, it can also be understood by closely examining the propagation of the wave.

If P-wave is propagating vertically through clay platelets and two effective stresses felt by granular media in the horizontal plane are considered equal ($\sigma'_H = \sigma'_h$), the wave is mainly affected by vertical stress since the direction of propagation (also parallel to the polarization direction) of the P-wave is parallel to the stress direction (Figure 8). However, since the horizontal P-wave propagates and polarizes in the same direction on the horizontal plane, our resulting model should depend on horizontal stress rather than vertical stress. If the in-situ stress in vertical P-wave measurement is vertical stress, then a way to correct the stress effect is required. In principle, in order to compensate the vertical stress effect, the measurement can be multiplied by a scalar which is the effective stress ratio ($K_0 = \frac{\sigma'_h}{\sigma'_V}$). Therefore, by multiplication, the vertical measurement will be corrected. Because the vertical stress component will vanish, the modeled quantity is going to be affected by horizontal stress ($C_{11} = C_{33} \frac{\sigma'_h}{\sigma'_V}$, C_{11} will only be affected by horizontal stress). As a result, we successfully address the stress-induced anisotropy in the prediction model without dealing with complicated equations.

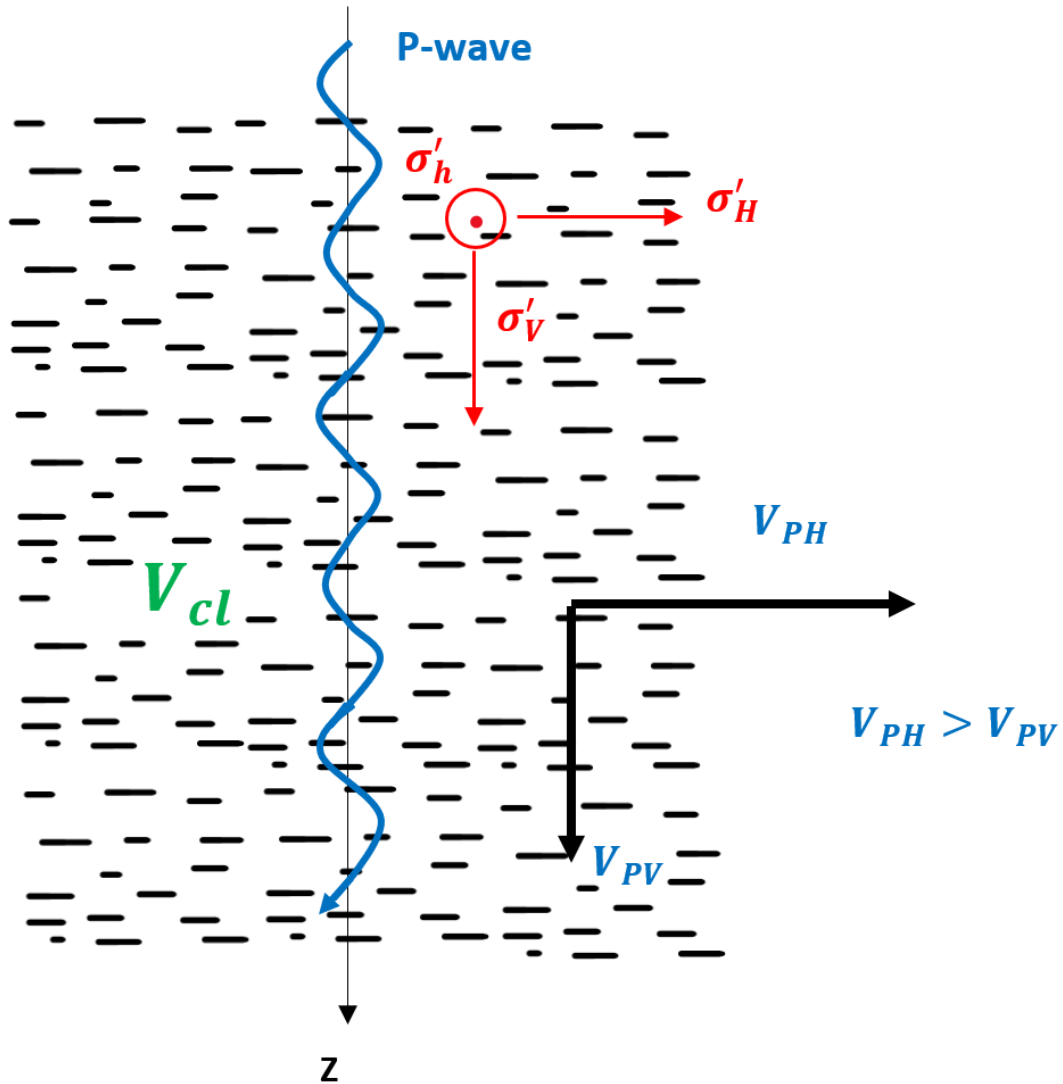


Figure 8. P-wave propagation in clayey medium.

The final prediction model considering intrinsic and stress contributions is presented in Equation 2.4.

$$C_{11} = \left(\frac{1 - V_{cl}}{C_{33}K_0} \right)^{-1}$$

Equation 2. 4

Then, the P-wave anisotropy – ε is acquired using Thomsen 1986's ε definition, (Equation 2.5).

$$\hat{\varepsilon} = \frac{C_{11}^{estimated} - C_{33}^{measured}}{2C_{33}^{measured}}$$

Equation 2. 5

In the end, it is worth noting that the proposed model also fulfills Hooke's law criteria (Hooke 1678). As Hooke's law states, the stiffness of a media is the parameter that links stresses to strains. Thus, if the model is conceptually correct, Hooke's law should yield the horizontal stiffness coefficient. The verification steps are shown in Equation 2.6. Using the definition of K_0 , which is the horizontal-to-vertical stress ratio, it is possible to access the vertical strain of the media (ϵ_{33}). Since the remaining stress is the horizontal stress, using classical Hooke's law, one can show that the result will be a horizontal stiffness coefficient.

$$C_{11} = \left(\frac{1 - V_{cl}}{C_{33}K_0} \right)^{-1} = \left(\frac{1 - V_{cl}}{\sigma'_h} \frac{\sigma'_V}{C_{33}} \right)^{-1} = \left((1 - V_{cl}) \frac{\epsilon_{33}}{\sigma'_h} \right)^{-1}$$

Equation 2. 6

2.2. Vertical S-wave propagation and influencing factors

A similar analysis can be performed for vertical S-wave propagation to understand the horizontal stiffness component (C_{66}). The vertical S-wave propagation in clayey media is sketched in Figure 9. The blue arrow indicates the direction of propagation while the black arrow is again the vertical cartesian coordinate Z . The clay platelets are shown by black bars and all three stresses by red arrows. The only difference between the illustrations of P- and SV- wave propagations is that SV-wave propagates in the vertical plane while polarizing in the horizontal plane. As the subsurface model is the same as P-wave propagation, the equivalent principle for the same reasons will be used for dealing with intrinsic anisotropy. Thus, we are again dividing the vertical SV-wave response to " $1 - V_{cl}$ ". Yet, the main distinction in P- and SV-wave propagation is the stress contribution. As SV-wave propagates in the vertical direction while polarizing in the horizontal direction, the stress primarily affecting the propagation will not be vertical or horizontal. The in-situ stress in SV-wave propagation will be mean stress. The equation of mean stress is in Equation 2.7, considering the two stresses in the horizontal plane are equal ($\sigma'_H = \sigma'_h$). Although another widely used version of mean stress is the one that is defined by only two directions $\left(\frac{\sigma'_V + \sigma'_h}{2} \right)$ yet, by introducing the third horizontal direction on the horizontal plane, the resulting stress will be corrected for the third dimension, which will improve the model's predictability.

$$\sigma_m = \frac{\sigma'_V + 2\sigma'_h}{3}$$

Equation 2. 7

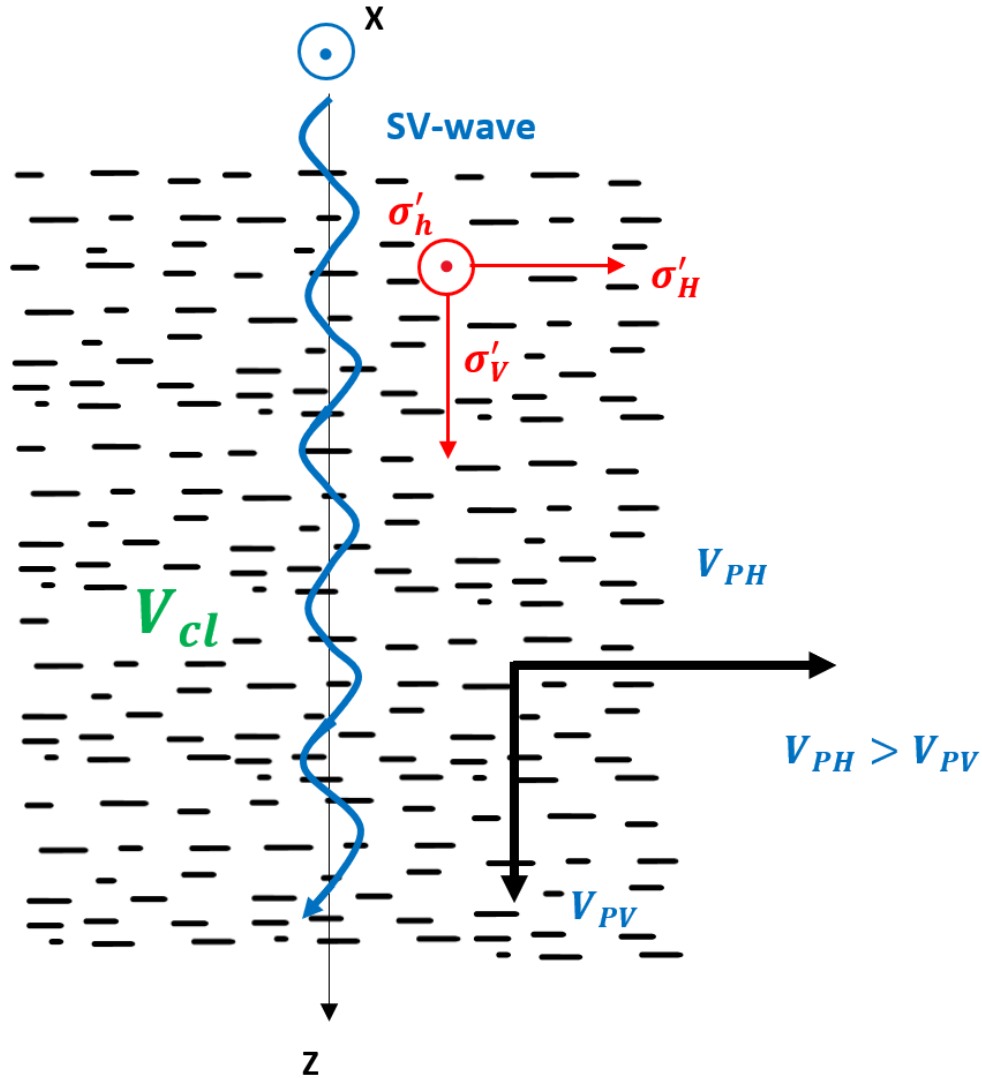


Figure 9. SV-wave propagation in clayey medium.

Since the horizontal S-wave (SH) propagates and polarizes in the horizontal plane, the measurement should be compensated for mean stress. Here, the propagation and polarization are not in the same direction but same plane. Since the stresses in the horizontal plane are equal, the difference in direction does not affect the result. Because P-wave is influenced by vertical stress, the multiplication of $\frac{\sigma'_h}{\sigma'_v}$ succeeds its objective. Yet in SV-wave propagation, the major stress affecting is mean stress, that's why the compensation should be done by $\frac{\sigma'_h}{\sigma'_m}$. Since it is not straightforward to handle mean stress, the stress ratio needs to be modified. The steps of modification are in Equation 2.8. This modification helps us simplify and generalize the expression, now like in P-wave propagation, in order to address stress contribution in SV-wave propagation, only input required is the horizontal-to-vertical stress ratio coefficient (K_0).

$$\frac{\sigma'_h}{\sigma'_M} = \frac{\sigma'_h}{\frac{\sigma'_V + 2\sigma'_h}{3}} = \frac{\frac{3\sigma'_h}{\sigma'_V}}{\frac{\sigma'_V + 2\sigma'_h}{\sigma'_V}} = \frac{\frac{3\sigma'_h}{\sigma'_V}}{1 + 2\frac{\sigma'_h}{\sigma'_V}} = \frac{3K_0}{1 + 2K_0}$$

Equation 2. 8

The basic version of prediction model for C_{66} combining intrinsic and stress effects is in Equation 2.9.

$$C_{66} = \left(\frac{1 - V_{cl}}{C_{44} \left(\frac{3K_0}{1 + 2K_0} \right)} \right)^{-1}$$

Equation 2. 9

It is still possible to show that Equation in 2.9 obeys the Hooke's law (Equation 2.10). Since the stress correction factor is $\frac{\sigma'_h}{\sigma'_m}$, the application will still yield in the vertical strain. Using vertical strain and the remaining stress, the horizontal stiffness coefficient can be found.

$$C_{66} = \left(\frac{1 - V_{cl}}{C_{44} \left(\frac{3K_0}{1 + 2K_0} \right)} \right)^{-1} = \left(\frac{1 - V_{cl}}{C_{44} \frac{\sigma'_h}{\sigma'_m}} \right)^{-1} \left(\frac{1 - V_{cl} \frac{\sigma'_m}{\sigma'_h}}{C_{44}} \right)^{-1} = \left((1 - V_{cl}) \frac{\epsilon_{44}}{\sigma'_h} \right)^{-1}$$

Equation 2. 10

Like ϵ , S-wave anisotropy – γ is extracted using Thomsen 1986's γ definition (Equation 2.11).

$$\hat{\gamma} = \frac{C_{66}^{estimated} - C_{44}^{measured}}{2C_{44}^{measured}}$$

Equation 2. 11

2.3. Last Thomsen parameter

Our proposed model explains P- and S-wave anisotropies (ϵ and γ) considering all the contributing factors in the real subsurface medium. Yet, we have not made any discussion on the third Thomsen parameter, δ . As discussed in the theory chapter, δ is a crucial parameter in the cases of vertical P-wave propagation. However, this parameter is only accessible when we have P-wave propagation at 45° . Even in laboratory conditions, conducting a 45° propagation test on cores is very difficult and a primary source of the most uncertainties (Wang 2002). Several studies have discussed that the relation between ϵ and δ is linear (Li 2006, Asaka 2018), and the implementation of these relationships is quite successful (Naghiyev 2021). The conclusion of Naghiyev 2021 shows that when compared with the well reading, a study done by Li 2006

considers a linear relationship between ε and δ works quite satisfactory. Li 2006 has examined the data from Thomsen 1986, Vernik & Nur 1992, Johnson & Christensen 1995, and Vernik & Liu 1997's rock information data, resulting in the approximation in Equation 2.12. The basic theory of Li 2006's anisotropy approach is in Appendix B.

$$\delta = 0.32\varepsilon$$

Equation 2. 12

Although this relationship is a product of general estimation, the performance is still acceptable. Later, Asaka 2018 proposed another linear approximation by estimating epsilon during parameter scan for flattening the gathers and delta by comparing check-shot and seismic velocities. His estimation is in Equation 2.13.

$$\delta = 0.76923\varepsilon$$

Equation 2. 13

Since these approximations practically result in satisfactory values, Thomsen's 1986's data have been analyzed to achieve a similar approximation. The data reflects elastic anisotropy as well as velocity and pressure measurements and combines the original data from laboratory-derived ultrasonic velocity measurements and seismic-band velocity readings from the field. That's why because of the reliability of the data, the analysis using this data would potentially produce a good approximation. A new approximation by linear regression using Thomsen 1986's data is presented in Equation 2.14 and illustrated in Figure 10.

$$\delta = 0.352467\varepsilon$$

Equation 2. 14

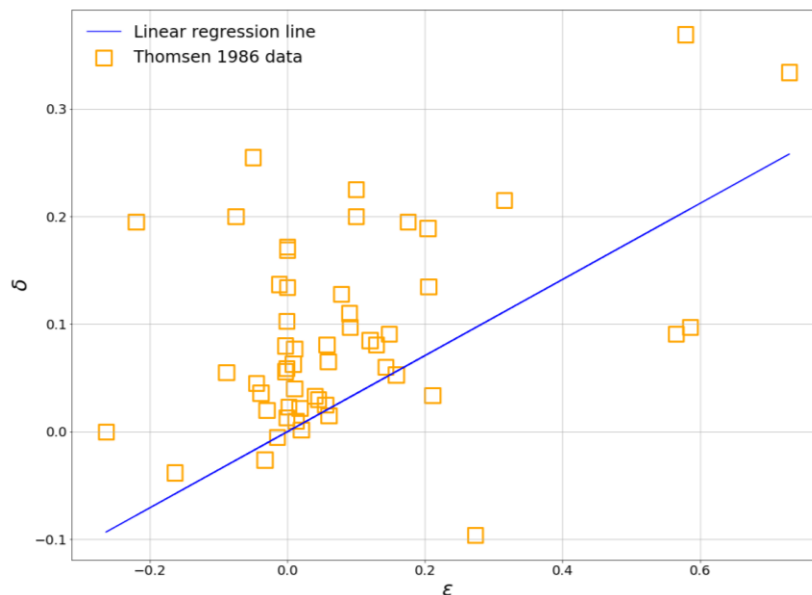


Figure 10. Estimation of V_{SV} (left). Red: Well measurement, Blue: Estimated V_S . Estimation of ρ (left). Red: Well measurement, Blue: Estimated ρ . Grey area is hydrocarbon filled reservoir

These approximations and their validations show that the linear approximation between ε and δ could be used. Since the results from analyzing Thomsen 1986's data confirms the linear dependency, it is possible to use the linearity to address δ . Thus, the linear approximation resulted from regression using Thomsen 1986's data will be used to generate δ log in further steps.

By considering a linear approximation for δ , the prediction modelling set for elastic anisotropy is complete. Now, it is necessary to remind and have a full understanding on the model's assumption. The main assumptions are:

- Elastic anisotropy subjected to the rock is weak, and the parametrization is based on Thomsen 1986 theory.
- The rock medium is assumed as a Vertically Transverse Isotropic (VTI) medium
- The rock bodies are linear, elastic and homogenous.
- There is a direct link between vertical and horizontal measurements ($C_V \propto C_H$). So, by correcting one measurement, it is possible to obtain the other.
- Hooke's law is valid.
- The model is treated as Reuss model.
- Model is valid in water-wet formations.
- Hydrostatic equilibrium has been met.
- A linear dependency between δ and ε is considered.

In order to successfully estimate all three Thomsen parameters using the proposed anisotropy prediction model, all the assumptions have to be fulfilled.

2.4. Predicting elastic anisotropy in non-zero angles

Our prediction model has been devised to predict the propagation in horizontal direction (90°). However, most of the cases, we are also interested in velocities anisotropies at non-horizontal propagation. Using the prediction results (three anisotropic parameters) and vertical sonic measurements, it is possible to estimate velocities at arbitrary angles by Equation 2.15 (same with Equation 1.13) when weak elastic anisotropy is assumed.

$$\begin{aligned}
 v_p(\theta) &= V_{P0}(1 + \delta \sin^2 \theta \cos^2 \theta + \varepsilon \sin^4 \theta) \\
 v_{SV}(\theta) &= V_{S0} \left[1 + \frac{V_{P0}}{V_{S0}} (\varepsilon - \delta) \sin^2 \theta \cos^2 \theta \right] \\
 v_{SH}(\theta) &= V_{S0}(1 + \gamma \sin^2 \theta)
 \end{aligned}$$

Equation 2. 15

Chapter 3. Supporting parametrization

Now, our analysis has formulated two prediction models: one for C_{11} leading to ε and one for C_{66} leading to γ . The principal motivation in generating these models is to define a convenient-to-use, theory-based model where the results can be acquired by inputting conventional well logging. Thus, in this chapter, I will present a full description of how to handle the constitutive parameters. The definition suggests predicting the elastic anisotropy using three main sets of measurements: vertical stiffnesses (C_{33} and C_{44}) describing vertical propagation, horizontal-to-vertical stress ratio (K_0) representing stress contribution of anisotropy and clay content (V_{cl}) defining intrinsic contribution of anisotropy. Even though defining some of these parameters can seem fairly straightforward to obtain, close attention to their origin is necessary.

3.1. Vertical stiffness coefficients

It is always nice to start with more obvious parameters like stiffness coefficients. The classical definition (see Chapter 1.1) states that the vertical stiffness coefficients are the product of density and vertical velocity measurements ($C_{33} = \rho V_{PV}^2$, $C_{44} = \rho V_{SV}^2$). If density and vertical sonic logs are present, then the vertical stiffnesses can easily be acquired from these measurements. The main question is whether they are always available or not. With the recent advances, the laboratories and log readings often yield these measurements (Mavko et al. 2009). Yet, there are many cases (new or old data) in which only P-wave sonic measurements are available. Since they are crucial parameters to define elastic anisotropy, their absence would mean not continuing prediction. So, other empirical methods for acquiring them also have to be reviewed. Although in literature numerous models estimate well readings, the choice has to be made on its functionality and ease of implementation.

For S-wave measurement, Greenberg & Castagna 1992's relations seem to be a great choice. They have developed empirical relationships in homogenous, brine-saturated pure monomineralic rocks. It proposes that the vertical shear wave velocities (V_{SV}) can be acquired using vertical compression wave velocities (V_{PV}) by the respected lithologies. The generalized expression is in Equation 3.1.

$$V_S = a_{i2}V_P^2 + a_{i1}V_P + a_{i0}$$

Equation 3. 1

Table 1. Coefficients of Greenberg-Castagna shear wave estimation relationships for pure lithologies

Lithology	a_{i2}	a_{i1}	a_{i0}
Sandstone	0	0.80416	-0.85588
Limestone	-0.05508	1.01677	-1.03049
Dolomite	0	0.58321	-0.07775
Shale	0	0.76969	-0.86735

Representative coefficients for the most encountered sedimentary rocks are in Table 1 (Greenberg-Castagna 1992, Castagna 1993, Mavko et al. 2009). Note that the expressions are for 100% water-saturated rocks. For using them in other fluid phases or saturations, the Gassmann 1951's equations should be used (Mavko et al. 2009). The verification of the Greenberg-Castagna model is done using well 7220/8-1. The model is applied to the vertical P-wave velocities, and the resulting SV-wave velocities are compared with the actual SV-wave measurements from the well 7220/8-1. The results are in Figure 11 (left). As seen from Figure 11 (left), the Greenberg-Castagna relation results in fairly good SV-wave measurements when compared with the real measurements from the well. Since the Greenberg-Castagna relation is valid on the water-filled rocks, it results in mismatches in the presence of oil & gas (grey section on the plot). This comparison ensures us about the predictability of Greenberg-Castagna empirical relationships. Therefore, in the absence of SV-wave measurements, Greenberg-Castagna is a fairly good choice of model for the estimation.

Another measurement to be focused on is density measurement. Although it is rare not to acquire density measurement in the conventional well logging suites, a handful of empirical relationships can always help. For the purpose of obtaining density measurements, Gardner et al. 1974 has developed a set of empirical, lithology-specific relationships (Gardner et al. 1974, Castagna 1993, Mavko et al. 2009). These relationships use P-wave velocities (V_{PV}) to estimate densities (ρ). The generalized expression is in Equation 3.2. The representative polynomial regression coefficients are in Table 2 (Mavko et al. 2009).

$$\rho = aV_p^b$$

Equation 3. 2

Table 2. Coefficients of Gardner's density estimation relationships for pure lithologies

Lithology	a_{i2}	a_{i1}
Sandstone	0	0.80416
Limestone	-0.05508	1.01677
Dolomite	0	0.58321
Shale	0	0.76969

The verification of Gardner's model is done using well 7220/8-1. The model is applied to the vertical P-wave velocities, and the resulting densities are compared with the true density measurements from the well, presented in Figure 11 (right). Although mismatches are present, the overall performance of the model is good. Thus, this relationship can be used for estimating density measurements.

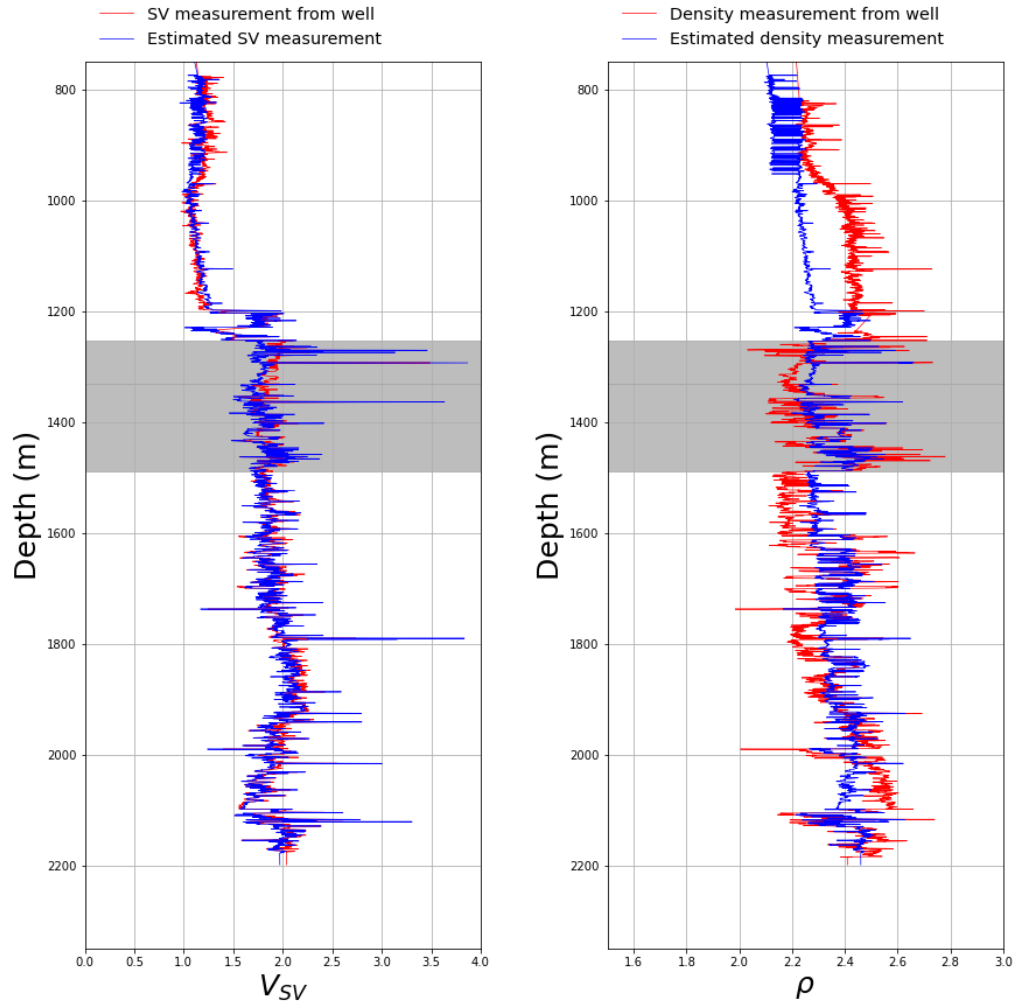


Figure 11. Estimation of V_{SV} (left). Red: Well measurement, Blue: Estimated V_S . Estimation of ρ (left). Red: Well measurement, Blue: Estimated ρ . Grey area is hydrocarbon filled reservoir

Now, we have set the basic empirical relations for interpolating the missing log values. In order to implement them correctly, the lithological descriptions of the applied subsurface section should be known. Since the basics of our study are about elastic anisotropy, an important distinction should be made between clayey rocks (e.g., shale) and non-clayey rocks (e.g., sandstone). This distinction can be performed by addressing the shale content of the rock. Figure 12 illustrates the constituents of a sand-shale mixture rock. The model obeys the volumetric rock unity equation (Equation 2.2). Figure 12 shows that the clayey part of the rock is summarized under V_{sh} . Before, we have discussed and included V_{cl} into the prediction model, yet the clayey section of the rock also consists of bounded water within the clay platelets (clay bound water - CBW) and the different minerals in the form of silt ($V_{sh} = V_{cl} + V_{silt} + CBW$). Thus, in order to perform the estimation based on the relationships mentioned above that depend on the lithological type, V_{sh} is the fair indicator to be chosen as a cut-off value. The most straightforward and most used approach to acquire V_{sh} is using gamma ray reading which is always available in well log

suits. Gamma ray shaliness index formula for estimating V_{sh} is in Equation 3.3. Although numerous other methods exist, such as Clavier et al. 1971, Larionov 1969, and Stieber 1973, the shaliness equation is widely used because of its simplicity. The choice of cut-off value varies a lot, yet, because of elastic anisotropy, which is mainly addressed in shaley structures, the typical cut-off value can be chosen as 0.25 or 0.4. Thus, below the cut-off value, the estimation is done based on non-clay rocks (mostly sandstone), and above the cut-off value, the rock is considered clayey rock.

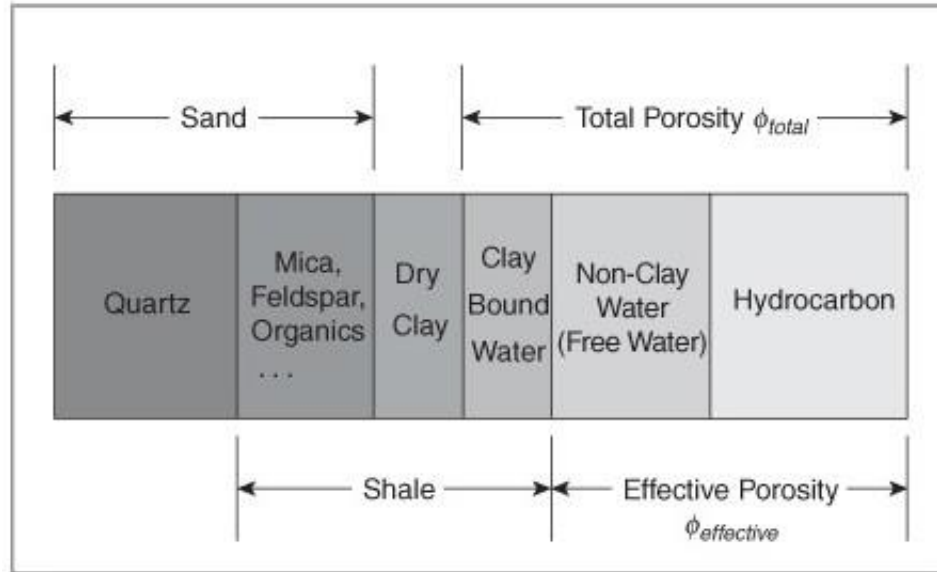


Figure 12. Volumetric rock volume (Ezekwe 2010).

$$V_{sh} = \frac{GR_{log} - GR_{MIN}}{GR_{MAX} - GR_{MIN}}$$

Equation 3. 3

3.2. Horizontal-to-vertical stress ratio: K_0

Horizontal-to-vertical stress ratio, K_0 is a powerful notation in order to consider the stress contribution in the proposed model. Since the term is directly related to the stresses, laboratory measurements are the best tools to acquire its true values. However, acquiring a stress log is even harder than basic anisotropic parameter logs, so, this ratio needs to be closely examined and extracted by other means. For the model's simplicity in implementation, a way to extract the stress relationships using well log reading is necessary.

When the stress is applied to a material, there is a deformation response measured by strain. Robert Hooke's work in continuous media in 1678 clearly states these stress-strain relationships. Owing to Hooke's law, the stress ratio can may be understood by taking strain ratio into account $\left(\frac{\sigma_h}{\sigma_v} \sim \frac{\epsilon_h}{\epsilon_v}\right)$. A good starting point is Gretener 1994's definition of strain ratio using Poisson's ratio (Poisson 1829). Poisson 1829 has defined a variable (Poisson's ratio) which measures the

deformation of a material when a stress is applied perpendicular to that deformation. In that regard, the Poisson's ratio (ν) equals to the negative ratio of horizontal-to-vertical strains (Equation 3.4) (Gretener 1994, Thomsen 1996). If the material is linearly elastic and isotropic, the Poisson's ratio can be expressed by incompressibility (bulk modulus) K and rigidity (shear modulus) G^{**} (Equation 3.5).

$$\nu = -\frac{\epsilon_h}{\epsilon_v}$$

Equation 3. 4

$$\nu = -\frac{\epsilon_h}{\epsilon_v} = \frac{3K - 2G}{6K + 2G}$$

Equation 3. 5

Afterwards, Gretener 2003 discussed that the effective stress ratio is dependent on Poisson's ratio in the uniaxial strain regime using Hooke's law (Equation 3.6). This means if there is a way to measure Poisson's ratio by well log measurements, then, the horizontal-to-vertical stress ratio K_0 can directly be calculated in the same. If we substitute moduli in Equation 3.5 with velocities using Equation 3.7, Poisson's ratio can be estimated by sonic measurements (Equation 3.8).

$$K_0 = \frac{\sigma_h}{\sigma_v} = \frac{1 - \nu}{\nu}$$

Equation 3. 6

$$V_P = \sqrt{\frac{K + \frac{4}{3}G}{\rho}}; V_S = \sqrt{\frac{G}{\rho}}$$

Equation 3. 7

(See Equation 1.7)

$$\nu = \frac{\left(\frac{V_P}{V_S}\right)^2 - 2}{2\left(\frac{V_P}{V_S}\right)^2 - 2}$$

Equation 3. 8

Thus, in the case of homogenous, isotropic, linearly elastic rock with uniaxial deformation, the stress ratio is defined by Equation 3.9.

** The rigidity of a material is the same moduli as shear modulus.

$$K_0 = \frac{\sigma_H}{\sigma_V} = 1 - 2 \left(\frac{V_S}{V_P} \right)^2$$

Equation 3. 9

Although V_P/V_S ratio successfully estimates K_0 , because of its isotropic assumptions, it is not suitable for our purpose. That's why there is still an anisotropic correction to perform. Thomsen 1990 and Thomsen 1996 studies have argued the inequality of this equation in the cases of elastic anisotropy. These discussions led us to include elastic anisotropy using Thomsen's anisotropic parameter, δ . So, in the case of anisotropy, K_0 will be improved by δ (Equation 3.10). Now, the only question which δ can be used here? The practical applications showed that the influence of δ used here on model's precision is small. That's why using a constant δ could be beneficial. So, in order to address a very weak and moderately strong anisotropy in the clayey rock case, $\delta = 0.05$ and $\delta = 0.15$ are used respectively.

$$K_0 = \frac{\sigma_H}{\sigma_V} = 1 - 2 \left(\frac{V_S}{V_P} \right)^2 + \delta$$

Equation 3. 10

3.3. Clay content V_{cl}

Another parameter that has to be defined precisely is the clay content of the rock. As it discussed, V_{cl} is a decisive factor in intrinsic anisotropy and stress sensitivity. In the implementation, we will see in further chapters that this petrophysical parameter controls general anisotropy trends and has an essential influence on the reliability of the proposed model. In petrophysical applications, there are several ways to estimate actual clay content.

It is possible to acquire V_{cl} as a part of the elemental spectroscopy well log suite. Because these spectroscopy readings give as true V_{cl} as possible, the method is considered the best option to obtain V_{cl} information. Another reliable way of using well logging is the spectral gamma ray logs. Since the clay portion of the rock is highly radioactive by potassium, thorium, and uranium, using spectral gamma ray readings of these elements will determine a quite reliable V_{cl} information. An example expression using thorium log is in Equation 3.11. These logs perform better than natural gamma ray logs because they pinpoint the exact elements that the clay platelets are composed of. On the contrary, the natural gamma readings are best for calculating V_{sh} using the IGR method discussed in Equation 3.3. Since elemental spectroscopy and spectral gamma ray logs can be absent in some well log suites, an empirical approach would be required to handle.

$$V_{cl} = \frac{TH_{log} - TH_{MIN}}{TH_{MAX} - TH_{MIN}}$$

Equation 3. 11

The easiest way to estimate V_{cl} is using shale content. As discussed before, the shale content does not only represent the clay content since it also contains other minerals and bound water.

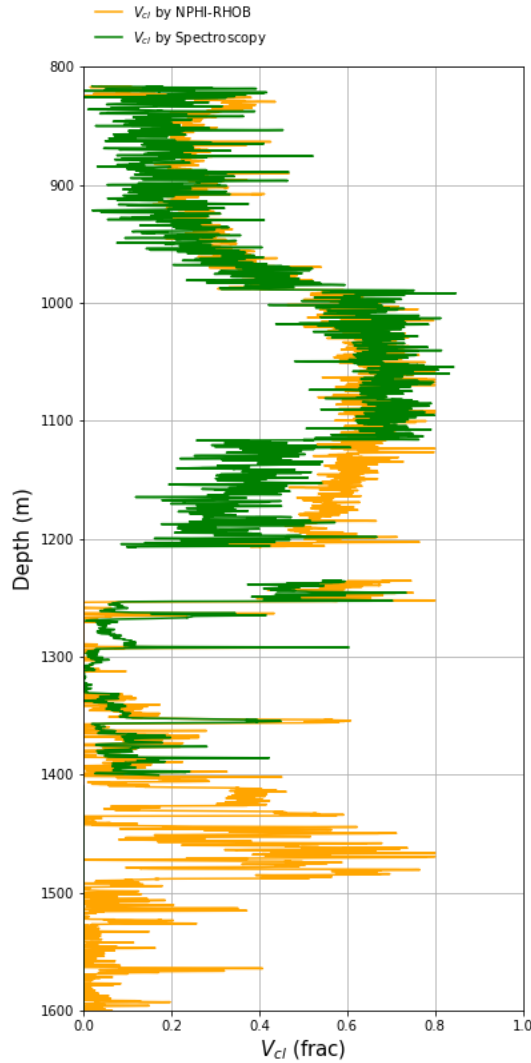


Figure 13. Comparison of clay content calculation from Spectroscopy log and Neutron-Density porosity method proposed by La Vigne 1994 using well 7220/8-1

However, from petrophysical practice, it is possible to say that in most cases, the clay content contains 60 % of the shale volume. Therefore, as a rough assumption, an empirical relation such as $V_{cl} = 0.6 V_{sh}$ is suitable in practice.

Another method that is currently popular to estimate V_{cl} is using neutron-density porosity. In petrophysics, the density porosity using conventional formation density logs is considered one of the most reliable sources of computing effective porosity (Equation 3.12). La Vigne et al. 1994 have proved that it is possible to obtain V_{cl} by combining density porosity with one of the most common log readings – neutron porosity (Equation 3.13). In order to verify this empirical method, a comparison has been made using well 7220/8-1 data. The comparison of La Vigne et al. 1994 method's results and clay content readings from the elemental spectroscopy log is in Figure 13. From Figure 13, it is obvious that although a clear mismatch is observed at some intervals, overall performance of the method is pretty good. Additional to our comparison, Paiva et al. 2019 have compared several clay content estimation methods and discussed that because the well logs such as neutron and formation density, provide a good overview of the reservoir and non-reservoir rocks, the implementation of the Neutron-Density porosity method would likely have more reliable results. Yet, the method requires a fine selection of neutron

porosity reading at the clayey rock. This can be calculated by averaging the neutron values within a formation where V_{sh} estimations from natural gamma rays are high.

$$\phi_D = \frac{\rho_{mat} - \rho_{log}}{\rho_{mat} - \rho_{fluid}}$$

Equation 3. 12

$$V_{cl} = \frac{\phi_N - \phi_D + 0.025}{\phi_{N-clay}}$$

Equation 3. 13

3.4. Implementation of the model

It is essential to apply the model correctly in order to evaluate its performance. So, to better understand the model, a workflow with main bullet points is as follows:

1. Generate vertical stiffness coefficients (C_{33} and C_{44}) using formation density and vertical sonic measurement ($C_{33} = \rho V_{PV}^2$, $C_{44} = \rho V_{SV}^2$). If needed, use the empirical methods for obtaining those measurements.
2. Use elemental spectroscopy or spectral gamma rays to obtain V_{cl} . If not available, use second best option, La Vigne et al 1994's neutron and density porosity by Equation 3.13. Use appropriate matrix density for ρ_{mat} (most cases, sandstone's matrix density, 2.65 g/cc is suitable). Use appropriate fluid density for ρ_{fluid} (for formation water, 1.03 g/cc is suitable. For improving the choice, Batzle-Wang 1992 expressions can be used).
3. Use vertical sonic log measurements together with predefined δ to calculate horizontal-to-vertical stress ratio, K_0 .
4. Generate horizontal stiffness coefficients (C_{11} and C_{66}) by inputting vertical stiffness coefficients (C_{33} and C_{44}), estimated V_{cl} and estimated K_0 .
5. Produce ε and γ anisotropic logs by horizontal and vertical stiffness coefficients using Equation 2.5 and 2.11.
6. Complete elastic anisotropy prediction by calculating δ anisotropic log by modelled ε log using a linear approximation proposed by Li 2006.

As seen from the workflow, three main estimators are vertical stiffness measurements, stress contribution - K_0 and clay content. The computation of these parameters will affect the performance of the model. The implementation of this workflow to validate the model and assess its performance is in the next chapters.

Chapter 4. Validation & Performance

Now, all the aspects of the proposed model are defined theoretically. A need to validate this theory-based model's reliability and accuracy is a necessary step for evaluating its performance in practice and mitigating any imperfections. It will help us to be assured that this model gives a good representation of elastic anisotropy in the subsurface by comparing existing data.

4.1. Sonic Scanner

In previous chapters, we have seen that the model requires basic lithology-determining measurements as well as vertical sonic logs. However, along with those measurements, we also need an anisotropic information measurement based on the well readings to be used as a reference in verifying the model. A borehole acquisition tool called Sonic Scanner, devised by Schlumberger is the right source of the kind of information we need.

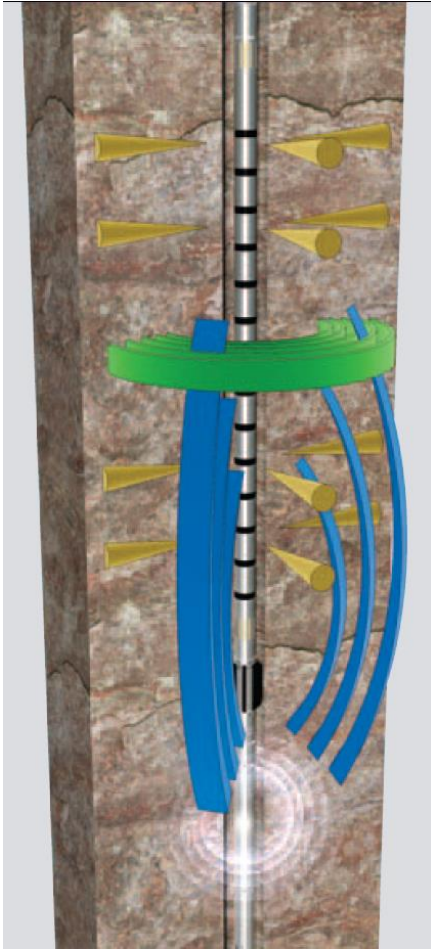


Figure 14. Sonic Scanner tool provides axial, azimuthal and radial information from both the monopole and the dipole measurements for near-wellbore and far-field slowness information (Schlumberger, 2005).

Although basic sonic tools have been utilized in the energy industry for decades for assessing formations in the near-wellbore area, they are limited in measuring the subsurface information (Schlumberger, 2005). Because the methods for exploiting reservoirs more efficiently are developed, which requires a good understanding of the subsurface medium, studies on well integrity have drawn attention. In 2005, Schlumberger designed a tool called Sonic Scanner, which uses the technology for advanced acoustic acquisition, such as cross-dipole and multi-spaced monopole measurements (Schlumberger, 2005). For a deeper understanding of acoustic behavior, the Sonic Scanner performs accurate radial and axial measurements of the rocks near the borehole. It presents data from multiple depths of investigations with superb waveform quality (Schlumberger, 2005). An overview of a Sonic Scanner tool is in Figure 14. Despite the rock type, the Sonic Scanner overcomes the obstacles from the previous acoustic measurements to successfully define formation characterization and quantification (Schlumberger, 2005). Since it uses a wide range of frequencies, it gives reliable information on the formation characterizations such as isotropic or anisotropic, homogenous or heterogeneous. It also uses long and short monopole transmitter-receiver spacing, making it more reliable as it captures data at a high signal-to-noise ratio (Schlumberger, 2005). Its applications include the improvement of the seismic-to-well tie, as well as 3D seismic analysis, identification of gas zones, measurement of fluid mobility, optimization of hydraulic fracturing, and so on (Schlumberger, 2005). It benefits by enhancing oil & gas recovery, improving reserves estimation, diminishing operation time & cost, eliminating the cost of running the logging multiple time, and overcoming uncertainties and operation risks (Schlumberger, 2005).

What interests us is it provides shear wave anisotropy. As discussed, it takes axial, azimuthal and radial slowness measurements which makes compressional, fast- and slow-shear, and Stoneley wave slowness available. It is possible to extract Thomsen parameter γ information using shear-wave splitting and Stoneley wave measurements. It is also worth noting that these measurements were affected by the presence of intrinsic anisotropy, formation stresses, and fluid mobility (Klimentos, 2007).

Thus, in order to perform performance validation to our proposed model, the data from Sonic Scanner will work as a real source to compare our findings.

4.1.1. Gamma measurement

As discussed, getting anisotropic measurements directly from the well is necessary to validate the model's reliability. Additionally, the ways of extracting the anisotropic information from wellbore data should also be clearly set. It is not always an easy task to extract anisotropic information from wellbore data. On the basis of Sonic Scanner, not all velocities from different angles (0° , 45° , 90° when considering VTI) are available, and this makes us to unable to compute ε or δ directly from Sonic Scanner data. Yet, since different S-wave velocities as well as Stoneley wave velocity measurement are available, borehole-derived anisotropic information by Thomsen anisotropic parameter γ can be acquired.

Although it is possible to derive γ from available horizontal and vertical S-wave velocities, the study done by Norris 1990 suggest that using Stoneley waves instead of horizontal S-waves will result in better measurements. The reason is that the method considers the effects of the logging tool itself. Since the method performs the logging tool correction, which is always recommended by petrophysicists, the resulting measurement will be more reliable than those yielded from shear wave splitting. The analytical expressions are in Equation 4.1.

$$V_{Stoneley} = \sqrt{\frac{C_{66}^*}{\rho_{BF}}}$$

$$\frac{1}{M_F} = (1 - f) \left(\frac{1}{C_{66}^*} - \frac{1}{K_{BF}} \right) - \frac{f}{M_T}$$

$$M_T = \mu_T \frac{1 - f_T}{f_T + \frac{1 - \nu_T}{1 + \nu_T}}$$

$$f = a^2/b^2$$

Equation 4. 1

where, $V_{Stoneley}$ – Stoneley wave velocity, ρ_{BF} –density of borehole fluid, C_{66}^* - effective stiffness from Stoneley wave, M_F – formation stiffness (moduli), M_T – tool stiffness (moduli), f – volume fraction of the tool occupies the borehole, K_{BF} – bulk modulus of borehole fluid, a – outer radii of the tool, b – radii of the borehole ($b > a$), f_T – volume fraction of inner part of the logging tool. The logging tool is considered as an annular elastic shell, and μ_T – shear modulus, ν_T – Poisson's ratio of this elastic shell.

We are after M_F because it characterizes the stiffness of the formation, so, can replace horizontal stiffness in classical definition (Equation 4.2)

$$\gamma = \frac{M_F - C_{44}^{well}}{2C_{44}^{well}}$$

Equation 4. 2

$M_T, \rho_B, K_{BF}, f, \mu_T$ and v_T are precisely defined during well logging, thus, these pieces of information are accessible in well log data schemes. If the logging tool used is a solid tool which is typically made of metal, $f_T = 0$. Once Stoneley wave measurement is available, we can derive a formation stiffness, then formation γ information.

4.2. Walk-Away Vertical Seismic Profiling

From Sonic Scanner, we successfully defined a reference γ measurement. However, in order to have a rough idea about the other two anisotropic parameters, we are still in need of relevant reference measurements. Here, the Walk Away Vertical Seismic Profiling survey comes into play. It is done by moving sources progressively farther offsets at the surface and holding a single tool that has multiple receivers at a fixed point (Schlumberger n.d). This provides a pseudo seismic line with higher resolution and more continuous coverage than surface seismic data (Schlumberger n.d). The general purpose of VSP is to acquire high-resolution images of velocity, attenuation, and anisotropy (Hardage 1983, Dillon & Thomson 1984, Campbel et al. 2005, Galybin & Dahlhaus 2019). The unique geometry of VSP data allows to perform a wide aperture seismic experiment to study angle-dependent velocities. It offers the methods to measure the vertical and horizontal components along with wave-type polarization. Using preconditioning and time picking of compressive wave travel time data, anisotropies are estimated by four methods (Schlumberger 2012). Because the estimation is done on P-wave time data, the extracted anisotropic parameters are ε and δ . These relatively satisfactory anisotropy results provide us with reference measurements for ε and δ .

A simplest method is the hyperbolic fit method for effective anisotropic determination which estimates anisotropy by fitting a parametrized moveout equation proposed by Alkhalifah and Tsvankin 1995 (Schlumberger 2012). The equation is in Equation 4.3. A non-linear optimization had been performed on the unknown parameters (t_0, V_{NMO}, η) . The optimization results in Thomsen parameters ε and δ using Equation 4.4.

$$t^2(x) \approx t_0^2 + \frac{x^2}{V_{NMO}^2} - \frac{2\eta x^4}{V_{NMO}^2(t_0^2 V_{NMO}^2 + (1 + 2\eta)x^2)}$$

Equation 4. 3

$$V_0^2 = \frac{z}{t_0^2} \quad V_{NMO}^2 = V_0^2(1 + 2\delta) \quad \varepsilon = \eta(1 + 2\delta) + \delta$$

Equation 4. 4

An isotropic model is generated using available well log data. Then, the model is improved to a VTI model by Backus averaging with an averaging window. Using this vertical velocity model, 1D VTI ray tracing was performed to determine the best fit (Schlumberger 2012). The anisotropy has been estimated by minimizing the difference in P-wave travel times. The third method is the Phase slowness method. This is an estimation method to obtain interval anisotropies using phase slowness values (Schlumberger 2012, Miller & Spencer 1993). The vertical and

horizontal slowness are extracted from travel time arrivals and then inverted to the interval anisotropy parameters (Schlumberger 2012). The fourth and last method is the slowness plus polarization method. The basis relies on local homogeneities around the receiver and does not depend on the structural complexities within the overburden. Using parametric wavefield decomposition proposed by Leaney 1990, P and SV polarizations and slowness are inverted. This decomposition also provides slowness and polarization curves for downgoing P/SV and upgoing P/SV for the full offset. Then, anisotropic information can be extracted by the downgoing P curve. In the end, in order to summarize the anisotropic effect in the formations, the results from all four methods are combined.

4.3. Validation results

4.3.1. Well 7220/8-1

For performing verification, a test well should be chosen. Because the aim is to extract horizontal information using vertical measurements, this reference well should be drilled in the vertical direction. We have chosen an exploration well 7220/8-1, which has Sonic Scanner measurements and Walk-Away VSP to be used for validation of the model's performance. This well was a discovery well drilled by Statoil (now Equinor) with a maximum inclination of 3.2° (so, it is a vertical well) in the Johan Castberg field (NPD n.d). The field is located just west of the Polheim Sub-platform and Loppa High in the Barents Sea (NPD n.d, Naghiyev 2021). The purpose was to assess the economic volume of hydrocarbons and to establish oil/gas contacts in the Stø and Nordmela formations in the Skrugard Prospect (NPD n.d, Naghiyev 2021). The formation consists of Tertiary and Cretaceous claystone and sandstone and upper Jurassic claystone above the reservoir, Jurassic sandstone within Stø, Nordmela, and Tubåen formations, and Triassic sandstone within Fruholmen and Snadd formations (NPD n.d). As discussed above, the primary target was to penetrate within the top Stø Formation at 1253 m and the top Nordmela Formation at 1331 m (NPD n.d). They contained a 37 m thick gas column (GOC = 1289 m) and an 83 m thick oil column (OWC = 1372 m) (NPD n.d). Very good hydrocarbon shows were seen during drilling in the Stø and Nordmela formations (NPD n.d). Dataset is illustrated in Figure 15 and Figure 16. The sections that contain hydrocarbon are highlighted in gray.

In addition to the measurement available, the clay content measurement is necessary to estimate since it is one of the main inputs to our proposed model. Because the elemental spectroscopy log is only available for the overburden section, the clay content calculated has been done based on the Neutron-Density porosity method proposed by La Vigne et al. 1994. Since the conventional well logging tools and Sonic Scanner provide all the velocity (or slowness) and the formation density data the model requires, no empirical methods are used.

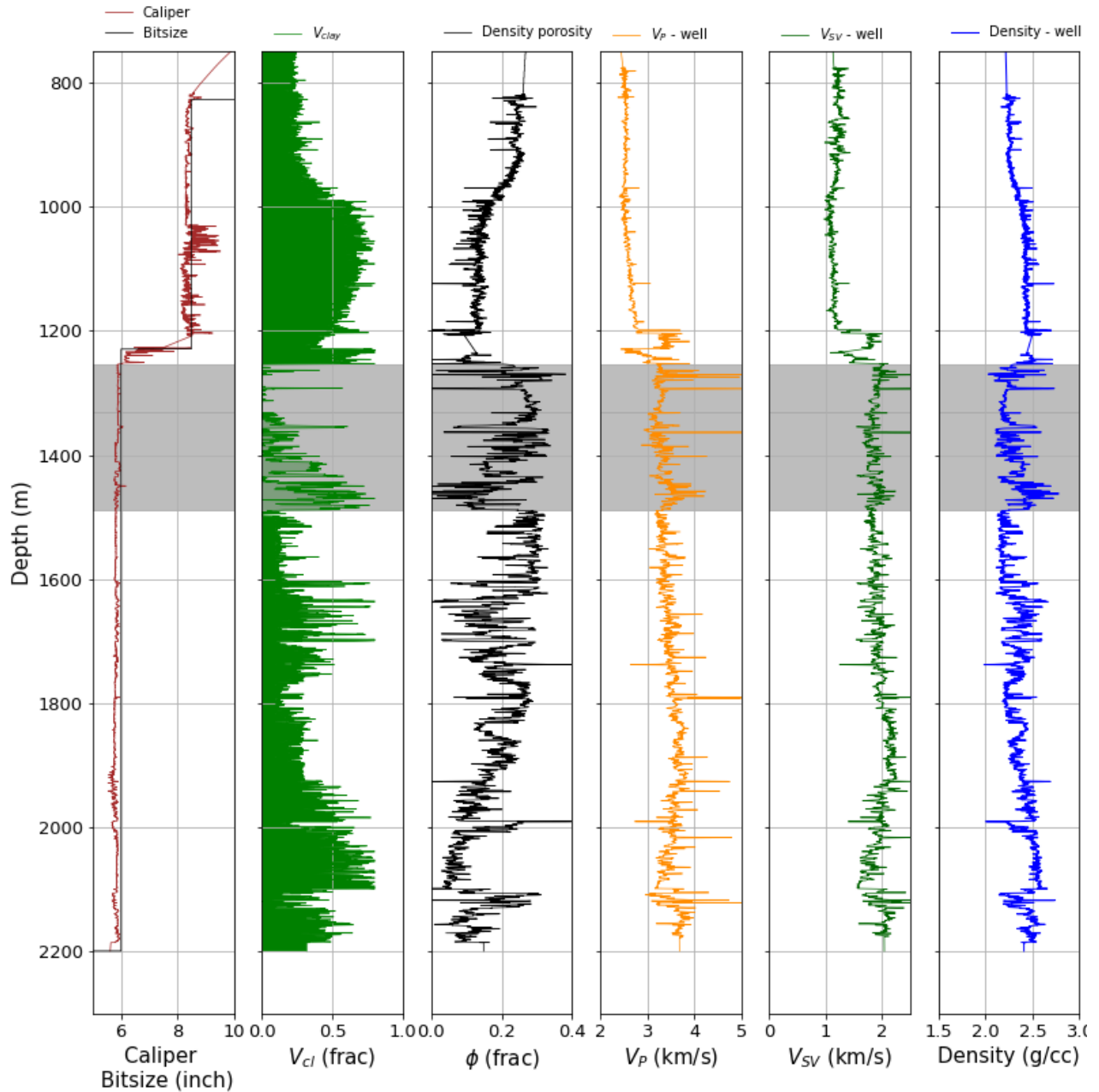


Figure 15. Overview of well 7220/8-1. From left to right: Caliper (brown) & Bit size (black), Clay content (green), density porosity (black), Vertical P-wave velocity (orange), SV-wave velocity (dark green), Formation density (blue). Hydrocarbon zones are highlighted in gray.

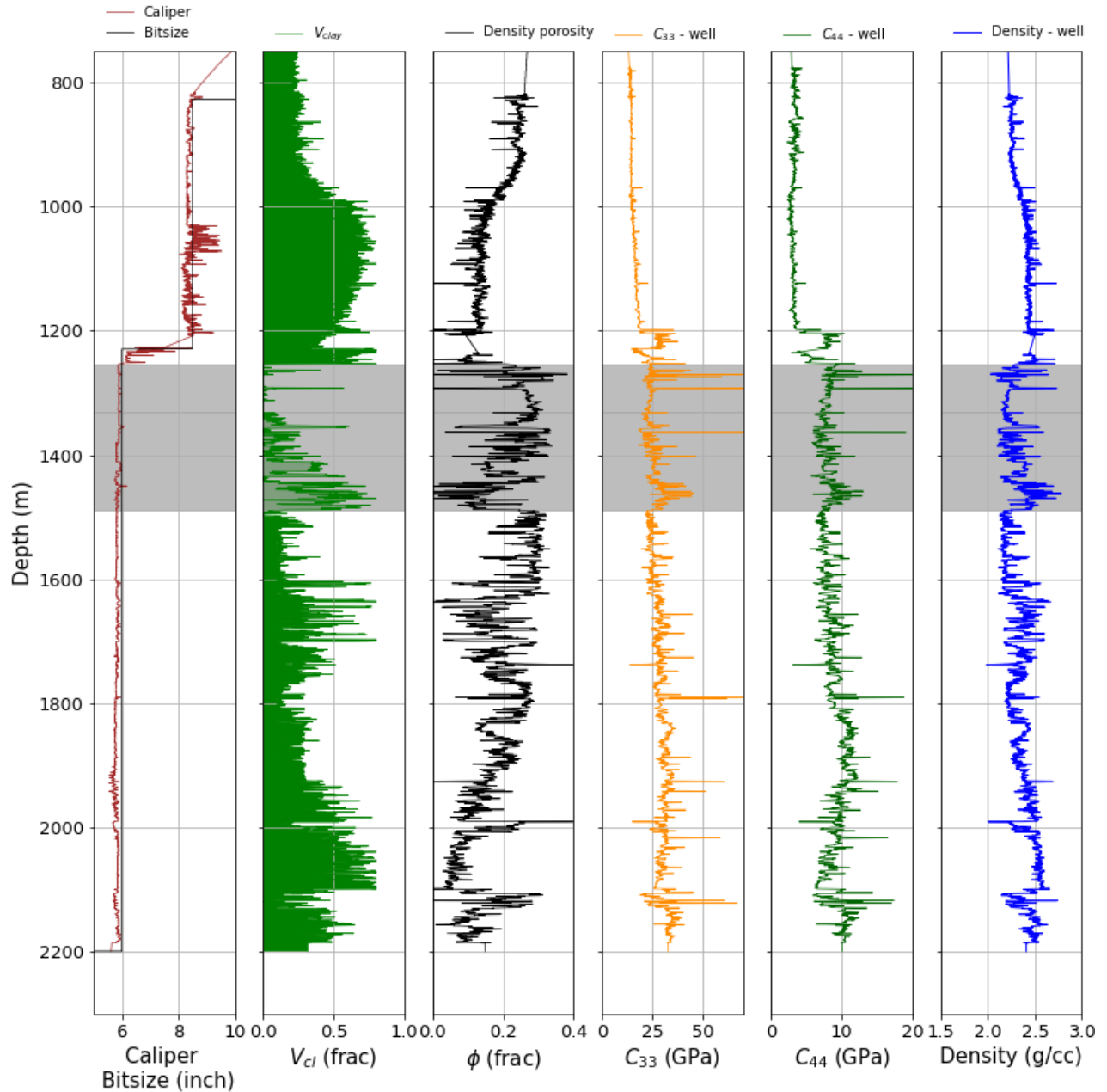


Figure 16. Well log data from 7220/8-1 including vertical stiffnesses (C_{33} and C_{44}). From left to right: Caliper (brown) & Bit size (black), Clay content (green), Density porosity (black), Vertical P-wave stiffness (C_{33}) (orange), SV-wave stiffness (C_{44}) (dark green), Formation density (blue). Hydrocarbon zones are highlighted in gray.

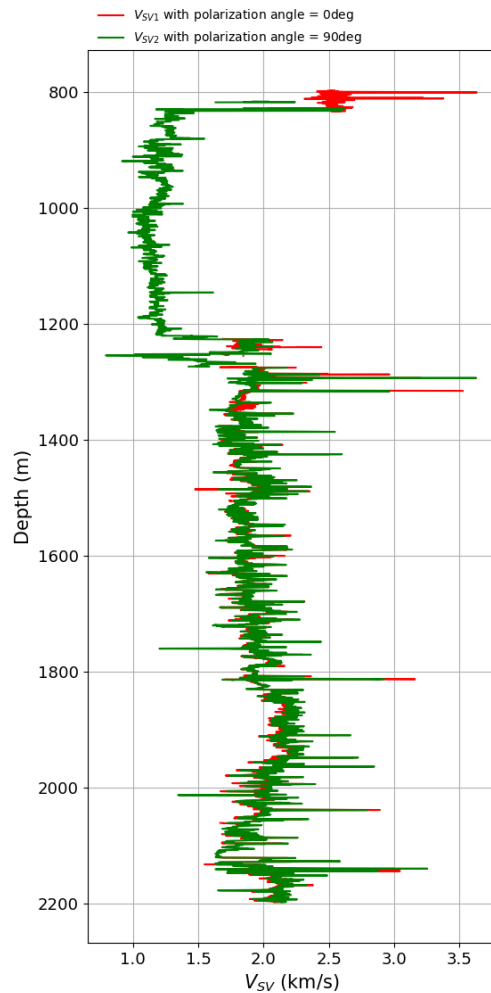


Figure 17. V_{SV} analysis. V_{SV} with polarization angle = 0° (red), V_{SV} with polarization angle = 90° (green)

In order to obtain a reference γ , we have estimated the formation moduli using Norris 1990 Stoneley wave method presented above. Then, using V_{SV} measurement presented in Figure 17, a reference γ has been extracted. This γ will be a base measurement for comparison with model-predicted γ in order to evaluate the predictability of the model. The reference γ together with Stoneley-wave measurement used are presented in Figure 18.

From Sonic Scanner, a set of sonic slowness measurements available are: Vertical P – wave, Vertical S-wave with polarization angle at 0° , Vertical S – wave with polarization angle at 90° , Horizontal S – wave, and Stoneley wave. These measurements were converted to velocities. Additionally, in order to achieve dimensional consistency, the velocities are shown in km/s instead of f/us.

We can compare vertical S-wave velocities with different polarization angles to validate that the medium is a VTI medium. The match between two velocities with different polarization angles will indicate no or little difference in velocities in the same plane but with further polarization. This will validate the VTI medium's requirements since the variation should be in the vertical plane, not horizontal. Because in V_{SV} velocities, the polarization is parallel to the bedding, this theory can be proved using them. Figure 17 illustrates this correlation. From 1200 m till the end of the borehole where we have data in both polarization angles, very good match was observed. Thus, we can assume the VTI medium in this data.

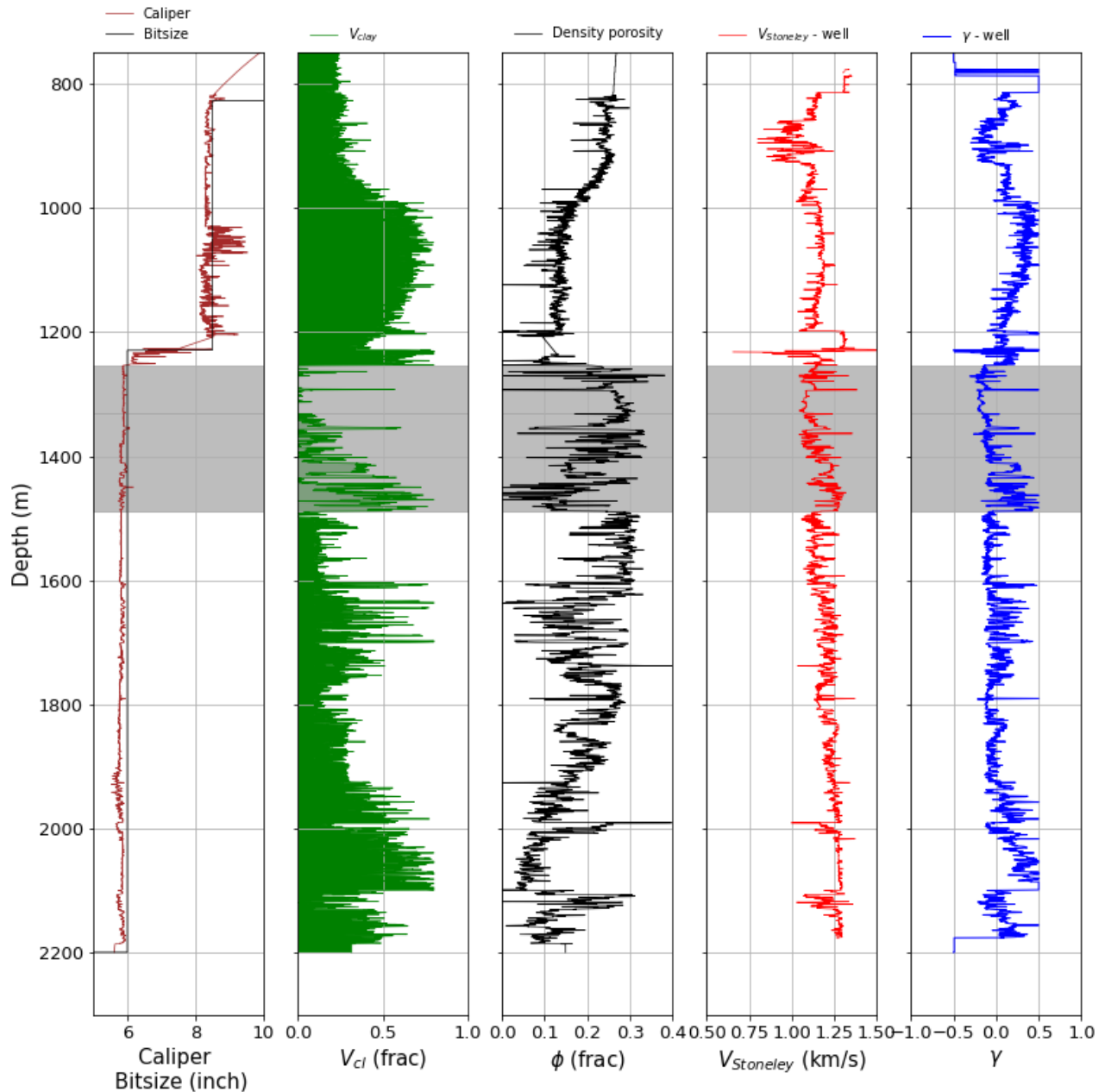


Figure 18. Well log data from 7220/8-1 including Stoneley wave and reference γ . From left to right: Caliper (brown) & Bit size (black), Clay content (green), Density porosity (black), Stoneley-wave velocity (red), Formation γ generated by Stoneley wave (blue). Hydrocarbon zones are highlighted in gray.

In addition to conventional well logging together with Sonic Scanner, Walk Away Vertical Seismic Profiling survey has been performed in the discussed well. Since the primary objective of Vertical Seismic Profiling was to estimate anisotropy in Cretaceous and Tertiary overburden formations, the results can be used for as a reference for our verification. The survey done by 16 receivers placed below base Tertiary overburden (Schlumberger 2012). The survey was conducted in two walkaway lines, in dip direction, and in strike direction (Schlumberger 2012). As expected, the data acquired in dip direction is better to tie to the data than that in strike direction. The

anisotropic information has been extracted combining four methods discussed above. The data we used represent interval properties and was averaged over the receive interval. The intervals after receivers were considered as isotropic. Figure 19 presents the VSP data along with borehole data. These anisotropic parameters ϵ and δ will be used as reference measurements like Stoneley-wave derived γ .

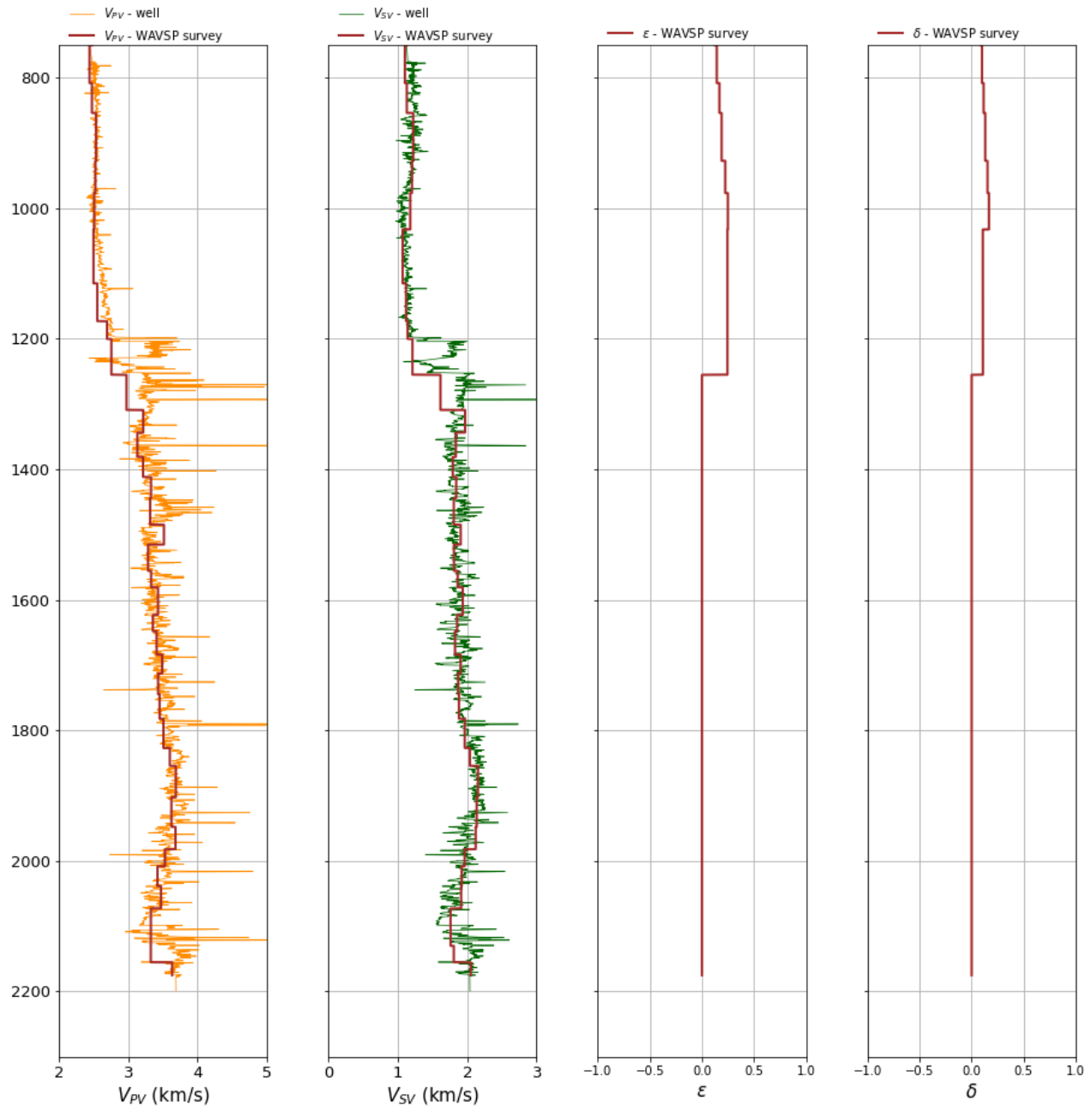


Figure 19. Vertical velocities (V_P and V_S) including data from Walkaway Vertical Seismic Profiling. V_{PV} from well (1st track, orange), V_{PV} from WAVSP (1st track, brown), V_{SV} from well (2nd track, green), V_{SV} from WAVSP (2nd track, brown). WAVSP ϵ (3rd track, brown), WAVSP δ (4th track, brown)

Since all the references are set, the prediction can be performed. As mentioned above, because the elemental spectroscopy is available in the shallow depths, neutron – density porosity method (see Equation 3.13) is used in the clay content calculation. The density porosity is calculated using Equation 3.12. The input vertical stiffnesses are derived using the available Sonic Scanner vertical velocity and formation density. Additionally, the model needs K_0 . In isotropic sections, it has been deduced using velocity measurement (see Equation 3.9). In the shaley section, a δ has been added (see Equation 3.10). Practical applications reveal that considering $\delta = 0.15$ in high shaley cases and $\delta = 0.05$ in moderate shaley cases gives acceptable results.

Our prediction model has been applied to well 7220/8-1, and the results are in Figure 20. The uncertainty is added using the classical propagation of error method presented in Appendix C. The fluid substitution is not performed on purpose in order to see our model's effect on hydrocarbon-filled sections. Although the model covers the anisotropy causes such as intrinsic and stress-induced anisotropy, it does not include layer-induced anisotropy. As discussed in the theory chapters, layer-induced anisotropy is added using Backus averages. Therefore, after prediction, the result has been Backus-averaged with an averaging window of 1 m. The averaging window has been chosen carefully not to overlook the boundary effects.

By comparing with the Sonic Scanner γ , one can see from Figure 20 that the match between predicted and log-derived values are really good. Especially in the deeper sections of the log where the formation can be associated as shaly sands, it covers almost the true γ . Even though in the reservoir section, hydrocarbons affect the actual readings a lot and some mismatches are present, the model performs pretty well. As expected, the model results in a negative anisotropy in the sand sections. On the other hand, the positive anisotropy in clayey sections is also present. This shows that the formularization of our prediction model enables us to get good coverage of elastic anisotropy.

Coming to the discrepancies, the mismatches in the reservoir sections are expected since the model is designed to be used in water-wet formations, yet the prediction is a bit off-track in the thick overburden shale pack. The first reason is the quality of the measurement at the discussed interval. From Figure 20, it is clearly seen that caving is presented in this thick shale which can significantly influence the measurements obtained. The other more critical cause of this mismatch is how the model has been defined in this section. Because the parameters that introduce intrinsic and stress-induced anisotropy are what can affect the result, the moderately big mismatch on thick shale can be dependent on either K_0 or V_{cl} . The effect of high V_P/V_S on K_0 can be the first cause of this discrepancy. On the maximum V_P/V_S , K_0 also becomes higher. Considering the small number of $(1 - V_{cl})$ on the clayey interval, the multiplication with higher K_0 will boost the predicted result. The analysis has shown that the effect of δ in K_0 definition is minimal. Another, but more powerful influence is from clay content. It is seen that the general behavior of the predicted measurement mimics the clay content. Considering the measurements are divided to $(1 - V_{cl})$ for addressing intrinsic contribution, this value will be low in the overburden section. Because of division to a low value, the overall result will be too high. Thus, the precision of clay

content calculation will directly influence the accuracy of the prediction result. That's why it is recommended to estimate the clay content as true as possible from lithology logs. However, as shown in previous chapters, reliable empirical methods like La Vigne et al. 1994 are the backup plan. Although we have used La Vigne et al. 1994's method here, the comparison shows that except for the thick shale section, the prediction coverage is excellent. In the later chapters, I will discuss La Vigne et al. 1994's method thoroughly and present a way to improve these results.

Since the comparison results of γ with Sonic Scanner data show a good match, the same comparison is necessary for other Thomsen parameters. However, Sonic Scanner does not enable us to derive a reference ε or δ . The only reference measurement for these parameters is VSP data. In VSP data, all the formations after overburden thick shale were assumed as isotropic formations (so, ε and $\delta = 0$). But it is still possible to perform a comparison and verify the general behavior. Figure 20 shows the comparison of predicted ε and δ with VSP data. For δ , the linear approximation resulting from analyzing Thomsen 1986's data, $\delta = 0.352467\varepsilon$ has been used. As expected, the prediction results show positive anisotropies for overburden shale intervals. The comparison with VSP data confirms this behavior. Although VSP data shows no anisotropy in the reservoir part, from anisotropy theory, it is well-known that these formations are experiencing negative anisotropy. Fortunately, our prediction model successfully confirms the negativity of anisotropy in the non-clay sections. Since the predictability of our model in γ is outstanding and both models were derived using the same approach, it would be logical to assume ε model also achieves a good prediction. When comparing of δ from our model and VSP data, we still observe good a correlation with the available VSP data.

The uncertainty estimation has been performed using Appendix C, the propagation of error method by the derivatives of each term and their random errors (Lyons 1991). Because of the complexity of defining the stress contribution in C_{66} , the uncertainty related to γ is higher than ε . Although this uncertainty window may seem narrow, it provides a good prediction range.

It is also worth noting that the reference γ is derived from Norris 1990's method using Stoneley wave measurements. Thus, it also introduces some degree of uncertainty. That's why when assessing the comparison, this should be kept in mind.

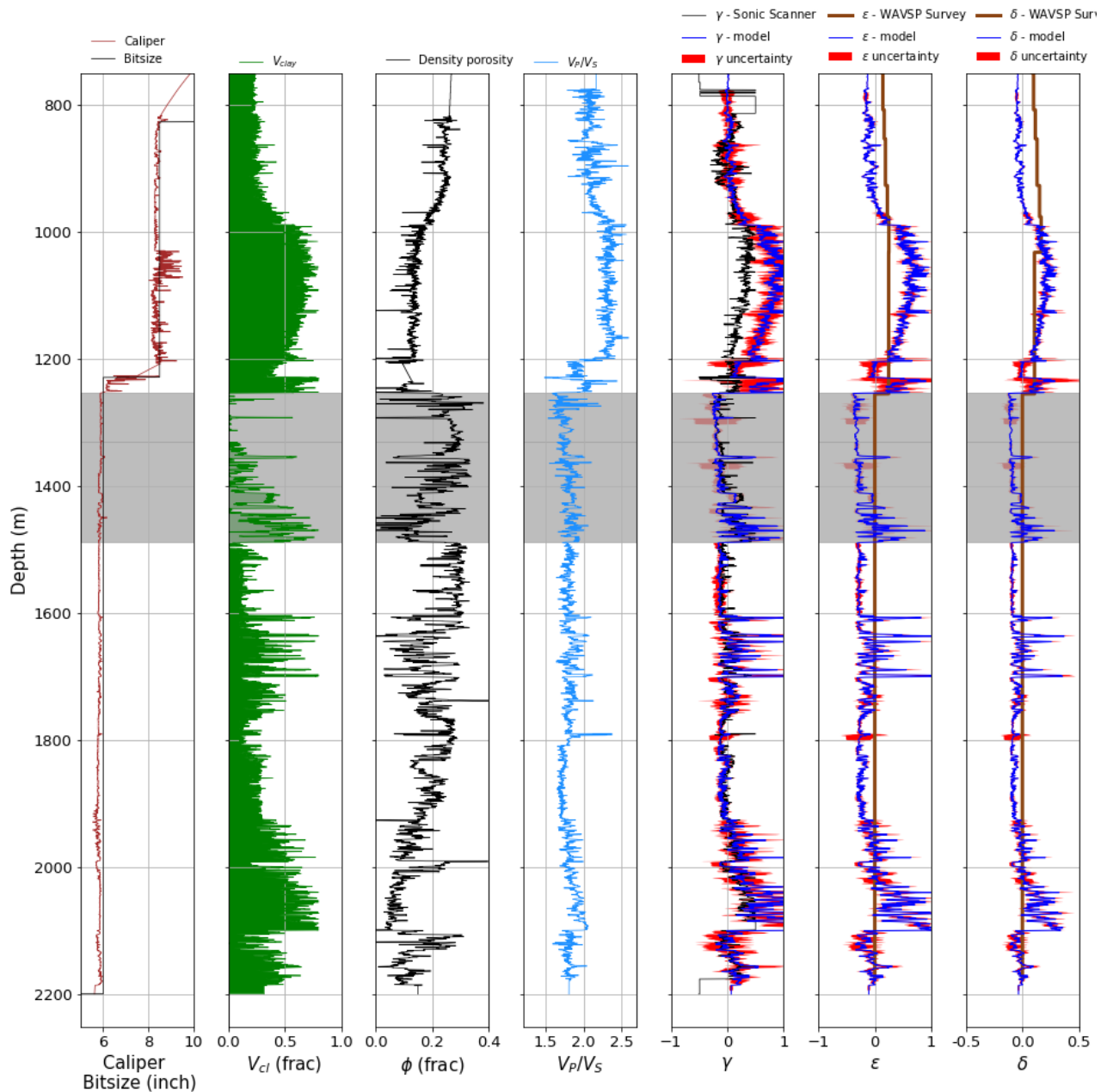


Figure 20. Prediction results of well 7220/8-1. From left to right: Caliper (brown) & Bit size (black), Clay content (green), Density porosity (black), V_p/V_s ratio (light blue), γ , ϵ , δ . Hydrocarbon zones are highlighted in gray.

γ track (5th track): Black – formation γ generated by Stoneley wave, Blue – predicted γ generated by our prediction model. Red – uncertainty of prediction.

ϵ track (6th track): Brown – ϵ by Walk-Away Vertical Seismic Profiling, Blue – predicted ϵ generated by our prediction model. Red – uncertainty of prediction.

δ track (7th track): Brown – δ by Walk-Away Vertical Seismic Profiling, Blue – predicted δ generated by our prediction model. Red – uncertainty of prediction.

4.3.2. Well 7220/7-1

In order to verify the prediction done by well 7220/8-1, an adjacent well, well 7220/7-1, which also has Sonic Scanner data, has been chosen. This well is also a part of the Johan Castberg field located in the Barents Sea. It was drilled by Statoil (now Equinor) in the southwest of 7220/8-1 discovery well and the west of Loppa High in the Barents Sea with a maximum inclination of 6° (a vertical well) (NPD n.d). The main purpose was to examine the hydrocarbon potential in Stø, Nordmela, and Tubåen Formations and to test the presence and quality of sandstones in the lower Triassic Fruholmen Formation (NPD n.d). The findings were also compared and proved by seismic data (NPD n.d). The well has penetrated all the formations aging from the Quaternary to Triassic periods. The top of the hydrocarbon-bearing target reservoir Stø Formation has been found at 1741 m. GOC was detected at 1788m and OWC at 1916 m, and seven cores were cut in the Stø, Nordmela, and Tubåen Formations covering hydrocarbon and water-bearing zones. Dataset is illustrated in Figure 21 and Figure 22. The formations that contain hydrocarbon are highlighted by gray. Like well 7220/8-1, the clay content calculation has been done using the Neutron-Density porosity method proposed by La Vigne et al. 1994. It is still worth noting that in the high shaley sections, the logging tool has experienced high caving up to 5 inches (Figure 21).

A reference γ has been extracted using Norris 1990 Stoneley wave method presented in earlier sections. The reference γ , together with the Stoneley-wave measurement used, are shown in Figure 23. Because the connection with logging tool has been lost for some layers right before the reservoir, the measurement of Stoneley wave has not been acquired in this section.

Unfortunately, in well 7220/7-1, the Walk-Away Vertical Seismic Profiling has not been done. So, there is no source for obtaining reference measurements for ε and δ . So, the prediction and comparison done by γ is the only way to prove and verify the model's predictability.

Using the vertical measurements, clay content calculation and predefined δ for K_0 , the anisotropy prediction model has been applied to well 7220/7-1. Figure 24 shows the prediction results using well 7220/7-1. The uncertainty has been added with the same principle used before. Layer-induced anisotropy effects have been included using Backus theory with an averaging window of 1 m.

The comparison of γ predicted by model and derived by Sonic Scanner has shown us that the model is still performing pretty well. The model predicts close values to the well readings in the upper section of the well 7220/7-1. As the well enters the high-clayey section, the mismatch starts to expand. One of its direct reasons is that the logging tool does not stabilize because of the caving present in the interval. That's why the tool's reading is not as reliable as in deeper sections. Another reason, as discussed with the well 7220/8-1, is the causes related to the parameters V_{cl} and K_0 . Although there are some mismatches in the upper and overburden section of the well, the prediction is almost perfect in the deeper sections. This prediction can again verify the reliability of the model.

Since no reference measurements for ε and δ are available, a similar comparison cannot be made. Yet, because of a good correlation of results from predicted γ and reference γ in moderately clayey sections, the same performance can be expected for ε and δ . As expected, the model predicts a negative value in sand intervals and vice-versa for clayey intervals. This also proves that the predictability of the model is remarkable.

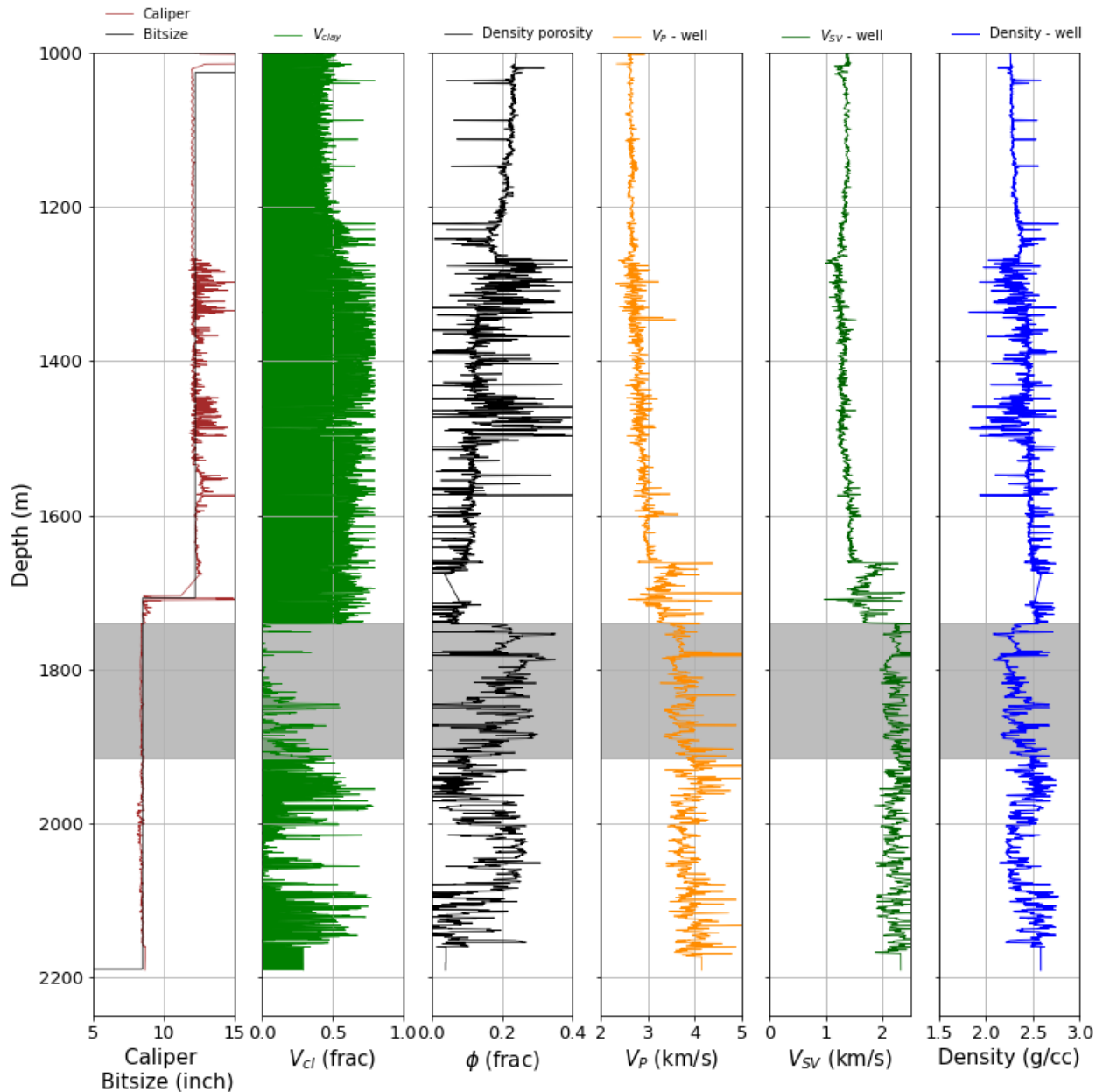


Figure 21. Overview of well 7220/7-1. From left to right: Caliper (brown) & Bit size (black), Clay content (green), density porosity (black), Vertical P-wave velocity (orange), SV-wave velocity (dark green), Formation density (blue). Hydrocarbon zones are highlighted in gray.

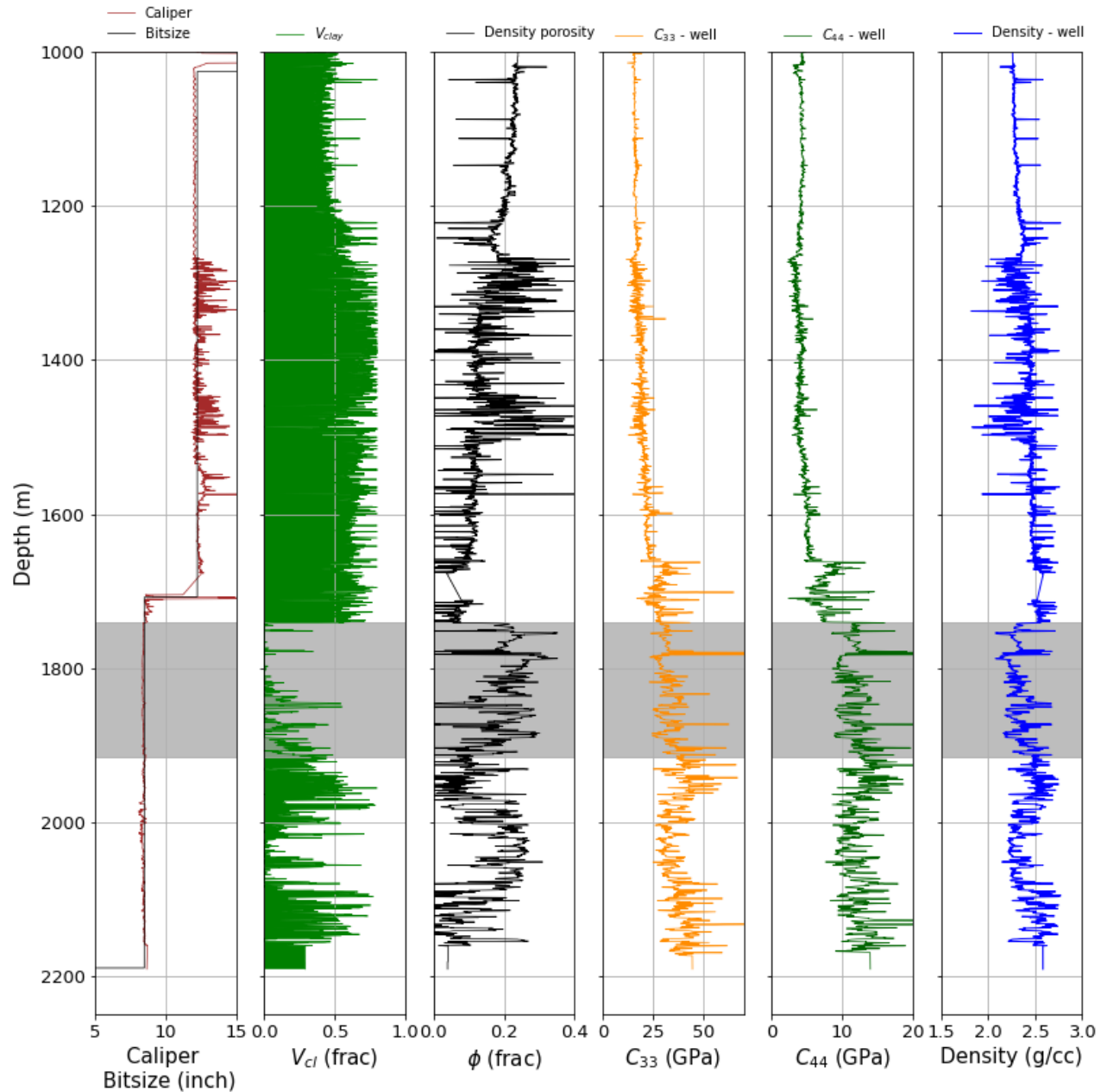


Figure 22. Well log data from 7220/7-1 including vertical stiffnesses (C_{33} and C_{44}). From left to right: Caliper (brown) & Bit size (black), Clay content (green), Density porosity (black), Vertical P-wave stiffness (C_{33}) (orange), SV-wave stiffness (C_{44}) (dark green), Formation density (blue). Hydrocarbon zones are highlighted in gray.

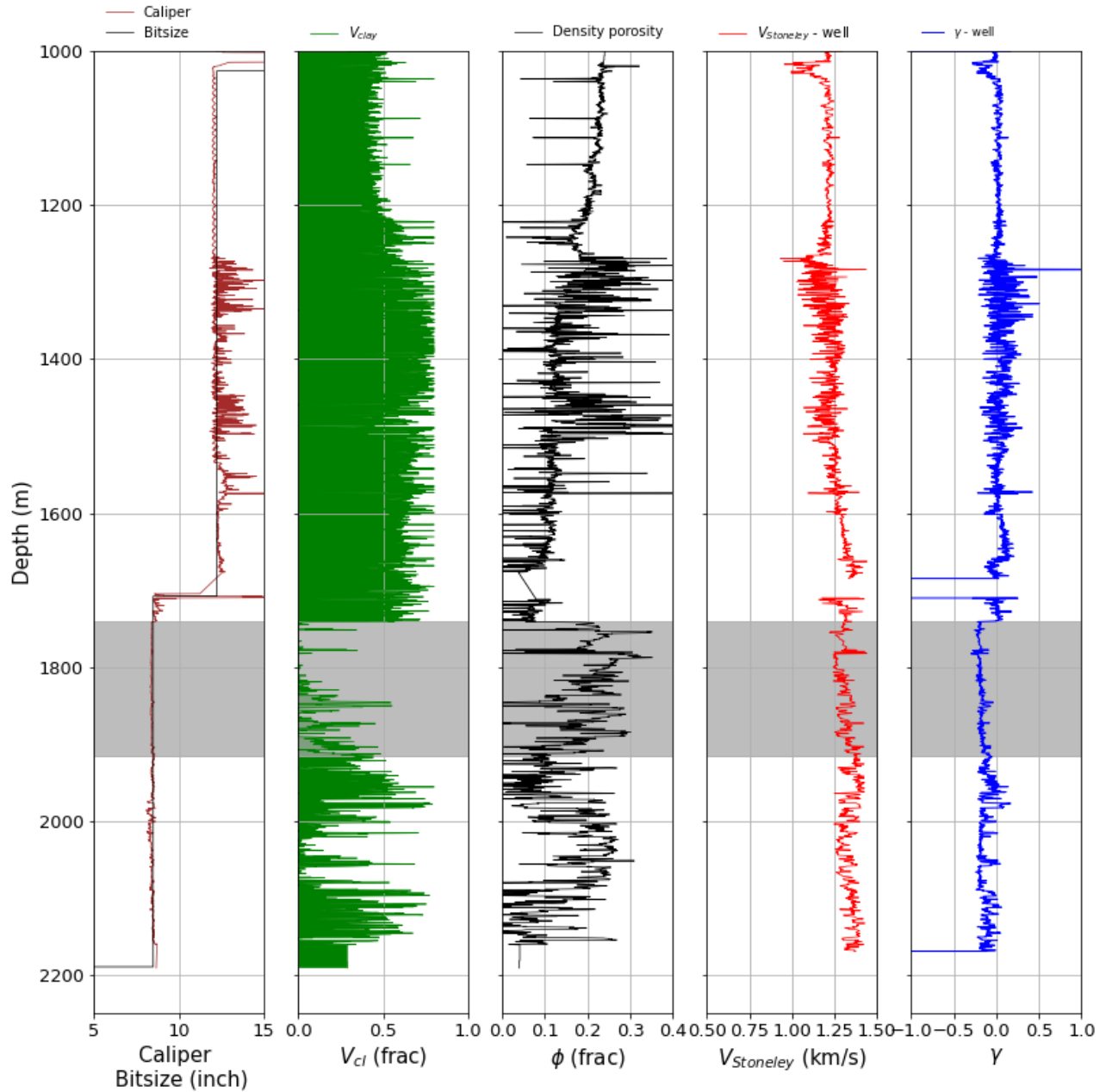


Figure 23. Well log data from 7220/7-1 including Stoneley wave and reference γ . From left to right: Caliper (brown) & Bit size (black), Clay content (green), Density porosity (black), Stoneley-wave velocity (red), Formation γ generated by Stoneley wave (blue). Hydrocarbon zones are highlighted in gray.

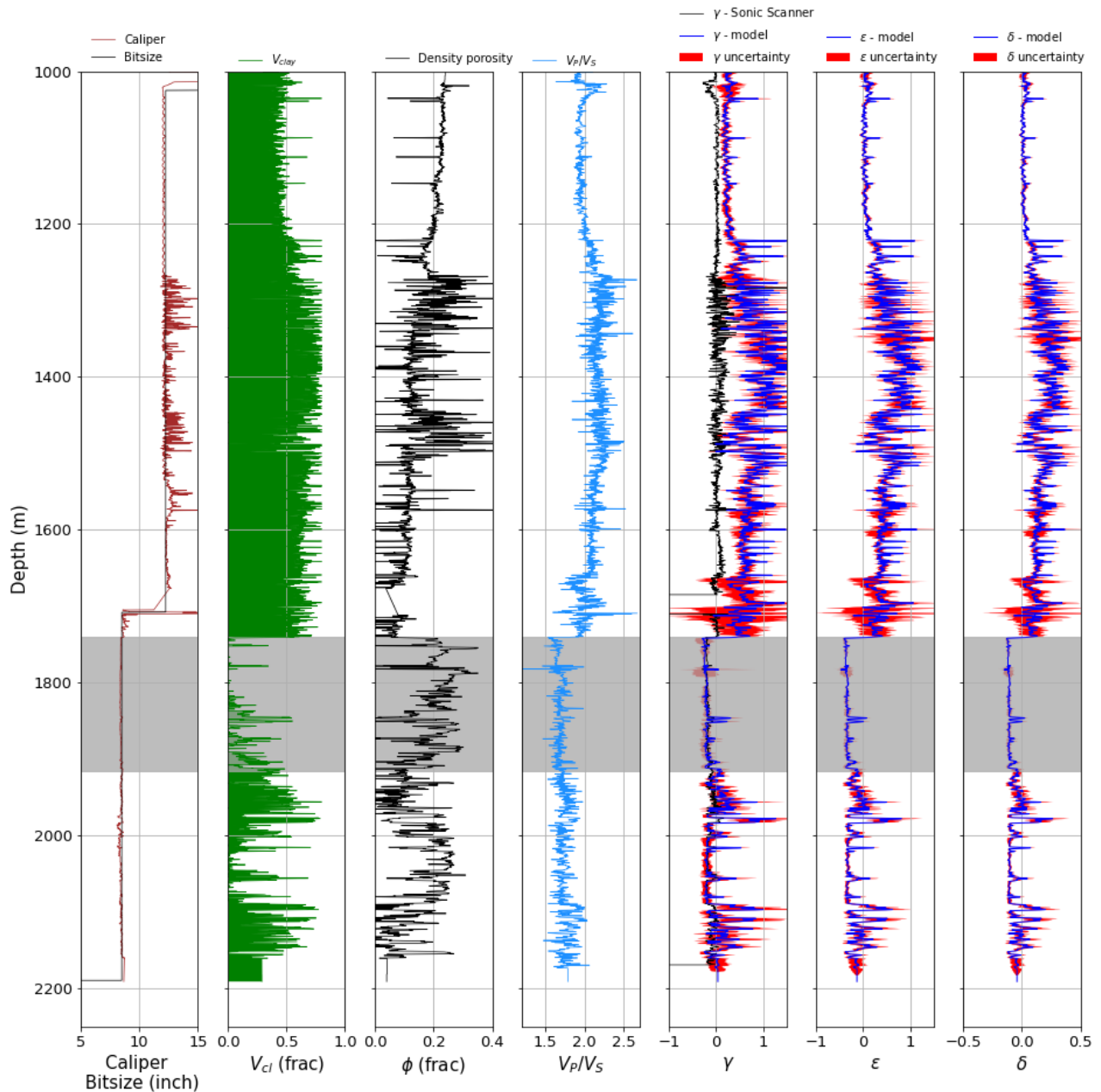


Figure 24. Prediction results of well 7220/7-1. From left to right: Caliper (brown) & Bit size (black), Clay content (green), Density porosity (black), V_p/V_s ratio (light blue), γ , ϵ , δ . Hydrocarbon zones are highlighted in gray.

γ track (5th track): Black – formation γ generated by Stoneley wave, Blue – predicted γ generated by our prediction model. Red – uncertainty of prediction.

ϵ track (6th track): Blue – predicted ϵ generated by our prediction model. Red – uncertainty of prediction.

δ track (7th track): Blue – predicted δ generated by our prediction model. Red – uncertainty of prediction.

4.3.3. Well 7220/10-1

From the prediction results of wells 7220/8-1 and 7220/7-1, we have concluded that the model works remarkably in the shaly sand intervals. That's why it would be interesting to see the prediction results in a well with high shaly sand content. For this purpose, one of the adjacent wells, well 7220/10-1 that also has Sonic Scanner, has been chosen. The well was drilled on Salina Prospect by Eni Norge (now Vår Energi) in the southwest end of the Loppa High in the Barents Sea with a maximum inclination of 0.9° (a vertical well) (NPD n.d). The main purpose was to verify the hydrocarbon in the Knurr and Hekkingen formations (Early Cretaceous to Late Jurassic reservoir rocks) and Stø, Nordmela, Tubåen, and Fruholmen formations (Middle to Early Jurassic reservoir rocks) (NPD n.d). The well has penetrated a 134 m reservoir that consists of sandstones and siltstones in the Kolmule Formation of the Aptian Age. The upper 36 m contained gas and had 96 % net-to-gross. From the pressure gradient test, GOC has been found at 1293 m. The second reservoir, which consisted of 132 m of sandstones, was encountered at 1513.5 m. The upper 53 m was gas bearing and had 90 % net-to-gross. GOC has been detected at 1479 m. The water-bearing sandstone reservoirs were found in Nordmela, Tubåen, Fruholmen, and Snadd Formations. Dataset is illustrated in Figure 25 and Figure 26. The formations that contain gas are highlighted by gray. Like the other two wells, the clay content calculation has been done using the Neutron-Density porosity method proposed by La Vigne et al. 1994.

Like other two wells, a reference γ has been extracted using Norris 1990 Stoneley wave method. Figure 27 illustrates the reference γ together with the Stoneley-wave measurement used. Unfortunately, in well 7220/10-1, the Walk-Away Vertical Seismic Profiling has not been done. So, like well 7220/7-1, there is no source for obtaining reference measurements for ε and δ .

The model has been applied to the well 7220/10-1 using its Sonic Scanner data, clay content calculation, and predefined δ for K_0 . The results are available in Figure 28. The uncertainty has been added with the same principle used before. Layer-induced anisotropy effects have been included using Backus theory with an averaging window of 1m.

Figure 28 has demonstrated an almost excellent fit between γ predicted by model and derived by Sonic Scanner. Although the overburden effect found by other wells is still applicable in the intervals at 1400 m, the performance of the model is outstanding. The comparison made in this well has made us more confident in the model's performance.

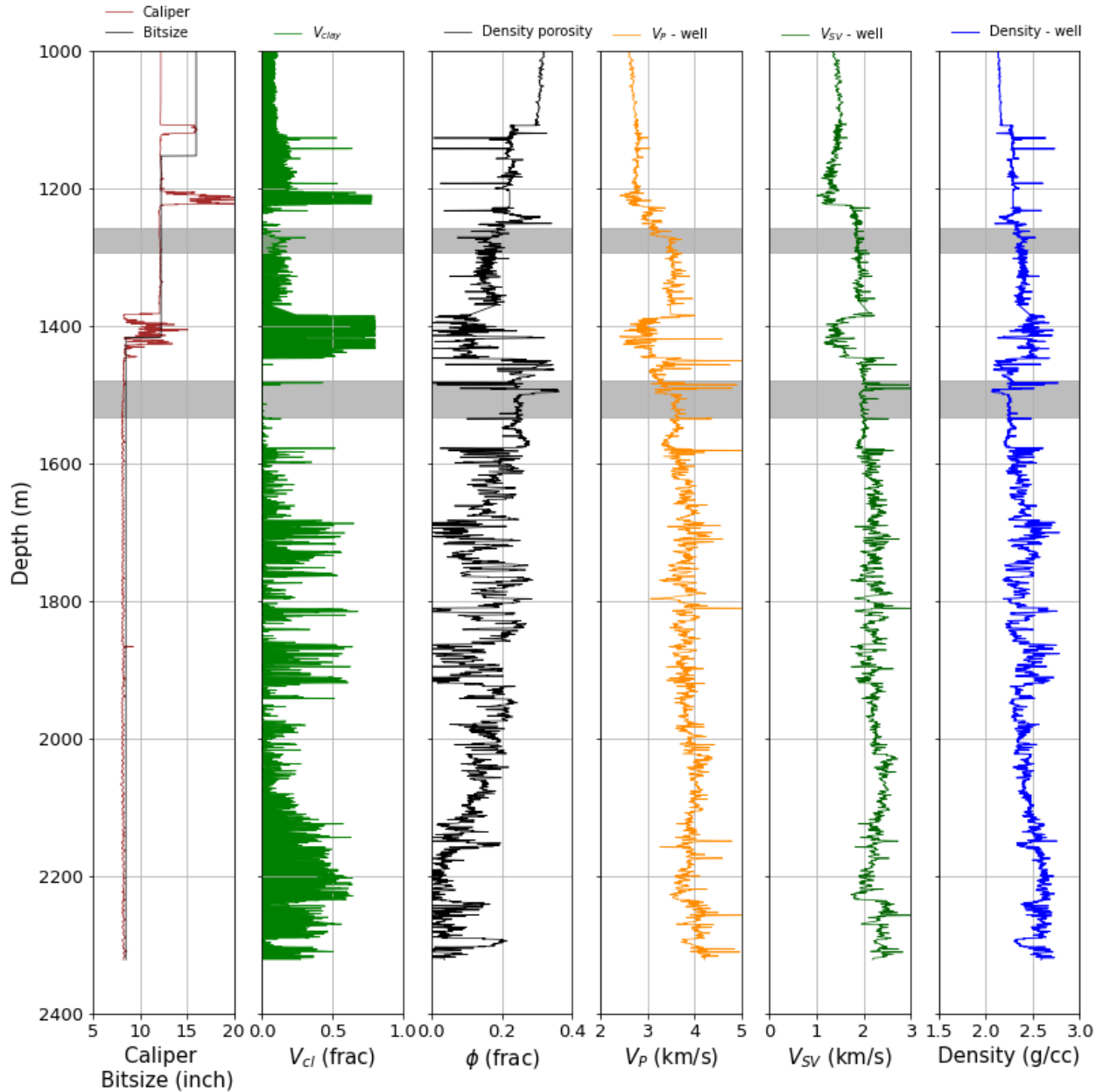


Figure 25. Overview of well 7220/10-1. From left to right: Caliper (brown) & Bit size (black), Clay content (green), density porosity (black), Vertical P-wave velocity (orange), SV-wave velocity (dark green), Formation density (blue). Hydrocarbon zones are highlighted by gray.

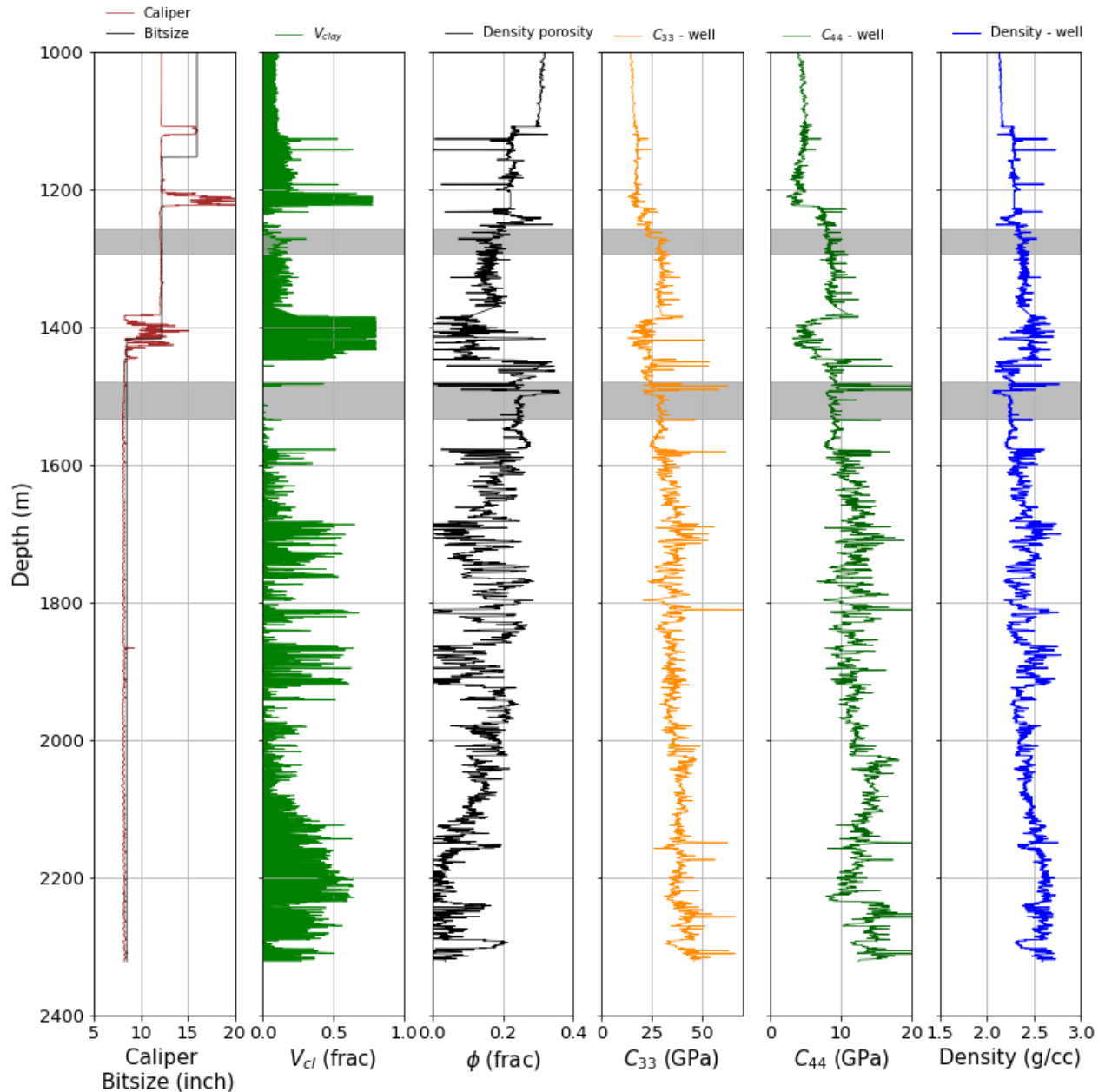


Figure 26. Well log data from 7220/10-1 including vertical stiffnesses (C_{33} and C_{44}). From left to right: Caliper (brown) & Bit size (black), Clay content (green), Density porosity (black), Vertical P-wave stiffness (C_{33}) (orange), SV-wave stiffness (C_{44}) (dark green), Formation density (blue). Hydrocarbon zones are highlighted by gray.

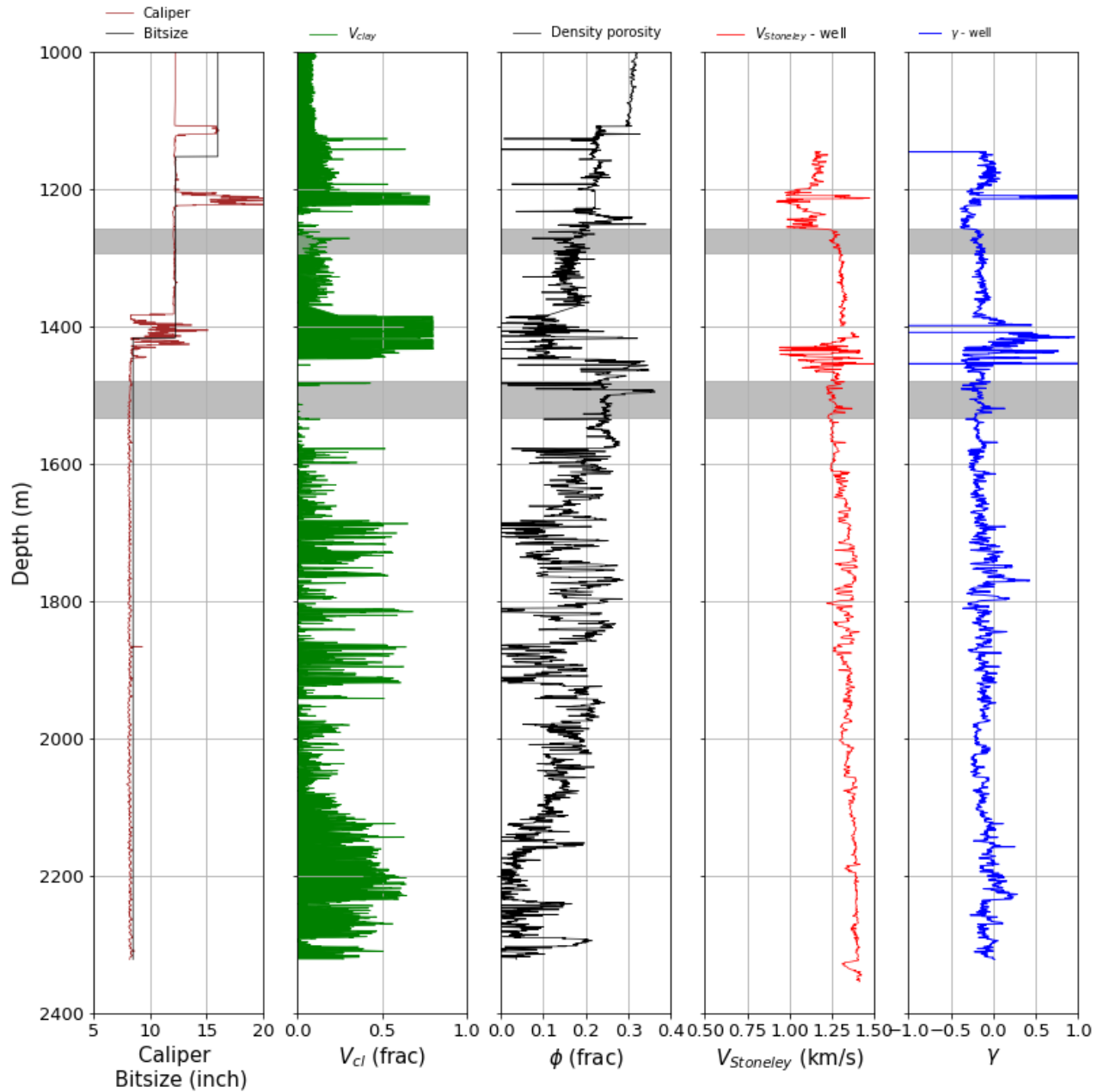


Figure 27. Well log data from 7220/7-1 including Stoneley wave and reference γ . From left to right: Caliper (brown) & Bit size (black), Clay content (green), Density porosity (black), Stoneley-wave velocity (red), Formation γ generated by Stoneley wave (blue). Hydrocarbon zones are highlighted by gray.

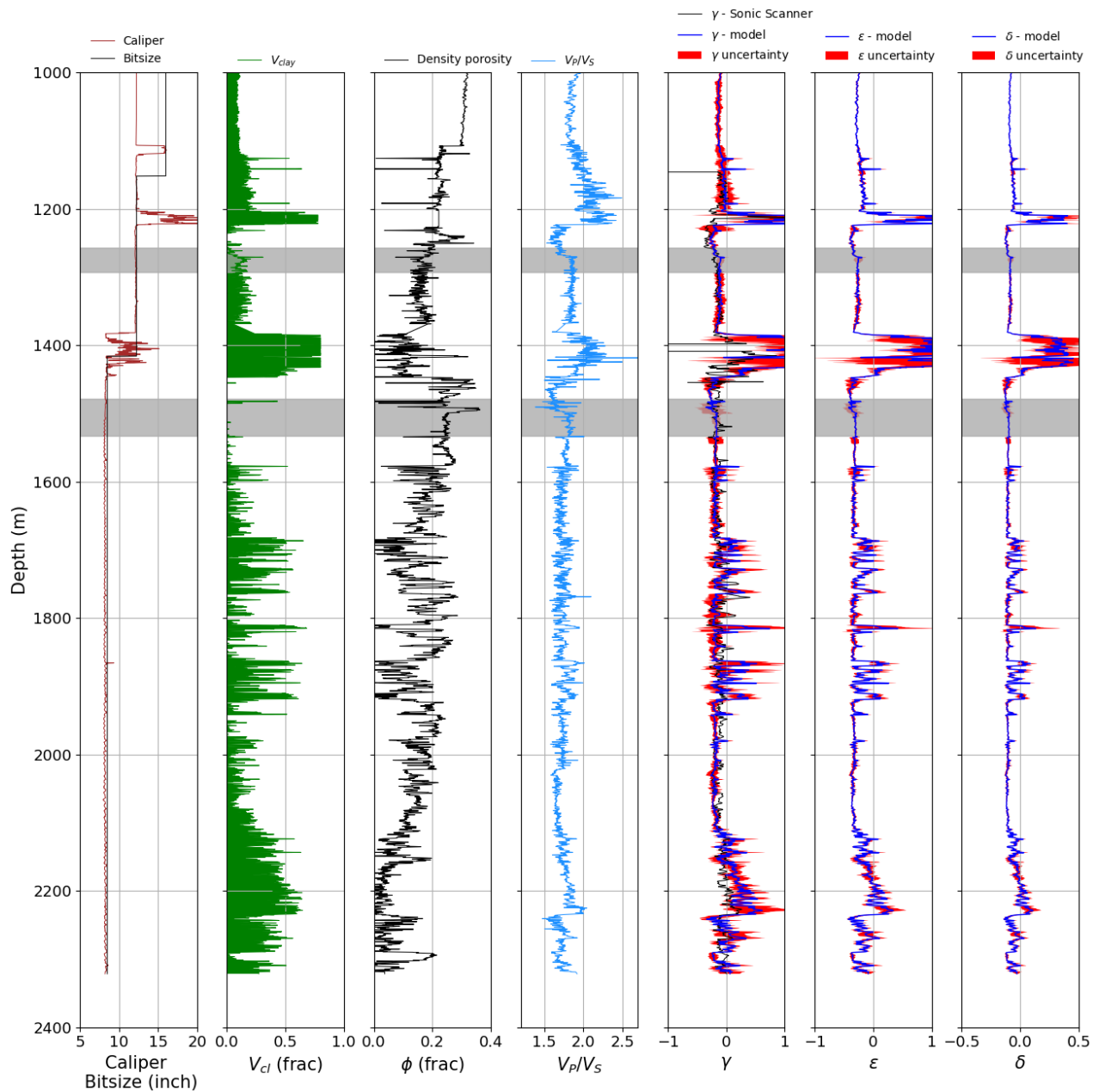


Figure 28. Prediction results of well 7220/10-1. From left to right: Caliper (brown) & Bit size (black), Clay content (green), Density porosity (black), V_p/V_s ratio (light blue), γ , ϵ , δ . Hydrocarbon zones are highlighted by gray.

γ track (5th track): Black – formation γ generated by Stoneley wave, Blue – predicted γ generated by our prediction model. Red – uncertainty of prediction.

ϵ track (6th track): Blue – predicted ϵ generated by our prediction model. Red – uncertainty of prediction.

δ track (7th track): Blue – predicted δ generated by our prediction model. Red – uncertainty of prediction.

Chapter 5. Impact of anisotropy on seismic response

Now, we have successfully predicted the elastic anisotropy in well 7220/8-1, well 7220/7-1, and well 7220/8-1. In the further step, it would be interesting to see the predicted anisotropic effects in associated seismic sections. This chapter will account for the isotropic and anisotropic forward modeling and explain the effect by AVO/AVA analysis. Because we do not have access to the real seismic done in the field, the analysis has been done by synthetic seismic gathers.

Generally, in conventional seismic reservoir characterization, methods such as forward modeling, AVO/AVA analysis/inversion, and seismic interpretation consider a model made of a stack of isotropic layers (Asaka 2018). However, as discussed in the theory and introduction chapters, assuming elastic isotropy in these applications can cause severe issues in characterization. Ferla et al. 2013 give a real data example on AVO response that has been influenced by velocity anisotropy and discuss how anisotropy can be an answer for pitfalls in AVO interpretation. Sams & Annamalai 2018 have debated the anisotropic effects on synthetic seismic data and why it is not always wise to ignore elastic anisotropy.

5.1. Forward seismic modelling

The primary purpose of forward seismic modeling is to simulate the real seismic data to verify the seismic interpretations. Since we do not have access to the real seismic done in the area, the resulting synthetic section from forward seismic modeling will help to indicate the effect of anisotropy by comparing isotropic and anisotropic gathers. The forward modeling has been done in the Geoview – Hampson-Russell Suite. The ultimate aim is to model the subsurface using the available data to explain the effect of elastic anisotropy. In order to generate this type of model, a basic convolution theory sketched in Figure 29 has been used. According to the theory, two kinds of information are required for generating synthetic data, reflection coefficients of the intervals and seismic pulse/wavelet.

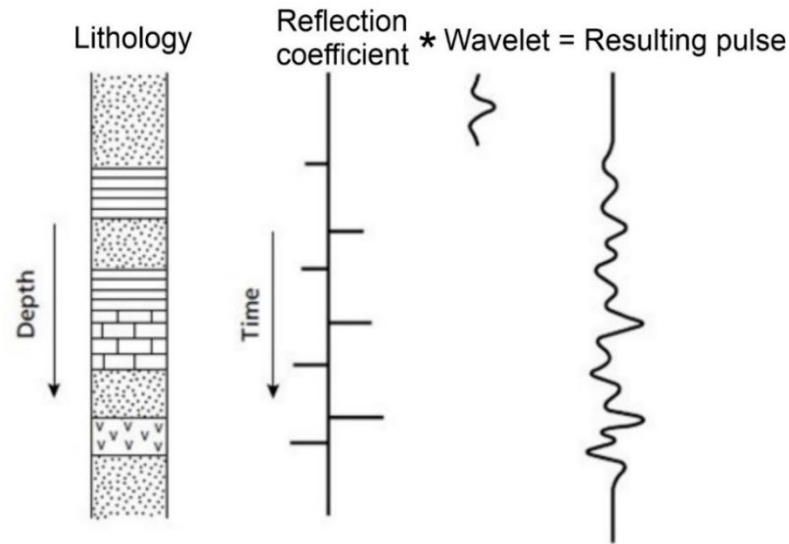


Figure 29. A process of convolution

After importing the prediction results together with the conventional well logs, the AVO synthetics modeling workflow has been run using the appropriate formation density and vertical velocities. Since the real seismic data is inaccessible, it is necessary to use as detailed synthetics as possible. That’s why the Zoeppritz equations in Appendix D have been used to compute the reflection amplitudes as precisely as possible. The Zoeppritz equations will provide us with the reflection amplitudes of the intervals, and then these

amplitudes are convoluted with an appropriate wavelet to generate synthetic seismic data. There are numerous already-defined wavelets used in seismic processing. One of the wavelets commonly used in generating synthetic seismic data is the Ricker wavelet, named after a mathematician Norman Ricker (Robinson & Treidel 2008). Ricker wavelet is a simple, non-causal wavelet that is symmetric at the origin and is a zero-phase signal. The general form of the wavelet is in Equation 5.1. In our forward seismic modeling, a 40 Hz Ricker wavelet is used to generate the synthetic seismic data. The shape of the Ricker wavelet is in Figure 30.

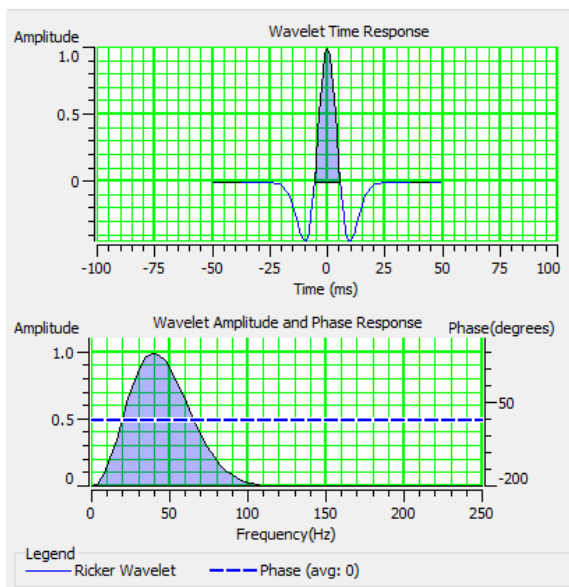


Figure 30. 40 Hz Ricker wavelet

$$(1 - 2\pi^2 f^2 t^2)e^{-\pi^2 f^2 t^2}$$

Equation 5. 1

For better visualization and comparison, the modeling output is a zero-phase, pre-stack, angle-type synthetic seismic data. For covering the whole section of interest, the depth range has

been chosen from 0 to 3000 m. Following the modeling steps described, the output synthetic will be an isotropic synthetic seismic data. However, the anisotropic synthetic section must also be done to perform the comparison. Luckily, when creating the synthetics in Geoview, there is an option to include anisotropy by means of anisotropic parameters. Additionally, in order to produce anisotropic synthetics, elastic anisotropy should be corrected in Zoeppritz equations. Rüger 1997 has given the relevant corrections to classical Zoeppritz equations. The anisotropic Zoeppritz equation used in generating anisotropic synthetic data is presented in Appendix D. Using the workflow explained, Geoview can produce different synthetic seismic data based on interested wave types. However, it is always easy to interpret PP-type synthetic seismic data (P-wave down, P-wave up). Since our primary interest is PP synthetic section, Zoeppritz equations described by Rüger 1997 will only require anisotropic information from ε and δ . Thus, γ will not have any effect on the resulting anisotropic synthetic seismic data.

5.2. Amplitude-versus-angle analysis

Now, forward seismic modeling resulted in two synthetics, one section considering elastic isotropy and another considering elastic anisotropy. Our goal is to compare the modeling results by AVO/AVA analysis. AVO/AVA is the variation of reflection amplitude with respect to the offset or angle (Simms & Bacon 2014). Using the evolution of reflection coefficient as a function of offset or angle, the geophysicists are able to identify the rock's features like fluid content, porosity, fluid indicators, and so on (Schlumberger n.d). Several authors have proved that by approximating the Zoeppritz equation, it is possible to determine the major influencing factors to the reflection coefficients (Bortfield 1961, Aki & Richards 1980, Shuey 1985, Smith & Gidlow 1987, Duffaut et al. 2000). They have identified that the major parameters that impact the resulting reflection coefficient are the acoustic impedance and V_p/V_s ratio (Bortfield 1961, Aki & Richards 1980, Mavko et al. 2009, Duffaut & Holt, 2021) (See Appendix D). Based on the contrasts resulted from the reflection coefficients by Zoeppritz equations (or contrasts from acoustic impedance and V_p/V_s ratio), the four classes of AVO/AVA response have been defined. They are presented in Figure 31. The visual representation of how to interpret AVO response is in Figure 32. Identifying the true AVO class is important in order to assess the fluid types, their relative compressibility, reservoir mineralogy, porosity, non-reservoir properties and so on.

Comparing these AVO/AVA graphs and associated AVO classes in isotropic and anisotropic synthetic seismic data makes it possible to see to what degree anisotropy affects the AVO interpretation result.

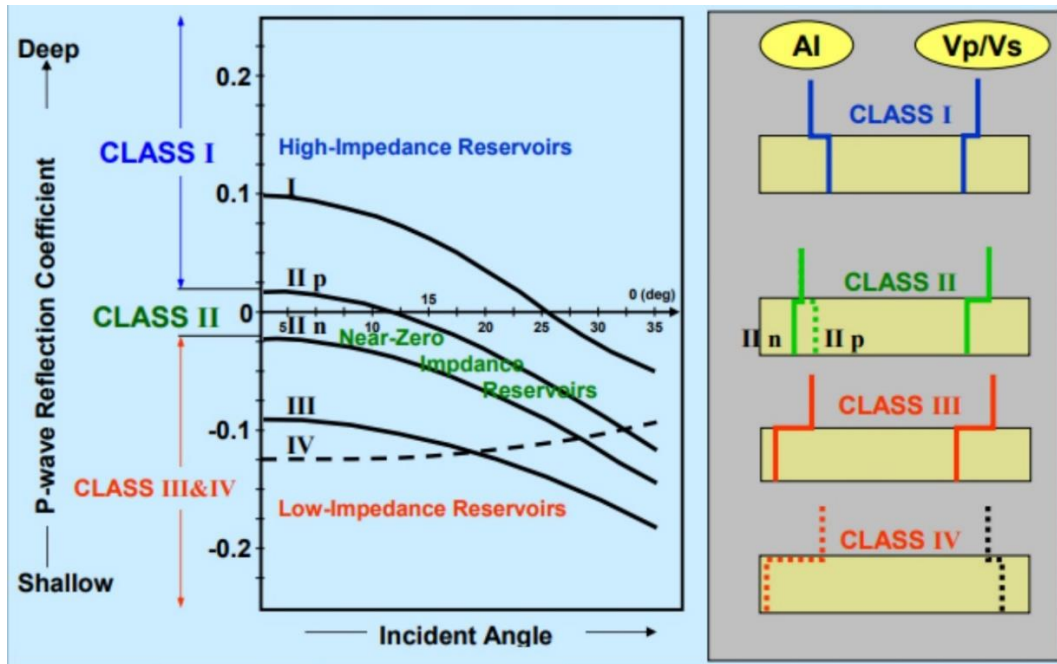


Figure 31. AVO analysis: Dependence of P-wave reflection coefficient on angle at 4 AVO classes (Rutherford & Williams 1989, Ross & Kinman 1995) (figure courtesy Duffaut & Holt, 2021).

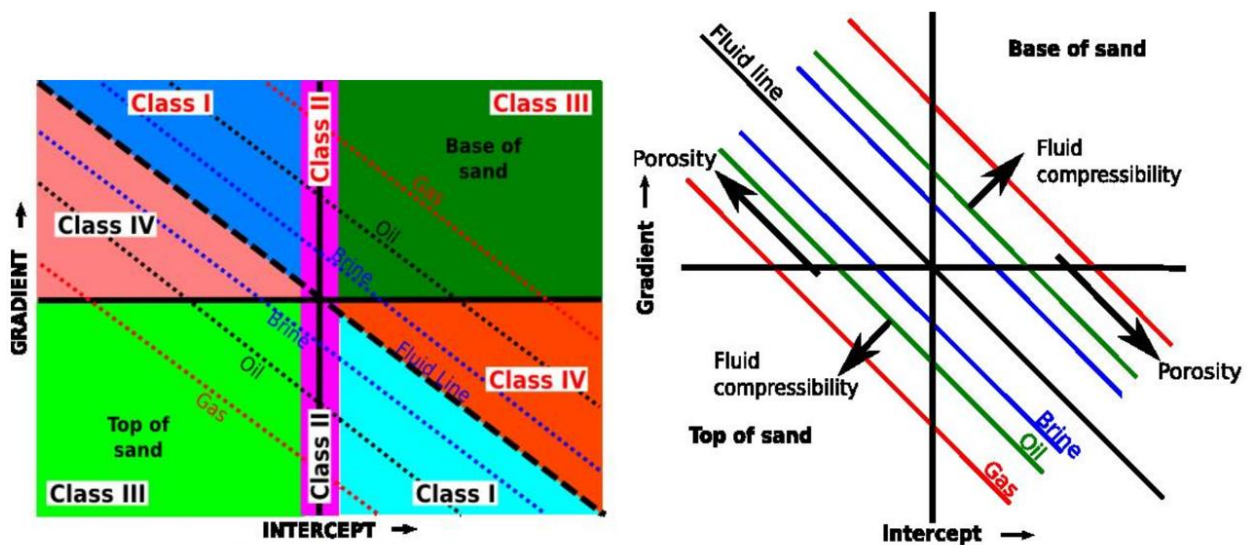


Figure 32. AVO classification: Intercept – Gradient crossplot Rutherford & Williams 1989 and Castagna & Swan 1997

5.3. Modelling and analysis results

In the previous chapter, where the validation is performed using three adjacent wells, the prediction model resulted in the anisotropic information. Since now, our aim is to prove the effect

of elastic anisotropy using AVO/AVA analysis, the same wells with predicted anisotropic logs can be used for this purpose.

Figure 33 shows the comparison panel between isotropic and anisotropic synthetics for well 7220/8-1 generated in Geoview. The panel displays the basic well log readings along with the anisotropy predictions using our model in well 7220/8-1. Additional to the well logs, V_p/V_s and Z_p (acoustic impedance) have been computed to better assess the intervals. The reservoir zone is marked by gray, and the well tops are presented. The isotropic synthetic seismic data has been generated using the conventional formation density and velocity logs. In addition to these measurements, the predicted ϵ and δ have been used for acquiring anisotropic synthetics. The angle range of anisotropic synthetic data has been reduced to 12° to 30° for better visualization of the anisotropic effect.

In a general look, the anisotropic effect is already seen from the seismic view. We can clearly see that the anisotropic synthetics differ significantly from the isotropic section in mid to far angles. Especially in the reservoir, this effect is more critical. An example of the effect can be observed at the top of the reservoir (in far angles, the reflection amplitude is inverting to positive values). In order to practically prove this effect, AVO/AVA analysis has been made. In this respect, we have picked several horizons in both synthetic data. As the forward seismic modelling in this well is

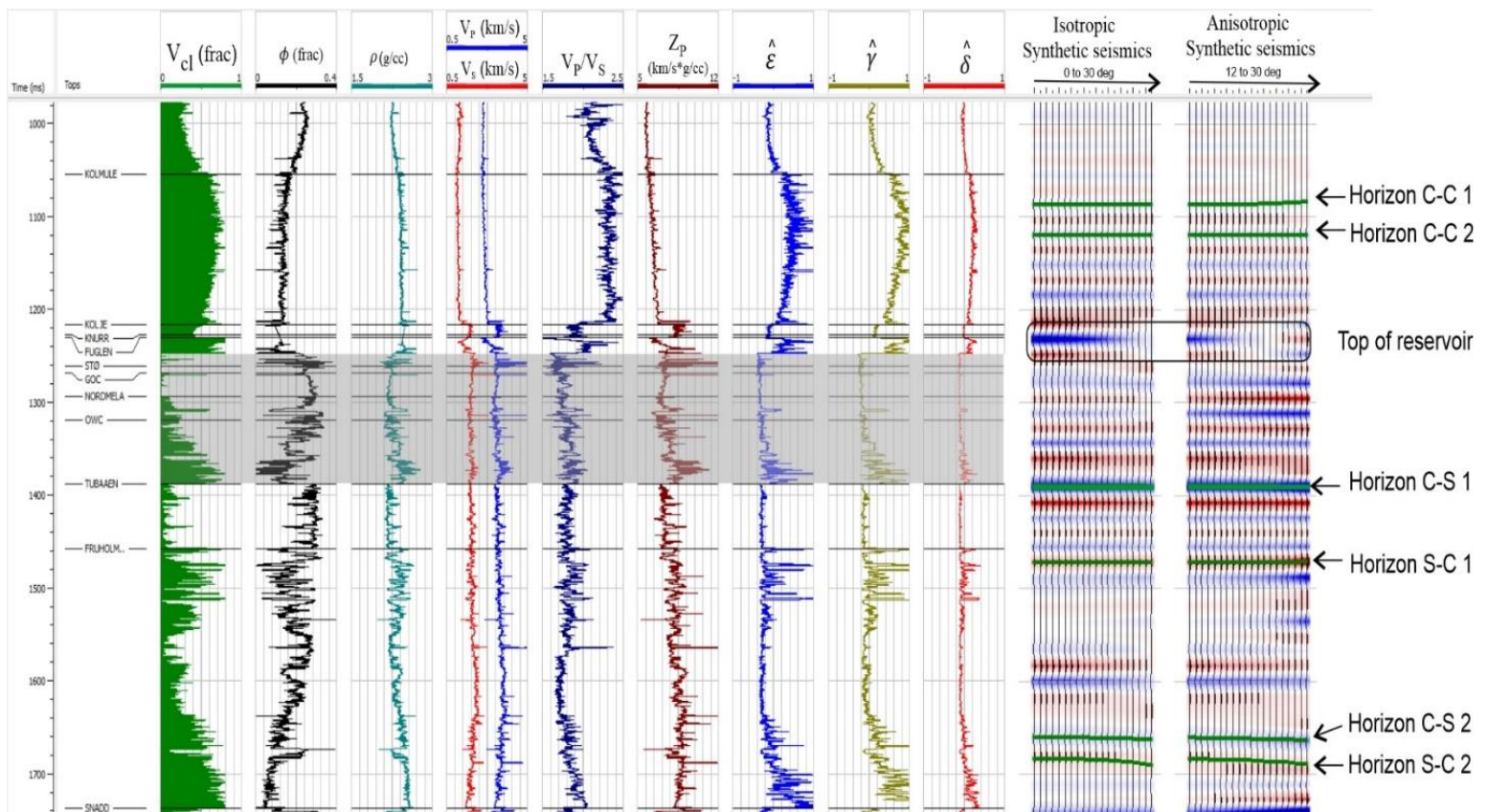


Figure 33. A comparison panel between isotropic and anisotropic synthetic seismic data in well 7220/8-1.

performed to validate the effect, it is better to pick two horizons of the same nature. Additionally, this effect is more pronounced in the lithological boundaries, so, we expect to see a significant effect in sand-to-shale or shale-to-sand packs, but less effect in sand-to-sand or shale-to-shale packs. Accordingly, the representative horizons have been picked based on the clay content log, the V_P/V_S , and acoustic impedance behaviors (Z_P) (See Figure 34). Horizon C-S 1 (clay-to-sand) picked in the top of Tubåen formation is a clear lithological boundary between shale and sand. Horizon S-C 1 (sand-to-clay) has been picked at the top of the Fruholmen formation where there is a distinct change from sand to shale. Towards the bottom of the Fruholmen formation, the formation becomes clayey, so the second set of similar horizons can be picked here (Horizon C-S 2 and Horizon S-C 2). Horizons for clay-to-clay comparison have been picked within the overlying shale in the Kolmule formation (Horizon C-C 1, Horizon C-C 2). AVA comparison results are in Figure 35.

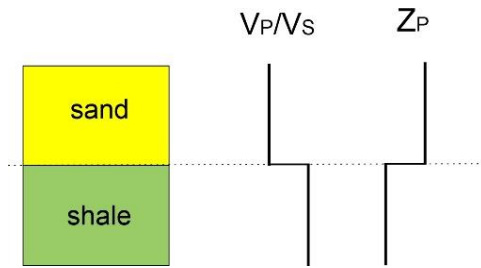


Figure 34. Behavior of the V_P/V_S and Z_P in sand-shale pack

In clay-sand horizons (Horizon C-S 1, Horizon C-S 2), the reflection amplitude versus angles in the isotropic case indicates a Class 4 AVA response. Yet, performing anisotropic AVA analysis results in a Class 3 AVA response for the same horizons. These responses are clearer in Horizon C-S 1. In a quick AVA interpretation, Class 3 AVA response indicates the top of sand interval, while Class 4 represents low-impedance reservoirs. Figure 33 clearly points out that horizon C-S 1 is the boundary between shale and sand intervals, and it is also the top of the Tubåen formation. Thus, relying on anisotropic AVA interpretation, it is possible to identify this horizon as a top of the sand interval. However, this conclusion cannot be drawn using isotropic synthetics. This is solid proof of how effective it is to include the elastic anisotropy hypothesis in the model. The anisotropic effect in Horizon C-S 2 is not as crucial as in Horizon C-S 1, but it is still possible to see the same behavior in reflectivity. As expected, sand-to-clay horizons (Horizon S-C 1, Horizon S-C 2) demonstrate the opposite effect. The anisotropic and isotropic sections conclude that both horizons indicate Class 1 AVA response. Yet, the elastic anisotropy still significantly impacts reflectivity, so the reflectivity is shifting up. Additionally, Figure 35 shows that in both clay-to-sand and sand-to-clay intervals, the elastic anisotropy starts to affect the section even at near angles (5° - 10°). The only exception is the first picked sand-to-clay horizon (Horizon S-C 1), where the anisotropy starts to affect from mid to far angles. Nevertheless, the far angles are hugely affected by anisotropy in this horizon. It was expected to see almost no reflectivity difference in clay-to-clay intervals (Horizon C-C 1, Horizon C-C 2). The analysis indicates that these sections have Class 2n AVA response.

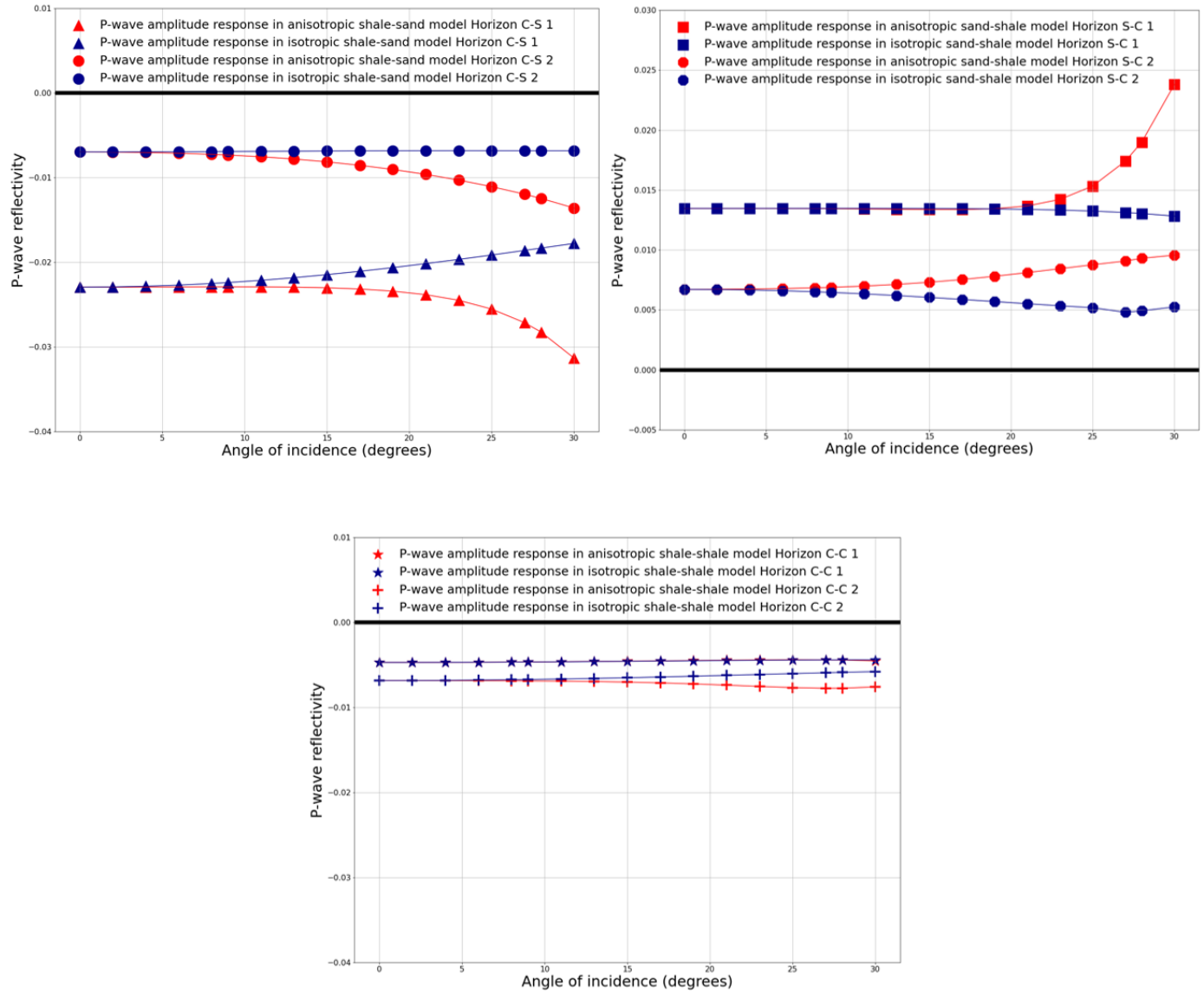


Figure 35. AVA responses of well 7220/8-1: top left – response from clay-to-sand boundaries, top right – response from sand-to-clay boundaries, bottom – response from clay-to-clay boundaries.

The same type of analysis has been made for the well 7220/7-1. Because the modeling of well 7220/8-1 has proved the anisotropic effect, further modeling is done to see the anisotropic behavior in other wells. Figure 24 has already shown the predictability of our model in well 7220/7-1. Since the prediction of elastic anisotropy in well 7220/8-1 was also successful, it is expected to have a similar anisotropic AVO/AVA behavior in this well. Forward seismic modeling results for well 7220/7-1 are in Figure 36. The structure of the panel is the same as well, 7220/8-1. It displays the conventional well logs together with our predictions and generated synthetic seismic data. The reservoir zone is marked by gray, and the well tops are presented. Both synthetics have been generated in the same way. Using density and velocity information, the isotropic synthetics have been produced. Then, anisotropic synthetics have resulted by using the predicted ϵ and δ in

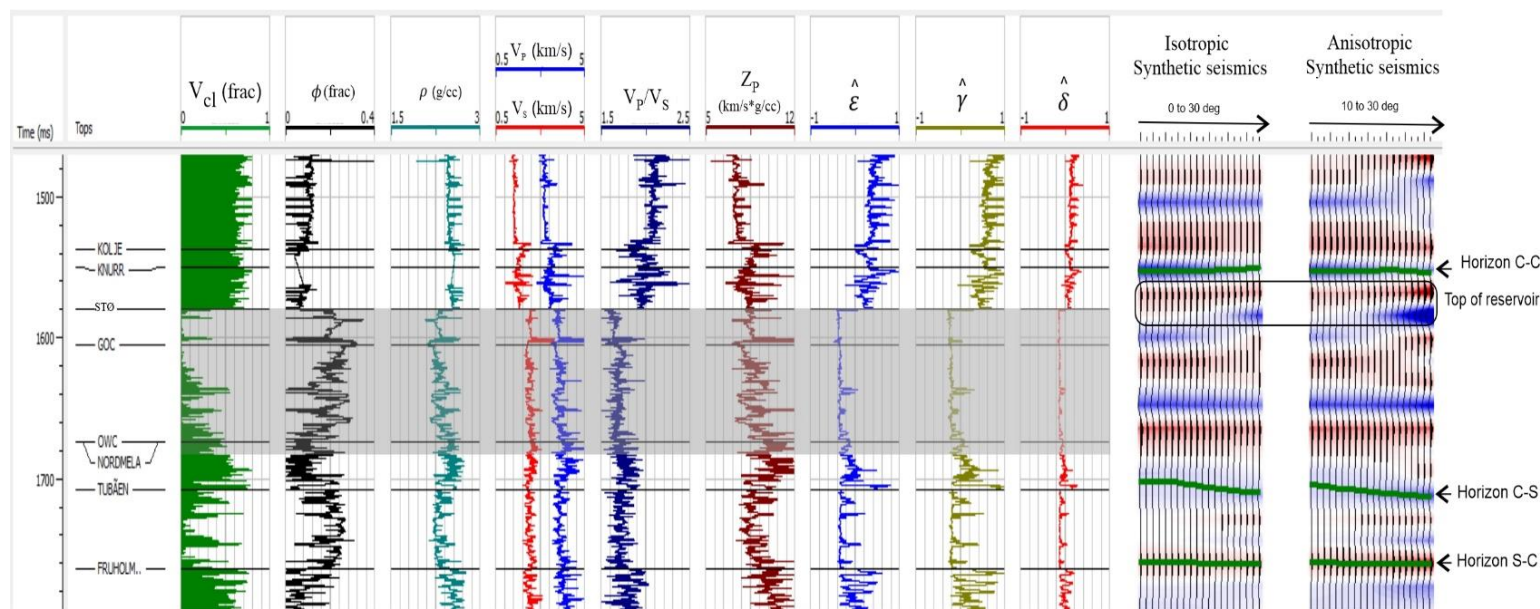


Figure 36. A comparison panel between isotropic and anisotropic synthetic seismic data in well 7220/7-1.

addition to the conventional measurements. The angle range for anisotropic synthetic data has been reduced to 10° to 30° for better visualization of the anisotropic effect. The impact of anisotropy in synthetics at mid-to-far angles is still evident. When comparing with the forward seismic modeling done in well 7220/8-1, the anisotropic effect in the top of the reservoir is negatively stronger. Horizon picking has been performed to display this effect. Again, since we are after the lithological boundaries, the clay content, V_p/V_s and Z_p logs are the base measurements. Because the anisotropic behavior is already proved by well 7220/8-1, only one horizon for each pack (shale-sand, sand-shale, shale-shale) is picked to verify this behavior. One horizon representing clay-to-clay interaction has been chosen in the overburden Kolje shale (Horizon C-C). Like well 7220/8-1, the clay-to-sand horizon (Horizon C-S) has been picked at the top of the Tubåen formation because of the reliable shale-sand boundary and the sand-to-clay horizon is again from the top of the Fruholmen formation. Figure 37 illustrates the AVA comparison plots.

The reflection amplitude versus angle analysis has indicated that in isotropic and anisotropy cases, the AVA response of the clay-to-sand horizon (Horizon C-S) follows the trend in well 7220/8-1. The amplitude has negatively increased by including elastic anisotropy. Because in well 7220/8-1, this boundary is weaker than the associated horizon in well 7220/8-1, the change in AVO/AVA classification has not been observed, so the analysis in both synthetics has resulted in Class 3 AVO/AVA classification. Additionally, AVA response in well 7220/8-1 has started to affect at the near angles. But because of the same reason, the anisotropy effect is recognizable from mid angles. In the sand-to-clay horizon (Horizon S-C), AVA interpretation has shown that the elastic anisotropy has a positive impact, so the reflection trend has been lifted up, and the AVA response is associated with Class 1. The anisotropic effect in the clay-to-clay interval (Horizon C-C) is almost indistinguishable.

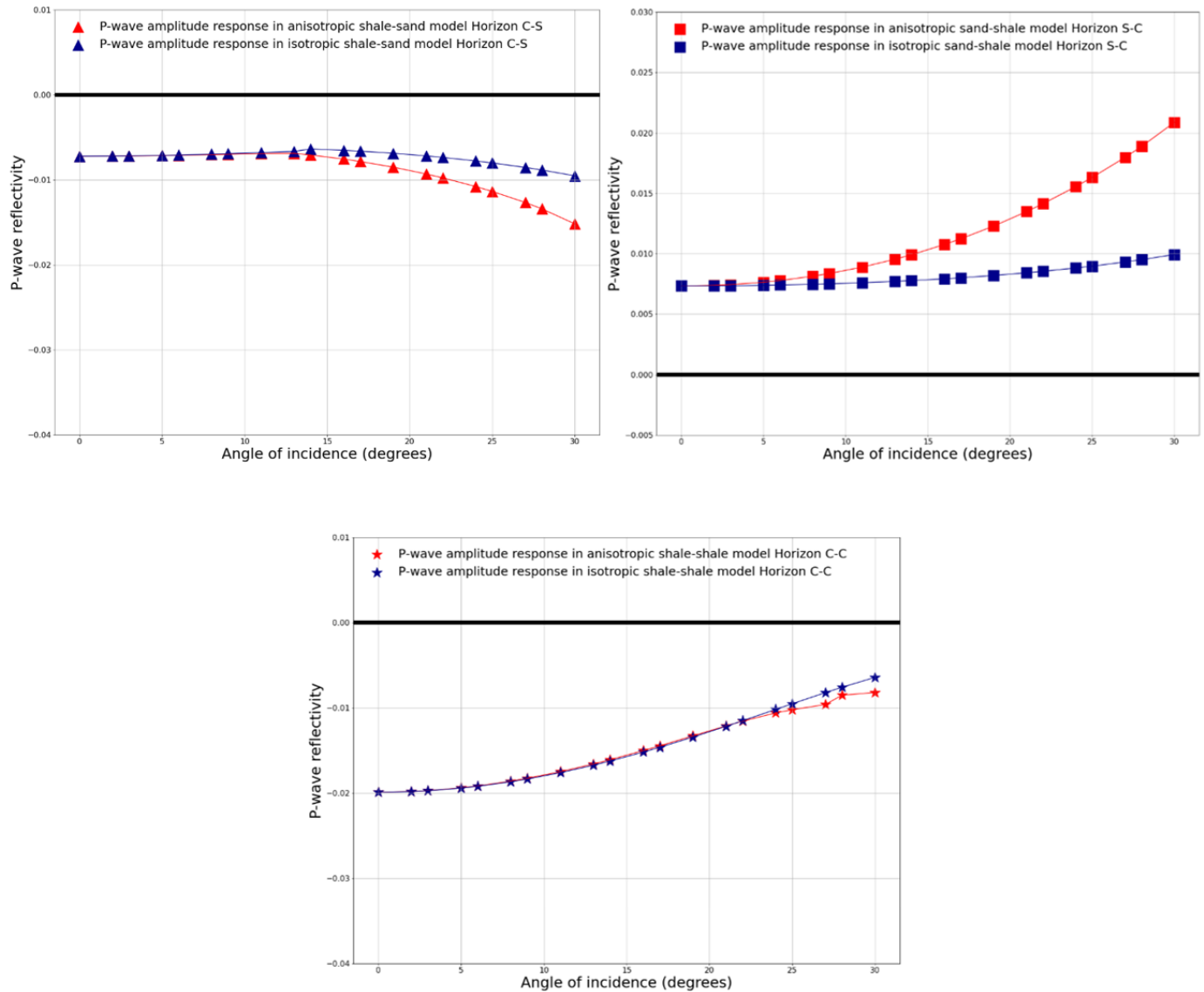


Figure 37. AVA responses of well 7220/7-1: top left – response from clay-to-sand boundaries, top right – response from sand-to-clay boundaries, bottom – response from clay-to-clay boundaries.

Among the three wells, the best prediction results have obtained in well 7220/10-1 (See Figure 28). Hence, the forward seismic modeling on this well would produce as close synthetics as possible to the real data. If we successfully verify the anisotropic effect presented in well 7220/8-1 and well 7220/7-1 by the analysis in well 7220/10-1, it will strengthen the confidence in predictions in the other two wells. Figure 38 represents the forward seismic modeling performed in well 7220/10-1. It presents the conventional well logs together with well tops and our predictions. In this well, two reservoirs have been found, and both reservoirs are marked by gray. Forward seismic modeling has run to generate the isotropic and anisotropic synthetics by the same procedure before. In a quick look, comparing isotropic and anisotropic synthetics still proves the

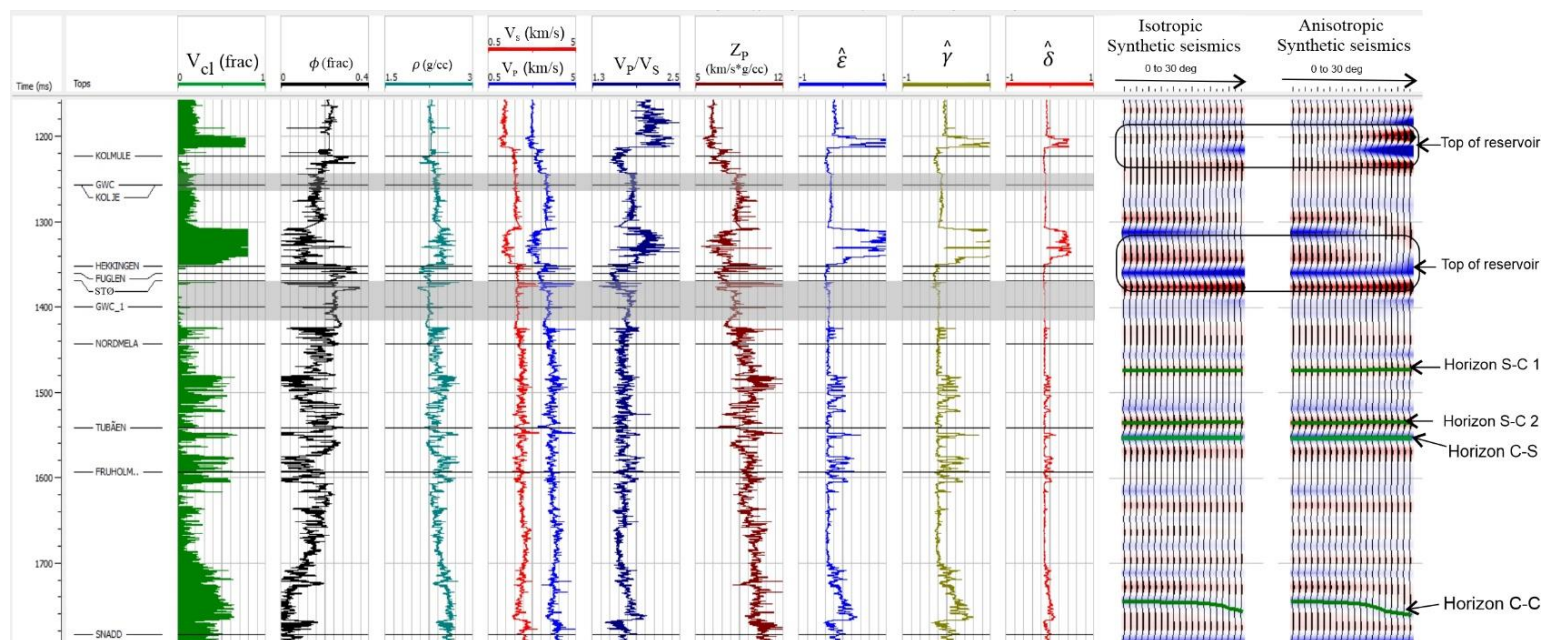


Figure 38. A comparison panel between isotropic and anisotropic synthetic seismic data in well 7220/10-1.

impact of anisotropy at far angles. In other wells, the angle range in the anisotropic section had been changed for better visualization, and near angles have been removed, however, here, the effect is significantly apparent even with the near angles in the seismic view. The anisotropic effect in both tops has shown a negatively stronger effect in far angles. Like the other two wells, horizons are picked at the lithological boundaries by the clay content, V_p/V_s and Z_p logs are the base measurements. To see the AVA response in clay-to-clay interaction, a horizon (Horizon C-C) has been picked at the bottom of Fruholmen formation, where it gets clayey. Like other wells, a reliable shale-sand boundary – the top of the Tubåen formation has been chosen for the clay-to-sand horizon (Horizon C-S). Because the well is rich with sand, it would be interesting to see the AVA response in different sand formations. Thus, for sand-to-clay formation, two horizons have been chosen: one with weaker amplitude (Horizon C-S 2) and one with higher amplitude (Horizon S-C 2). The AVA responses of these horizons are presented in Figure 39.

The reflection amplitude versus angle analysis has revealed interesting results. In Horizon C-S, the comparison of AVA responses follows the same trend as in other wells. The elastic anisotropy has negatively boosted the amplitude. However, in well 7220/7-1, we could not see the classification difference like in well 7220/8-1. Yet, with well 7220/10-1, this AVA classification difference can be observed. When considering isotropic synthetics, the AVA class resulted in Horizon C-S is Class 4, which indicates a low-impedance zone. Nevertheless, when elastic anisotropy is introduced, the classification shifts to Class 3. Although the Class 3 response is not as dramatic as in well 7220/8-1, it is still visible from the AVA plot. The sand-to-clay horizons have yielded two different results. In both horizons, elastic anisotropy has impacted as expected. It has a positive effect and pulls the reflection amplitude up. From Figure 39 (top left), one can see AVA response from the Horizon S-C 1 in both synthetics correlates with the other two wells. However, Horizon

S-C 2 has demonstrated the opposite effect. The anisotropy is still affecting positively, but in both synthetics, the reflection amplitude is weakened in far angles. The main reason for this behavior is the lithological response of this horizon. When the lithologies of Horizon S-C 1 and Horizon S-C 2 are compared, one can see that the Horizon S-C 1 is a much clearer boundary between sand and more clayey rock. On the other hand, the Horizon S-C 2 is a boundary between sand and less clayey rock. The conclusion is that the discrepancies resulting in sand-to-clay horizons are due to the clay content of the associated rocks at these horizons. Generally, in both clay-to-sand and sand-to-clay horizons, the elastic anisotropy is starting to significantly impact after near angles. The amplitude comparison between anisotropic and isotropic AVA responses in clay-to-clay interval still results in small differences.

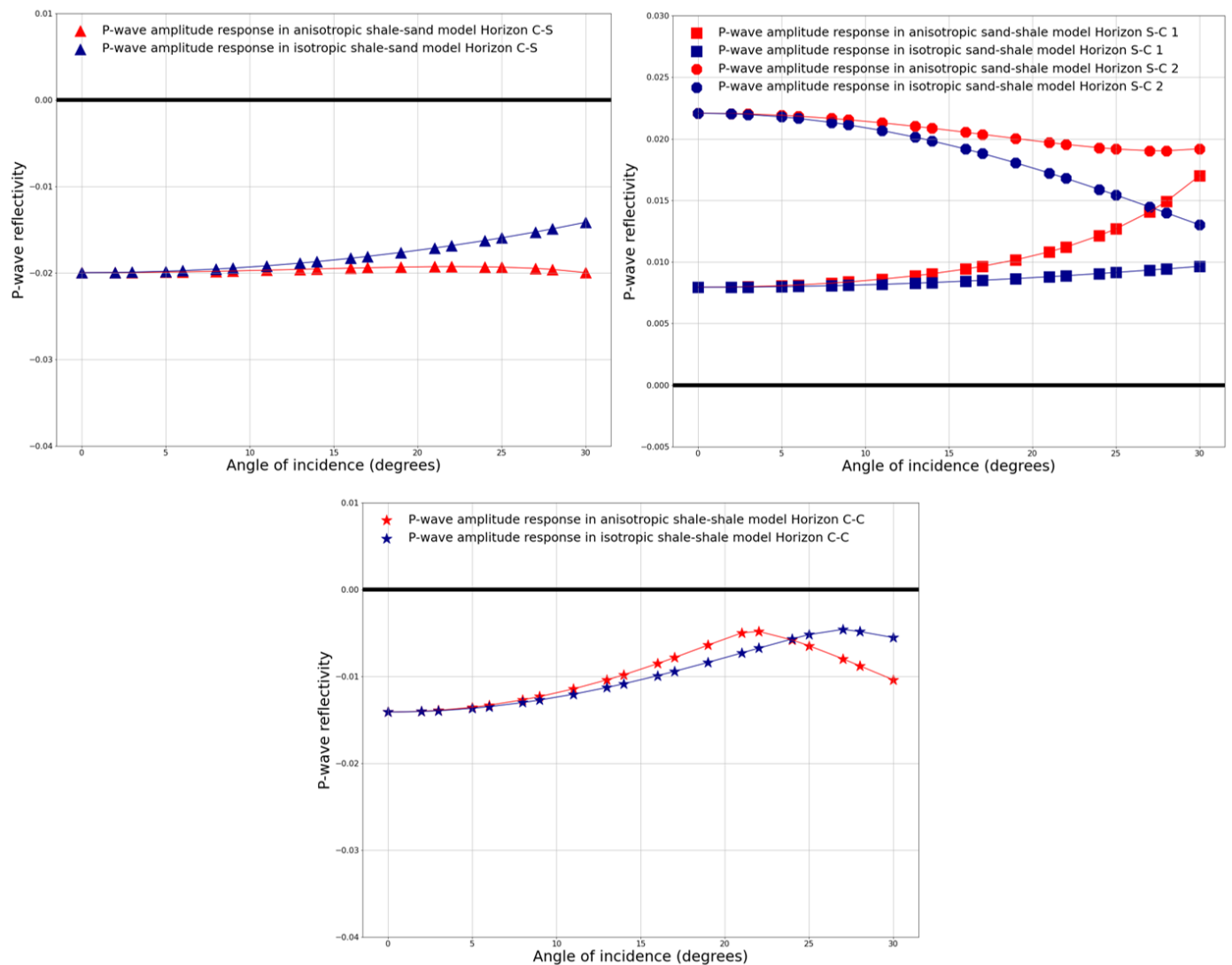


Figure 39. AVA responses of well 7220/10-1: top left – response from clay-to-sand boundaries, top right – response from sand-to-clay boundaries, bottom – response from clay-to-clay boundaries.

Chapter 6. Discussion

Now, we have defined our anisotropy prediction model and validated it using three adjacent wells from the Barents Sea. In all three wells, using readings from a Sonic Scanner logging tool, a borehole-measured Thomsen parameter γ has been acquired which is used as a reference measurement for validation. It is important to remember that the generation of γ is based on Norris 1990. Thus, although this γ is used as a reference, the uncertainty introduced by method should be noted. The references for ε and δ are measured by Walk-Away Vertical Seismic Profiling where it is available. Because all the sections after overburden are considered isotropic, the relevant anisotropic information has not been reported as zero. The verification has shown us that the tie between predicted and measured parameters is outstanding, especially in shaly reservoirs. Although the model has been designed for water-wet rocks, some mismatches are observed in the reservoir section of the well. However, the more pronounced discrepancies are those in the overburden thick shales. Such big differences in the shale pack are observed in all three wells. As discussed before, the reason for these discrepancies can be related to logging and model building problems. In the latter one, the source of these mismatches could be either clay content or K_0 calculation. The practical tests have shown that the impact of clay content on the final result is much more significant than K_0 . For instance, even from prediction, one can see that the prediction result mimics the clay content fluctuations. So, are we using a correct clay content that considers every factor to represent the lithology? Is it really a good indicator for intrinsic anisotropy? In all three wells, the clay content has been computed using La Vigne et al. 1994's empirical equation, which is based on neutron porosity and formation density-derived density porosity. If calculating a true clay content is really one of the core parts of our prediction model, it is crucial to understand what La Vigne et al. 1994's empirical method "really" calculates. It uses the neutron porosity and formation density readings from logging tools in the wellbore. In most cases, the logging tool measures as precise as possible formation density. Since it is a characterizing feature of the rock, it would contribute to the final intrinsic anisotropy. However, the response from the neutron porosity tool is not as straightforward as density. What the neutron porosity tool measures is actually the hydrogen content of the rock (Schlumberger n.d). Because hydrogen is mainly found in pore fluid, the resulting neutron measurement is classified as porosity. Yet, this porosity is not just effective porosity, and the tool is also sensitive to irreducible bound water, which has no contribution to elastic anisotropy. Additionally, the neutron-density porosity method requires a neutron porosity value for most clayey sections. According to Ellis & Singer 2008, it highly depends on which clay type is present in the interval. As reported in Table 21.3 in Ellis & Singer 2008, this value can be as high as 60 p.u in the case of montmorillonite and as low as 37 p.u in the case of kaolinite^{***}. Because the mineralogical logs are not common in conventional logging, this adds additional uncertainty to the method. Although La Vigne et al. 1994's method performs relatively well in most sections, the method-related uncertainties should be considered before using it.

^{***} In implementation, 47 p.u as an average value has been used.

As mentioned before, the best calculation of clay content is from either elemental spectroscopy or spectral gamma ray logs. Since these tools have become popular lately in conventional suites, and usually, they are not acquired for whole logging interval, the clay content estimation has been performed using the empirical methods like La Vigne et al. 1994. However, in well 7220/7-1, elemental spectroscopy has been reliably acquired. Thus, in order to assess to what degree the spectroscopy improves the prediction, a case study has been done using well 7220/7-1.

The available spectroscopy measurement in well 7220/7-1 is from elemental capture spectroscopy (ECS) sonde introduced by Schlumberger in 2006. The main principle of the tool is to measure the gamma spectra and extract the information by processing a number of gamma rays observed by the tool's detector (Schlumberger, 2006). The tool yields accurately defined lithological weight fractions of clay content along with a complete description of mineralogy and rock matrix properties, which help better estimate the porosity, fluid saturation, permeability, and so on (Schlumberger, 2006). The total clay computation is obtained using silicon, calcium, and iron concentrations (Schlumberger, 2006). Although the main element in most clays is aluminum, the estimation using secondary elements also gives precise results (Schlumberger, 2006). On the other hand, the matrix density is derived using the same elements plus sulfur concentration. As discussed above, the tool's clay content estimation is in weight fractions (W_{cl}). Yet, since our prediction is based on the volumetric rock volume presented in Figure 12 and the intrinsic anisotropy is addressed by the volume percent of clay (V_{cl}), the resulting measurement has to be converted to volumetric clay content. Ellis & Singer 2008 has suggested that this conversion can be performed using the associated density and porosity readings (Equation 6.1)

$$V_{cl} = W_{cl} \frac{\rho_{mat}}{\rho_{clay}} (1 - \phi)$$

Equation 6. 1

where ρ_{mat} and ρ_{clay} are the matrix and clay densities, respectively. The clay density has been fixed to an average value of 2.71 g/cc. Since the matrix density is available from elemental capture spectroscopy (ECS) log, there is no need for a constant value. ϕ is the porosity, and is often addressed by the density porosity. Thus, theoretically, the most precise method for estimating clay content is the ECS log, since it is a direct wellbore measurement. Additionally, it directly gives reliable values independent of the associated clay types in the section.

In order to see how this new method of computing clay content affects our prediction, the ECS log has been used to predict the elastic anisotropy in well 7220/7-1. The comparison of prediction results is presented in Figure 40. It is evident from Figure 40 that correcting the clay content estimation by ECS log has improved our final anisotropic prediction. Especially in the upper section of the well, the previous γ prediction with neutron-density porosity has estimated considerably high values than reference γ by Sonic Scanner. Yet now, the ECS log has minimized the mismatch and the resulting γ has almost covered the reference log. In the reservoir and low

clayey zones, the difference is hardly seen because here, the impact of intrinsic anisotropy is too low ($1 - V_{cl}$ is high). The previous prediction has resulted in a big discrepancy in the overburden shale interval. Although the prediction has been improved by the ECS log, the discrepancy between Sonic Scanner γ and predicted γ is still present. As discussed before, in this interval, the logging tool has encountered some difficulties indicated by the caliper log. Considering the ECS log reflects wellbore-measured clay content, the elastic anisotropy in this section should be quite high. Thus, the Sonic Scanner measurements in this interval do not appear to be reliable. Additionally, because another important quantity in our prediction model is the horizontal-to-vertical stress ratio, K_0 , the prediction can further be improved by a full control on the stress regimes in the well using laboratory tests or relevant borehole data. However, because the logging condition is not stabilized and the prediction follows the general trend indicated by clay content, it would be wise to accept that the result of γ prediction is as reasonable as possible. Thus, we have proved the value of clay content computation for our prediction scheme, so that by introducing ECS log into elastic anisotropy prediction in well 7220/7-1 and precisely correcting the clay content calculation, γ prediction results have almost reached a perfect correlation with Sonic Scanner reference measurements except in the overburden shale section. Owing to this conclusion, the prediction yielded in ε and δ has also been accepted as equally realistic. The full elastic anisotropy prediction using the elemental capture spectroscopy (ECS) log is presented in Figure 41. The uncertainty of the prediction has also been computed by the same fashion before. Overall results are in-line with the general lithology trend in clay content. Yet, it is also worth noting that the Sonic Scanner in the overburden section is not reliable, and the improvement of the ECS log is relatively small. So, it is still not a bad idea to use La Vigne et al. 1994's method where elemental concentration logs are unavailable.

Although we have improved the prediction results in well 7220/7-1, the relevant AVO/AVA analysis and synthetic seismic data generation have not been done. The reason is that despite the ECS log having improved the prediction, the general trend has not been changed because of the magnitude of improvement. Since AVO/AVA analysis is more pronounced in the boundaries, the influence of elastic anisotropy on reflection amplitude would have the same trend.

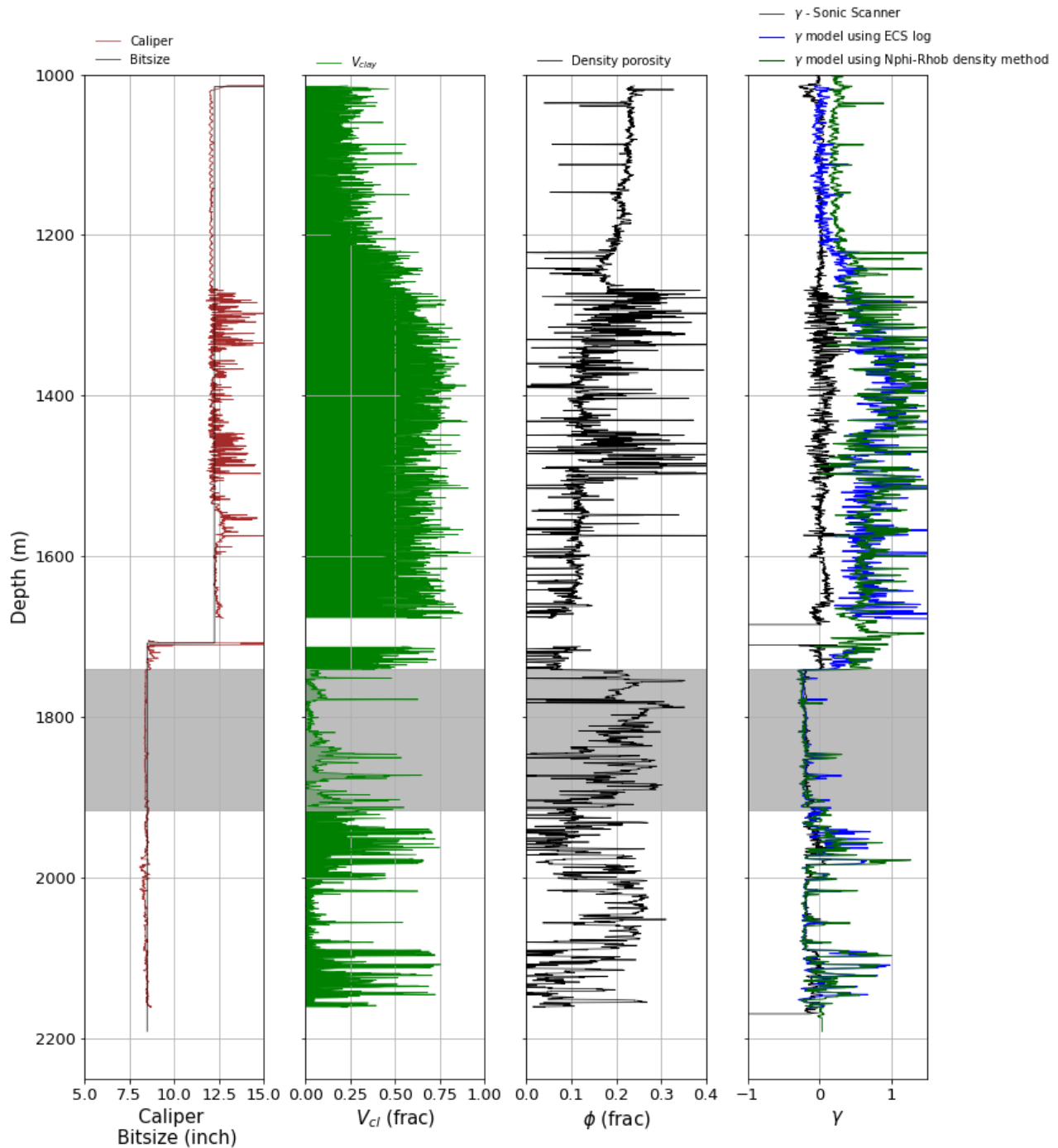


Figure 40. Comparison of prediction results for well 7220/7-1. From left to right: Caliper (brown) & Bit size (black), Clay content computed by ECS log (green), Density porosity (black), γ . Hydrocarbon zones are highlighted by gray.

γ track (4th track): Black – formation γ generated by Stoneley wave, Blue – predicted γ by our model using ECS log. Green - predicted γ by our model using La Vigne et al. 1994's neutron-density porosity method

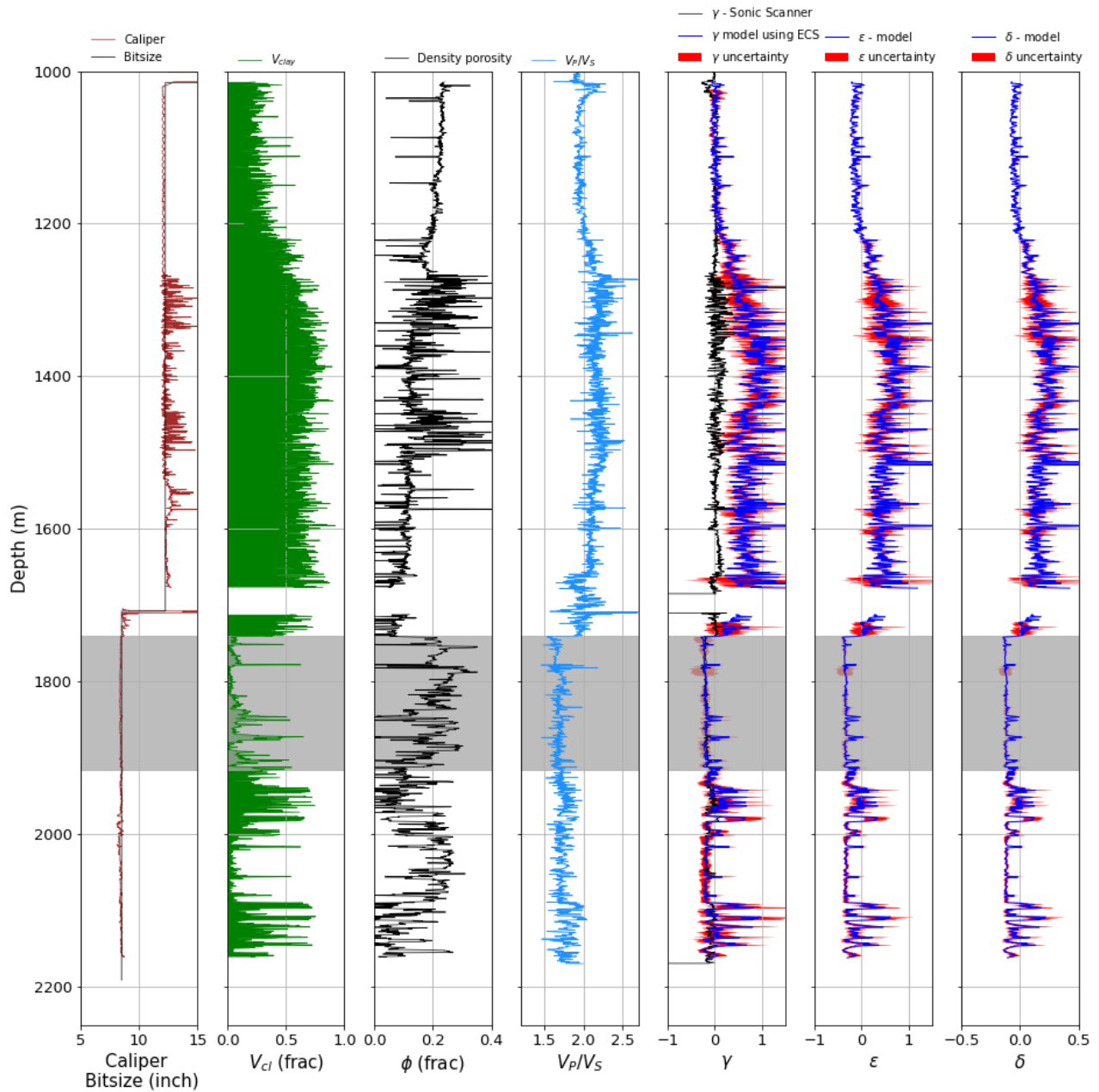


Figure 41. Prediction results of well 7220/7-1. From left to right: Caliper (brown) & Bit size (black), Clay content by ECS log (green), Density porosity (black), V_p/V_s ratio (light blue), γ , ϵ , δ . Hydrocarbon zones are highlighted by gray.

γ track (5th track): Black – formation γ generated by Stoneley wave, Blue – predicted γ by our prediction model using ECS log. Red – uncertainty of prediction.

ϵ track (6th track): Blue – predicted ϵ by our prediction model using ECS log. Red – uncertainty of prediction.

δ track (7th track): Blue – predicted δ by our prediction model using ECS log. Red – uncertainty of prediction.

A quick note on further works

In the further works, I recommend discussing the stress sensitivity. When correction stress contribution in the proposed model in Chapter 2 using $\frac{\sigma'_h}{\sigma'_v}$, we have assumed that the relationship between stress and stiffness is linear ($C_{ij} \sim \sigma$). This linear relationship stems from the classical Hooke's law (Hooke 1678) which states a linear relationship between stress and strain. In order to test the stress-strain relationships, Hertz 1882 and Mindlin 1949 have performed two tests, a normal compression (Hertz 1882) and tangential compression (Mindlin 1949) of two circular bodies that have simple cubic packing of identical spherical grains. A schematic view of the tests is in Figure 42.

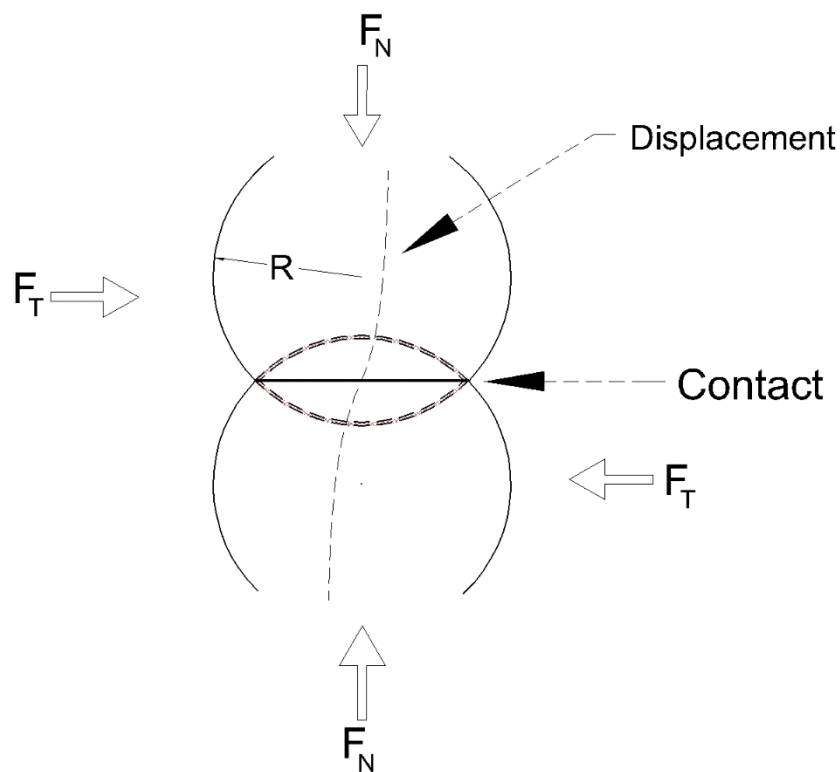


Figure 42. A schematic view of two spheres with a radius R . A deformation has been seen at their contact subjected by contact forces and displacement during compression tests done by Hertz 1882 (normal compression, F_N) and Mindlin 1949 (tangential compression, F_T).

The theory has claimed that because of the stress concentration of the contacts of two bodies, the linearity of stress-strain is no longer valid in the case of macroscopic stress. This has led to consider the non-linearity in stress-stiffness relations ($C \sim \sigma^n$). The implementation of Hertz-Mindlin contact theory have resulted that this dependency is constant and $n = \frac{1}{3}$ in elastic, homogenous, isotropic medium with simple cubic packed grains (Equation 6.2) (Hertz 1882, Mindlin 1949, Walton 1987, Duffaut et al. 2010). Later on, the laboratory measurements done by

Walton 1987, Brandt 1955, Dvorkin & Nur 1996 have developed the theory further, yet the bottom line was still the non-linearity of stress-strain relations.

$$K_{dry} = \left(\frac{C_p^2 (1 - \phi)^2 G_s^2 \sigma}{18\pi^2 (1 - \nu_s)^2} \right)^{\frac{1}{3}}$$

Equation 6. 2

Although the non-linearity was proved, the anisotropic influence has not been examined. In this chapter I am also proposing an anisotropic correction to Hertz-Mindlin's non-linearity assumption and claiming that as medium becomes anisotropic, the stress-stiffness dependency is going to be linear. The study done by Sayers 1999 can be a proof of this theory. In his Figure 5, in shale, when anisotropic is increasing, the stress-stiffness relationship becomes more linear. Then, in order to consider the stress sensitivity in anisotropic media, the stiffness should be dependent on stress by $n = \frac{1}{3} + V_{cl}$. A quick simulation has been done to see the effect of clay content in the stress-stiffness dependency (Figure 43). Figure 43 illustrates the dependence of stiffness on stress when Hertz-Mindlin contact theory is assumed and adds the effect of clay content.

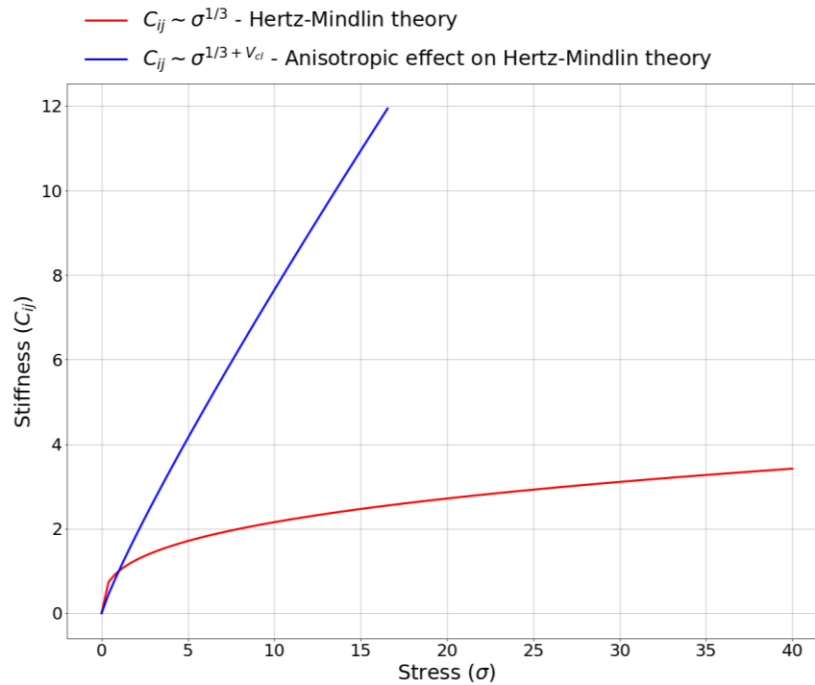


Figure 43. The effect of anisotropy on stress-stiffness relationship. In the isotropic case, Hertz-Mindlin contact theory have results 1/3 dependency (red line). The blue line is when anisotropy is added in the form of V_{cl} .

Because the other essential parameters of the proposed model are Hooke law-based, using this correction of Hertz-Mindlin, the comparison cannot be made. Yet, this can still parameters such as K_0 is acquired from other sources, the stress sensitivity can be one of the sources to improve the prediction.

Chapter 7. Conclusion

This study has proposed an elastic anisotropy prediction model while providing an extensive theoretical background of elastic anisotropy. An important distinction that differentiates the proposed model from other existing anisotropy models is that this model explains and covers all three anisotropic causes while based on practical applications such as wave propagation. The model predicts horizontal information by projecting vertical measurements. It defines intrinsic anisotropy using $(1 - V_{cl})$ instead of V_{cl} . The reason of that different clay types has different intrinsic responses. Considering $(1 - V_{cl})$ ensures us that all the influencing factors for clays have been covered. A safer way to estimate the clay content is through elemental concentration spectroscopy, which gives the direct measurement, or spectral gamma ray, which is more reliable than a natural gamma ray. However, in most cases, these logs are not available. For these occasions, the clay content can be calculated using La Vigne et al. 1994's neutron-density porosity equation. The model addresses stress-induced anisotropy using K_0 which is a horizontal-to-vertical stress ratio. This ratio is acquired using vertical velocity measurements and predefined δ . The last anisotropy cause, layer-induced anisotropy is added using Backus averages. Since the model results in horizontal measurements, the suite consists of two prediction models: ε and γ . Additionally, δ log is predicted using linear approximation resulting from regression studies of Thomsen 1986's data.

The model has been verified using three adjacent wells (well 7220/8-1, well 7220/7-1, and well 7220/10-1) in the Barents Sea. The wells have been chosen for their available Sonic Scanner data, which generated borehole-measured γ to be used as a reference. This reference is acquired using the Stoneley-wave measurement proposed by Norris 1990. The references for ε and δ have been extracted using Walk-Away Vertical Seismic Profiling. Yet, only for well 7220/8-1, the WAVSP measurements are available. Thus, for other two wells, the verification has been performed using only γ . The verification has shown that the model performs almost as perfectly as possible in shaly sand intervals. In γ comparison, it covers almost true readings from Sonic Scanner, and associated uncertainty is relatively small. Based on its predictability in γ , similar conclusions can be drawn for ε and δ . It is obvious that both ε and δ follow the same trend. Additionally, all three anisotropic information logs successfully confirm the negative anisotropy in non-clayey sections and positive anisotropy in clayey sections. This prediction method can be a point of interest to geophysicists or geoscientists because one of the core motivations for the energy industry is to characterize the reservoir to have an idea of where to look for possible hydrocarbons or for storage for carbon solutions.

The model also overpredicts the elastic anisotropy in the intervals which have relatively high clay content. The possible reasons for this overestimation can be the parameter definition in these intervals or the issues encountered during well logging. The problems related to caving or borehole fluid can be several examples that can cause this mismatch. However, in the model, the parameters that directly affect the prediction are K_0 and V_{cl} . Because the general prediction trend follows the clay content, the effect of clay content on prediction is much more critical than K_0 . In all wells,

the verification has been performed using the neutron-density porosity empirical equation, which can be the number one cause of the overestimation. Although in well 7220/7-1, the ECS log has improved the result, the mismatch in overburden shale is still present. It is also worth noting that the Sonic Scanner readings in overburden shale in well 7220/7-1 were not reliable because of borehole-related problems. Overall, the comparison with the ECS log shows that La Vigne et al. 1994's method is still a reliable method to use in shaly sand intervals. Thus, the recommendation is to use borehole-derived measurements where they are available. Yet, La Vigne et al. 1994's method is also a representative method to utilize when these measurements are not acquired. Additionally, in the overburden section, the intrinsic anisotropy indicator $(1 - V_{cl})$ is very low, and dividing a measurement into very low values will propagate high results. Thus, the overprediction can be explained by issues related to model building, model implementation, and measurement acquisition.

Since the prediction model results in elastic anisotropy in Barents Sea wells, these conclusions can be applied to see the effect of anisotropy in seismic sections. Yet, we do not have access to the real seismic done by operators in the area. Thus, the anisotropic effect has been analyzed using synthetic seismic sections. The forward seismic modeling has been run for all three wells (well 7220/8-1, well 7220/7-1, well 7220/10-1) to indicate the effect of anisotropy by comparing isotropic and anisotropic synthetic seismic sections. Because the modeling yields PP anisotropic synthetic sections, the only required anisotropic parameters are ε and δ . The AVO/AVA analysis has proved the impact of elastic anisotropy in their seismic responses. Since AVO/AVA responses are more significant in the lithological boundaries, the horizons have been picked using clay content, V_p/V_s , and Z_p logs. The AVO/AVA results for clay-to-sand horizons have shown that elastic anisotropy has a negative impact on reflection amplitude. However, this is the opposite in sand-to-clay horizons. Although depending on the clay content, the effect can increase or decrease, the AVO/AVA response in sand-to-clay horizons has demonstrated that elastic anisotropy affects the reflection amplitude positively. Thus, the reflection trend is lifted up. This analysis in clay-to-clay horizons is expected to have very a negligible difference in reflection amplitudes. As expected, it does not conclude on significant differences. Among all three types of horizons, clay-to-sand horizons have displayed a strong effect of anisotropy. Therefore, depending on the magnitude of lithological difference in clay and sand, clay-to-sand horizons have shown two different AVO/AVA classes. When considering the elastically isotropic medium, the resulting class is Class 4, yet this is changed to Class 3, assuming elastic anisotropy. This comparison demonstrates the importance of elastic anisotropy in such applications.

At last, for optimizing the proposed anisotropic prediction model, this thesis has recommended studying the stress-stiffness relationship and proposed an anisotropic correction to Hertz-Mindlin contact theory that achieves linearity as the medium becomes clayey. Because Hertz-Mindlin's contact theory violates Hooke's law and the other constituents of the proposed prediction model are dependent on Hooke's law, the verification of the model cannot be made. Yet, further studies on this topic could lead significant improvements.

Overall, we have successfully defined and validated an elastic anisotropy prediction model that considers three causes of elastic anisotropy. The benefit of this model is that it is easy to implement and cost-effective. So, this model can easily be used to enhance subsurface description, which is the core of applications such as seismic imaging, processing, and modeling 4D seismic interpretation. It is even possible to revisit the formations that has been classified as non-productive because of wrong assumption. Thus, in many ways, elastic anisotropy is the key to better understand and appreciate Earth and its evolution.

Acknowledgement

I would like to thank to Norwegian University of Science and Technology for providing relevant software and equipments for conducting this study.

I also want to take the opportunity to express my thanks to Norwegian Petroleum Directorate and Schlumberger for providing the well log data from well 7220/8-1, well 7220/7-1, well 7220/10-1, and Walk – Away Vertical Seismic Profiling data for well 7220/8-1, for validating our anisotropic prediction model.

Additionally, special thanks to GeosoftTM for their software Geoview – Hampson-Russel Suites where I have performed my forward seismic modelling.

Appendices

A. Sayers 1999: Contribution of stress into the overall anisotropy

Sayers 1999 argues the overall anisotropy can be expressed into two parts: intrinsic and excess anisotropy. This excess anisotropy is considered the stress-induced anisotropy. Sayers 1999 have defined these two parts using compliance matrices.

$$S_{ijkl} = S_{ijkl}^0 + \Delta S_{ijkl}$$

Equation A. 1

S_{ijkl} is total compliance, S_{ijkl}^0 – compliance at high stress regimes (when all contacts are closed – intrinsic), ΔS_{ijkl} – excess compliance by stress contribution. From previous works, the features about intrinsic properties (here compliances) are well-studied. Yet, the excess compliances which defines the stress-induced anisotropy is mostly unknown. According to Sayers 199, the excess compliance can be written by combination of second- and forth-rank tensor (α_{ij} and β_{ijkl})

$$\Delta S_{ijkl} = \frac{1}{4} (\delta_{ik}\alpha_{jl} + \delta_{il}\alpha_{jk} + \delta_{jk}\alpha_{il} + \delta_{jl}\alpha_{ik}) + \beta_{ijkl}$$

Equation A. 2

$$\alpha_{ij} = \frac{1}{V} \sum_r B_T^{(r)} n_i^{(r)} n_j^{(r)} A^{(r)}$$

$$\beta_{ijkl} = \frac{1}{V} \sum_r (B_N^{(r)} - B_T^{(r)}) n_i^{(r)} n_j^{(r)} n_k^{(r)} n_l^{(r)} A^{(r)}$$

Equation A. 3

where α_{ij} is second-rank tensor, β_{ijkl} is forth-rank tensor, δ_{ij} is Kronecker delta, $B_T^{(r)}$ and $B_N^{(r)}$ – shear and normal compliances at r-th contact, $n_i^{(r)}$ is i-th component of unit normal to r-th contact, $A^{(r)}$ is the area of contact plane. The summation has been done over all grain contacts

within rock volume V . Sayers 1999 also specifies that B_N characterizes the displacement discontinuity normal to the contact produced by a normal traction, on the other hand, B_T characterizes the shear displacement discontinuity produced by a shear traction at the contact, and it is independent of the direction of shear traction in the contact plane. If $B_N = B_T$ for all contacts, the excess compliance is completely dependent on the second-rank tensor. Therefore, Equation A.2 defines the excess compliances from the contacts between clay platelets in terms of second- and forth- rank tensors (α_{ij} and β_{ijkl}).

Note that second- and forth-rank tensors are symmetric with respect to all rearrangements of indices. A simple model of the medium that these expressions are valid is in Figure A. The contacts are assumed to be flat with unit normal n which is constant along each area A . Additionally, the stress interactions between contacts are neglected so that each contact region is subjected to the same average stress field σ_{ij} .

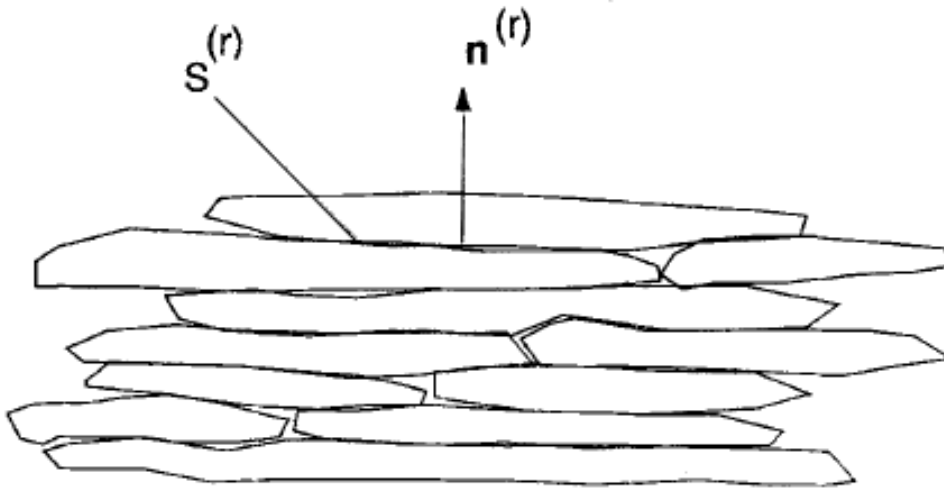


Figure A. Region with the shale, showing a local alignment of clay platelets (Sayers 1999)

Using symmetry in the case of general TI medium ($\alpha_{11} = \alpha_{22}, \beta_{1111} = \beta_{2222}, \beta_{1212} = \beta_{1122} = \beta_{1111}/3$), the expressions become:

$$\Delta S_{1111} = \Delta S_{2222} = \alpha_{11} + \beta_{1111}$$

$$\Delta S_{3333} = \alpha_{33} + \beta_{3333}$$

$$\Delta S_{1212} = \alpha_{11}/2 + \beta_{1111}/3$$

$$\Delta S_{2323} = \Delta S_{3131} = (\alpha_{11} + \alpha_{33})/4 + \beta_{1133}$$

$$\Delta S_{1122} = \beta_{1111}/3$$

$$\Delta S_{2233} = \Delta S_{3311} = \beta_{1133}$$

B. Li 2006's model and its theory

Li 2006 have developed an anisotropic prediction model for ε and γ in siliciclastic rocks which can be used to determine the anisotropic information using conventional well logs. The model assumes that the horizontal velocity is a function of the vertical velocity and clay content (so, only intrinsic anisotropy). The laboratory measurements by Johnston and Christensen 1995 showed that there exists a linear correlation between the volume of clay in the rock and a degree of alignment which indicates an intrinsic anisotropy (Li & Pickford 2002, Li 2006). Although based on Naghiyev 2021, this model performs fairly good, the model only assumes the effects of intrinsic anisotropy with ignoring anisotropy from stress effect. The proposed relations for ε and γ are in Equation B.1, and the original models are in Figure B.1.

$$\varepsilon = \frac{0.6V_{cl}(V_P - V_{Pwater})}{V_{Pquartz} - V_{Pwater} - 2.65V_{cl}}$$

$$\gamma = \frac{0.67V_{cl}V_S}{V_{Squartz} - 2.29V_{cl}}$$

Equation B. 1

The last important consideration of model is it assumes the linearity between ε and δ , so that $\delta = 0.32\varepsilon$.

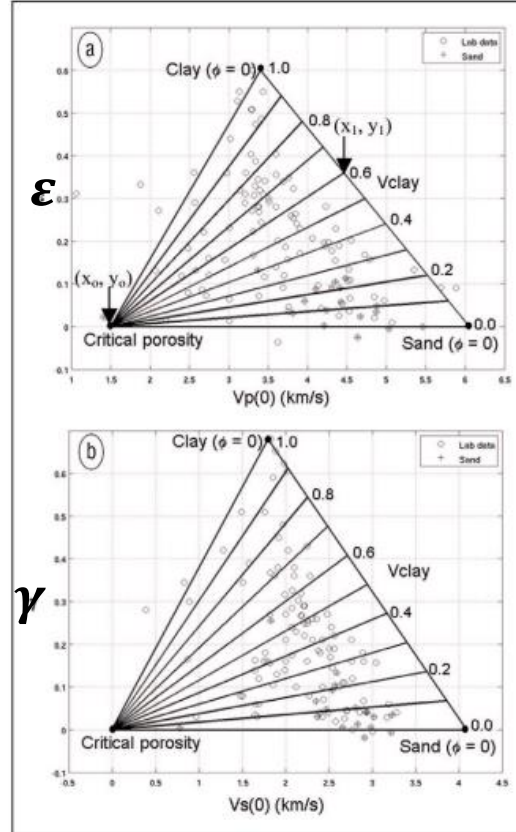


Figure B. Li 2006's elastic anisotropy prediction scheme

C. Propagation of error in proposed models

The propagation of errors, hence, uncertainty in a quantity that is a function of several parameters is computed by the uncertainties of each term (Gaussian random error σ_i) and their derivatives (Lyons 1991, Carter et al. 2020.). If we consider a variable $A = f(a_1, a_2, a_3, \dots)$, the global equation of uncertainty is in Equation C.1.

$$\sigma_A^2 \approx \sum_{i=1}^n \sum_{j=1}^k \sigma_{a_i}^2 \left(\frac{\partial A}{\partial a_i} \right)^2 + \sigma_{a_i a_j}^2 \left(\frac{\partial A}{\partial a_i} \right) \left(\frac{\partial A}{\partial a_j} \right) + \sigma_{a_j}^2 \left(\frac{\partial A}{\partial a_j} \right)^2$$

Equation C. 1

If the uncertainties of each term are not correlated, the middle term can be dropped, and the equation is reduced to Equation C.2.

$$\sigma_A^2 \approx \sum_{k=1}^n \sigma_{a_k}^2 \left(\frac{\partial A}{\partial a_k} \right)^2$$

Equation C. 2

Applying this equation to our proposed C_{11}, C_{66} expressions yields,

$$\sigma_{C_{11}}^2 = \sigma_{C_{33}}^2 \left(\frac{K_0}{1 - V_{cl}} \right)^2 + \sigma_{K_0}^2 \left(\frac{C_{33}}{1 - V_{cl}} \right)^2 + \sigma_{V_{cl}}^2 \left(\frac{C_{33}K_0}{(1 - V_{cl})^2} \right)^2$$

$$\sigma_{C_{66}}^2 = \sigma_{C_{44}}^2 \left(\frac{3K_0}{1 - V_{cl}} \right)^2 + \sigma_{K_0}^2 \left(\frac{3C_{44}}{1 - V_{cl}} \frac{1}{(1 + 2K_0)^2} \right)^2 + \sigma_{V_{cl}}^2 \left(\frac{C_{44}}{(1 - V_{cl})^2} \frac{3K_0}{1 + 2K_0} \right)^2$$

Equation C. 3

Using the definition of ε and γ proposed by Thomsen 1986, the uncertainty in estimated ε and γ is:

$$\sigma_{\varepsilon}^2 = \sigma_{C_{33}}^2 \left(-\frac{C_{11}}{2C_{33}^2} \right)^2 + \sigma_{C_{11}}^2 \left(\frac{1}{2C_{33}} \right)^2$$

$$\sigma_{\gamma}^2 = \sigma_{C_{44}}^2 \left(-\frac{C_{66}}{2C_{22}^2} \right)^2 + \sigma_{C_{66}}^2 \left(\frac{1}{2C_{44}} \right)^2$$

Equation C. 4

D. Zoeppritz equation

In non-zero incidence, the reflection and transmission coefficients are dependent on angles. An incidence in simple half-space is sketched in Figure D. According to Snell's law, the generated angles are related to each other by associated velocities (Equation D.1)

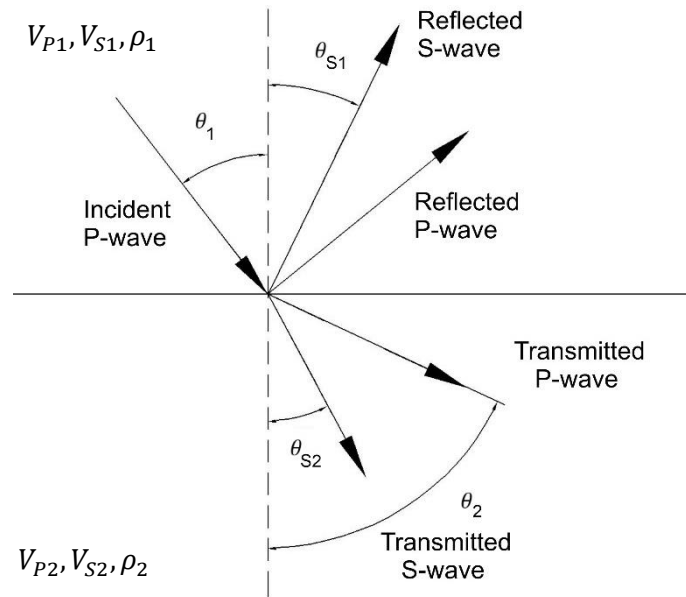


Figure D. Non-zero incidence of P-wave in half-space

$$p = \frac{\sin\theta_1}{V_{P1}} = \frac{\sin\theta_2}{V_{P2}} = \frac{\sin\theta_{S1}}{V_{PS1}} = \frac{\sin\theta_{S2}}{V_{PS2}}$$

Equation D. 1

where p is a ray parameter, θ and θ_S are the angles of P- and S-wave propagation respect to the reflector normal.

Based on the propagations of P- and S-waves, Zoeppritz 1919 has developed a set of equations that describes P- and S- wave energy partitioning into reflection and transmission energies (Zoeppritz 1919, Knott 1899, Aki & Richards 1980, Castagna 1993, Mavko et al, 2009, Duffaut & Holt, 2021). The generalization of Zoeppritz equations has been described in the matrix form by Aki & Richards 1980 (Mavko et al. 2009) (Equation D.2).

$$\begin{bmatrix} \dot{P}\dot{P} & \dot{S}\dot{P} & \dot{P}\dot{S} & \dot{S}\dot{S} \\ \dot{P}\dot{S} & \dot{S}\dot{S} & \dot{P}\dot{P} & \dot{S}\dot{P} \\ \dot{P}\dot{P} & \dot{S}\dot{P} & \dot{P}\dot{P} & \dot{S}\dot{P} \\ \dot{P}\dot{S} & \dot{S}\dot{S} & \dot{P}\dot{S} & \dot{S}\dot{S} \end{bmatrix} = A^{-1}B$$

Equation D. 2

Each matrix element describes either reflection or transmission coefficient. First letter stands for the incidence wave, and the second is for reflected or transmitted wave. The downgoing propagation is denoted with ` symbol, and upgoing propagation with ` symbol, which means `` represent a reflection coefficient, and `` indicates a transmission coefficient.

$$A = \begin{bmatrix} -\sin\theta_1 & -\cos\theta_{S1} & \sin\theta_2 & \cos\theta_{S2} \\ \cos\theta_1 & -\sin\theta_{S1} & \cos\theta_2 & -\sin\theta_{S2} \\ 2\rho_1V_{S1}\sin\theta_{S1}\cos\theta_1 & \rho_1V_{S1}(1-2\sin^2\theta_{S1}) & 2\rho_2V_{S2}\sin\theta_{S2}\cos\theta_2 & \rho_2V_{S2}(1-2\sin^2\theta_{S2}) \\ -\rho_1V_{P1}(1-2\sin^2\theta_{S1}) & \rho_1V_{S1}\sin 2\theta_{S1} & \rho_2V_{P2}(1-2\sin^2\theta_{S2}) & -\rho_2V_{S2}\sin 2\theta_{S2} \end{bmatrix}$$

$$B = \begin{bmatrix} \sin\theta_1 & \cos\theta_{S1} & -\sin\theta_2 & -\cos\theta_{S2} \\ \cos\theta_1 & -\sin\theta_{S1} & \cos\theta_2 & -\sin\theta_{S2} \\ 2\rho_1V_{S1}\sin\theta_{S1}\cos\theta_1 & \rho_1V_{S1}(1-2\sin^2\theta_{S1}) & 2\rho_2V_{S2}\sin\theta_{S2}\cos\theta_2 & \rho_2V_{S2}(1-2\sin^2\theta_{S2}) \\ \rho_1V_{P1}(1-2\sin^2\theta_{S1}) & -\rho_1V_{S1}\sin 2\theta_{S1} & -\rho_2V_{P2}(1-2\sin^2\theta_{S2}) & \rho_2V_{S2}\sin 2\theta_{S2} \end{bmatrix}$$

Equation D. 3

Since most of the time in reflection seismology, we are interested in the reflection and transmission coefficients in incidence case, Aki & Richards explicitly presented the Zoeppritz solutions for incidence (Equation D.4).

$$\dot{P}\dot{P} = R_{PP} = \left[\left(b \frac{\cos\theta_1}{V_{P1}} - c \frac{\cos\theta_2}{V_{P2}} \right) F - \left(a + d \frac{\cos\theta_1}{V_{P1}} \frac{\cos\theta_{S2}}{V_{S2}} \right) Hp^2 \right] / D$$

$$\dot{P}\dot{S} = R_{PS} = \left[-2 \frac{\cos\theta_1}{V_{P1}} \left(ab + cd \frac{\cos\theta_2}{V_{P2}} \frac{\cos\theta_{S2}}{V_{S2}} \right) pV_{P1} \right] / (V_{S1}D)$$

$$\begin{aligned}
\hat{S}\hat{P} = R_{SP} &= -2 \frac{\cos \theta_{S1}}{V_{S1}} \left(ab + cd \frac{\cos \theta_2 \cos \theta_{S2}}{V_{P2} V_{S2}} \right) p V_{S1} / (V_{P1} D) \\
\hat{S}\hat{S} = R_{SS} &= - \left[\left(b \frac{\cos \theta_{S1}}{V_{S1}} - c \frac{\cos \theta_{S2}}{V_{S2}} \right) E - \left(a + d \frac{\cos \theta_2 \cos \theta_{S1}}{V_{P2} V_{S1}} \right) G p^2 \right] / D \\
\hat{P}\hat{P} = T_{PP} &= 2\rho_1 \frac{\cos \theta_1}{V_{P1}} F V_{P1} / (V_{P2} D) \\
\hat{P}\hat{S} = T_{PS} &= 2\rho_1 \frac{\cos \theta_1}{V_{P1}} H p V_{P1} / (V_{S2} D) \\
\hat{S}\hat{P} = T_{SP} &= -2\rho_1 \frac{\cos \theta_{S1}}{V_{S1}} G p V_{S1} / (V_{P2} D) \\
\hat{S}\hat{S} = T_{SS} &= 2\rho_1 \frac{\cos \theta_{S1}}{V_{S1}} E V_{S1} / (V_{S2} D)
\end{aligned}$$

where,

$$\begin{aligned}
a &= \rho_2(1 - 2 \sin^2 \theta_{S2}) - \rho_1(1 - 2 \sin^2 \theta_{S1}) \\
b &= \rho_2(1 - 2 \sin^2 \theta_{S2}) + 2\rho_1 \sin^2 \theta_{S1} \\
c &= \rho_1(1 - 2 \sin^2 \theta_{S1}) + 2\rho_2 \sin^2 \theta_{S2} \\
d &= 2(\rho_2 V_{S2}^2 - \rho_1 V_{S1}^2) \\
D &= EF + GHp^2 = \det(A) / (V_{P1} V_{P2} V_{S1} V_{S2}) \\
E &= b \frac{\cos \theta_1}{V_{P1}} + c \frac{\cos \theta_2}{V_{P2}} \\
F &= b \frac{\cos \theta_{S1}}{V_{S1}} + c \frac{\cos \theta_{S2}}{V_{S2}} \\
G &= a - d \frac{\cos \theta_1 \cos \theta_{S2}}{V_{P1} V_{S2}} \\
H &= a - d \frac{\cos \theta_2 \cos \theta_{S1}}{V_{P2} V_{S1}} \\
p &= \text{ray parameter}
\end{aligned}$$

Equation D. 4

Although this equation provides as true reflection coefficient as possible, they do not give an explanation how the rock properties impact the reflectivity (Simm & Bacon 2014). In techniques such as AVO analysis which is a beneficial technique to analyze the petroleum systems, Zoeppritz equations are not straightforward to implement (Simm & Bacon 2014, Mavko et al. 2009). Several authors have tried to simplify the Zoeppritz equations. One of the famous explanations of Zoeppritz equation is the approximation presented by Aki & Richards 1980. They successfully proved that considering the weak contrast in the layers, the Zoeppritz equations are dependent on the contrasts in V_p , V_s and ρ (Mavko et al. 2009). The approximation is in Equation D.5

$$\begin{aligned}
R_{PP}(\theta) &\approx \frac{1}{2} \left(1 - 4\rho^2 \bar{V}_S^2\right) \frac{\Delta\rho}{\bar{\rho}} + \frac{1}{2 \cos^2 \theta} \frac{\Delta V_P}{\bar{V}_P} - 4 p^2 \bar{V}_S^2 \frac{\Delta V_S}{\bar{V}_S} \\
R_{PS}(\theta) &\approx -\frac{p \bar{V}_P}{2 \cos \theta_S} \left[\left(1 - 2\bar{V}_S^2 p^2 + 2\bar{V}_S^2 \frac{\cos \theta \cos \theta_S}{\bar{V}_P \bar{V}_S}\right) \frac{\Delta\rho}{\bar{\rho}} - \left(4 p^2 \bar{V}_S^2 - 4 \bar{V}_S^2 \frac{\cos \theta \cos \theta_S}{\bar{V}_P \bar{V}_S}\right) \frac{\Delta V_S}{\bar{V}_S} \right] \\
R_{SP}(\theta) &\approx \frac{\cos \theta_S}{\bar{V}_P} \frac{\bar{V}_S}{\cos \theta} R_{PS}(\theta) \\
R_{SS}(\theta) &\approx \frac{1}{2} \left(1 - 4\rho^2 \bar{V}_S^2\right) \frac{\Delta\rho}{\bar{\rho}} + \left(\frac{1}{2 \cos^2 \theta_S} - 4 p^2 \bar{V}_S^2\right) \frac{\Delta V_S}{\bar{V}_S} \\
T_{PP}(\theta) &\approx 1 - \frac{1 \Delta\rho}{2 \bar{\rho}} + \left(\frac{1}{2 \cos^2 \theta} - 1\right) \frac{\Delta V_P}{\bar{V}_P} \\
T_{PS}(\theta) &\approx \frac{\rho \bar{V}_P}{2 \cos \theta_S} \left[\left(1 - 2\bar{V}_S^2 p^2 - 2\bar{V}_S^2 \frac{\cos \theta \cos \theta_S}{\bar{V}_P \bar{V}_S}\right) \frac{\Delta\rho}{\bar{\rho}} - \left(4 p^2 \bar{V}_S^2 + 4 \bar{V}_S^2 \frac{\cos \theta \cos \theta_S}{\bar{V}_P \bar{V}_S}\right) \frac{\Delta V_S}{\bar{V}_S} \right] \\
T_{SP}(\theta) &\approx -\frac{\cos \theta_S}{\bar{V}_P} \frac{\bar{V}_S}{\cos \theta} T_{PS}(\theta) \\
T_{SS}(\theta) &\approx 1 - \frac{1 \Delta\rho}{2 \bar{\rho}} + \left(\frac{1}{2 \cos^2 \theta_S} - 1\right) \frac{\Delta V_S}{\bar{V}_S}
\end{aligned}$$

where,

$$\begin{aligned}
\theta &= \frac{(\theta_2 + \theta_1)}{2}, \theta_S = \frac{(\theta_{S2} + \theta_{S1})}{2} \\
\bar{\rho} &= \frac{(\rho_2 + \rho_1)}{2}, \Delta\rho = \rho_2 - \rho_1 \\
\bar{V}_P &= \frac{(V_{P2} + V_{P1})}{2}, \Delta V_P = V_{P2} - V_{P1} \\
\bar{V}_S &= \frac{(V_{S2} + V_{S1})}{2}, \Delta V_S = V_{S2} - V_{S1} \\
& p - \text{ray parameter}
\end{aligned}$$

Equation D. 5

This work has proved how the rock properties contrasts have an influence on resulting reflectivity or transmissivity. The approximation is valid for pre-critical angles. Also, the angle θ is often approximated to θ_1 , P-wave incidence angle. Since, generally, P-wave reflectivity is our interest, for better visualization, the Aki-Richards approximation for R_{PP} can be written as:

$$R_{PP}(\theta) \approx \frac{1}{2} \left(\frac{\Delta\rho}{\bar{\rho}} + \frac{\Delta V_P}{\bar{V}_P} \right) + \left[\frac{\Delta V_P}{2\bar{V}_P} - 2 \left(\frac{\bar{V}_S}{\bar{V}_P} \right)^2 \left(\frac{\Delta\rho}{\bar{\rho}} + \frac{2\Delta V_S}{\bar{V}_S} \right) \right] \sin^2 \theta + \frac{\Delta V_P}{2\bar{V}_P} \sin^2 \theta \tan^2 \theta$$

which is in the form of:

$$R_{PP}(\theta) \approx R_0 + G \sin^2 \theta + C \sin^2 \theta \tan^2 \theta$$

where,

$$R_0 = \frac{1}{2} \left(\frac{\Delta\rho}{\bar{\rho}} + \frac{\Delta V_P}{\bar{V}_P} \right) - \textit{intercept}$$

$$G = \frac{\Delta V_P}{2\bar{V}_P} - 2 \left(\frac{\bar{V}_S}{\bar{V}_P} \right)^2 \left(\frac{\Delta\rho}{\bar{\rho}} + \frac{2\Delta V_S}{\bar{V}_S} \right) - \textit{gradient}$$

$$C = \frac{\Delta V_P}{2\bar{V}_P} - \textit{curvature}$$

Equation D. 6

The main assumptions:

- Weak layer contrast approximation: $\frac{\Delta\rho}{\bar{\rho}}, \frac{\Delta V_P}{\bar{V}_P}, \frac{\Delta V_S}{\bar{V}_S} \ll 1$
- Incidence, reflection, transmission angles are real and not near 90° (pre-critical angles)

The intercept term represents zero-angle reflection coefficient (Equation D.7), while the gradient term describes the variation in intermediate offsets/angles and introduces the effect of shear velocity at non-zero angle. The third term defines the curvature of the amplitude response near to critical angles (Simm & Bacon 2014). In the case of small angles, the curvature term can be neglected.

$$R_0 = \frac{AI_{P2} - AI_{P1}}{AI_{P2} + AI_{P1}} \approx \frac{\Delta AI_P}{AI_P} \approx \frac{1}{2} \left(\frac{\Delta\rho}{\bar{\rho}} + \frac{\Delta V_P}{\bar{V}_P} \right)$$

Equation D. 7

This form of the Aki-Richards equation enables us to analyze the reflectivity in terms of different angles. Additionally, it has shown that the first intercept term is dependent on zero-offset acoustic impedance, and the gradient term is controlled by V_P/V_S .

The Aki-Richards approximation of Zoeppritz equations in Equation D.6 assumes only isotropic medium contrasts, thus, in order to perform AVO analysis in anisotropic media, the expression should be modified by considering anisotropy. Rüger 1997 and Rüger 2001 modifies the Aki-Richards approximation by introducing δ and ε contrasts. In the case of SH-wave incidence, the gamma contrast will be added.

$$R_{PP}(\theta) = \frac{1}{2} \left(\frac{\Delta\rho}{\bar{\rho}} + \frac{\Delta V_P}{\bar{V}_P} \right) + \left(\frac{\Delta V_P}{2\bar{V}_P} - 2 \left(\frac{\bar{V}_S}{\bar{V}_P} \right)^2 \left(\frac{\Delta\rho}{\bar{\rho}} + \frac{2\Delta V_S}{\bar{V}_S} \right) + \frac{\Delta\delta}{2} \right) \sin^2 \theta + \left(\frac{\Delta V_P}{\bar{V}_P} + \frac{\Delta\varepsilon}{2} \right) \sin^2 \theta \tan^2 \theta$$

Equation D. 8

References

1. Aki, K. and Richards, P.G. (1980) Quantitative Seismology. Theory and Methods, Vol. I and II. W.H. Freeman, San Francisco.
2. Alexandrov, K. S., and T. V. Ryzhova, 1961, Elastic properties of rock-forming minerals —II: Layered silicates: Izvestiya Academy of Sciences USSR, Geophysics Series, 9, 1165–1168.
3. Alkhalifah, T., and Rampton, D., 2001, Seismic anisotropy in Trinidad: A new tool for lithology prediction, *The Leading Edge*, 20, 420-424.
4. Alkhalifah, T., Tsvankin, I. 1995. Velocity Analysis for Transversely Isotropic Media. *Geophysics*, 60, 1550-1566. doi: [10.1190/1.1443888](https://doi.org/10.1190/1.1443888)
5. Armstrong, P., Ireson, D., Chmela B., Dodds, K., Esmersoy, C., Miller D., et al., 1994. Promise of Elastic Anisotropy. *Oilfield Rev. Schlumberger* 8, 36-47
6. Asaka, M. 2018. Anisotropic AVO: Implications for reservoir characterization. *The Leading Edge* 37: 916–923. doi: [10.1190/le37120916.1](https://doi.org/10.1190/le37120916.1)
7. Backus, G. E. 1962. Long-wave elastic anisotropy produced by horizontal layering: *J. Geophys. Res.*, 67, 4427-4440.
8. Banik, N. C., 1984, Velocity anisotropy of shales and depth estimation in the North Sea basin: *Geophysics*, 49, 1411–1419. doi: [10.1190/1.1441770](https://doi.org/10.1190/1.1441770)
9. Batzle, M., Wang, Z., 1992. Seismic properties of pore fluids. *Geophys.*, 57, 1396–1408.
10. Bhuiyan M., Holt R., 2016. Anisotropic parameters of dry and saturated sand under stress. *Geophysics*, Vol. 81, No. 5 (September-October 2016); P. C229–C241, doi:[10.1190/Geo2015-0354.1](https://doi.org/10.1190/Geo2015-0354.1)
11. Bortfeld, R., 1961. Approximation to the reflection and transmission coefficients of plane longitudinal and transverse waves. *Geophys. Prospecting*, 9, 485–503. doi: [10.1111/j.1365-2478.1961.tb01670.x](https://doi.org/10.1111/j.1365-2478.1961.tb01670.x)
12. Brandt, H., 1955. A study of the speed of sound in porous granular media. *J. Appl. Mech.*, 22, 479–486. doi: [10.1115/1.4011140](https://doi.org/10.1115/1.4011140)

13. Byun, B. S., Corrigan, D., and Gaiser, J. E., 1989, Anisotropy velocity analysis for lithology discrimination: *Geophysics*, 54, 1564–1574. doi: [10.1190/1.1442624](https://doi.org/10.1190/1.1442624)
14. Campbel A, Wakeman S, Fryer A. 2005. Vertical seismic profiles more than just a corridor stack. *The Leading Edge*, July, P. 694-697. doi: [10.1190/1.1993259](https://doi.org/10.1190/1.1993259)
15. Carter, A., J., Caceres, V., Duffaut, K., Stovas, A. 2020. Velocity-attenuation model from check-shot drift trends in North Sea well data. *Geophysics*. 2020, 85 (2), D65-D74. doi: [10.1190/geo2019-0419.1](https://doi.org/10.1190/geo2019-0419.1)
16. Castagna J., P. Swan H., W. 1997. Principles of AVO crossplotting. *The Leading Edge* 16: 337-344. doi:
17. Castagna, J. P. 1993. Petrophysical imaging using AVO. *The Leading Edge* 12: 172-178. doi: [10.1190/1.1436939](https://doi.org/10.1190/1.1436939)
18. Chapman, C. H., and Pratt, R. G., 1992, Traveltime tomography in anisotropic media, -I. Theory: *Geophys. J. Int.*, 109, 1–19.
19. Clavier C, Hoyle W, Meunier D. 1971. Quantitative interpretation of thermal neutron decay time logs: part I. Fundamentals and techniques. *J Petrol Technol* 23(6):743–755. <https://doi.org/10.2118/2658-A-PA>
20. Cruts, H. M. A., Groenenboom, J., Duijndam, A. J. W., and Fokkema, J.T., 1995. Experimental verification of stress-induced anisotropy. Expanded Abstracts, Soc. Expl. Geophys., 65th Annual International Meeting, pp. 894–897.
21. Daley, P. F., and Hron, F., 1977. Reflection and transmission coefficients for transversely isotropic media: *Bull., Seis. Soc. Am.*, 67,661-675.
22. Dillon, P.B, Thomson, R.C. 1984. Offset source VSP surveys and their image reconstruction. *Geophysical Prospecting* 32, P. 790-811. doi: [10.1111/j.1365-2478.1984.tb00739.x](https://doi.org/10.1111/j.1365-2478.1984.tb00739.x)
23. Duffaut K, Holt R., M. 2021. Amplitude versus Offset/Angle. *Reservoir Seismics*. Available at: ntnu.blackboard.com/
24. Duffaut, K., Alsos, T., Landrø, M., Rognø, H., Al-Najjar, N.F., 2000. Shear-wave elastic impedance. *Leading Edge*, 19, 1222–1229. doi: [10.1190/1.1438510](https://doi.org/10.1190/1.1438510)
25. Duffaut, K., Landrø, M., Sollie, R. 2010. Using Mindlin theory to model friction-dependent shear modulus in granular media. *Geophysics* 75: E143-E152. doi: [10.1190/1.3429998](https://doi.org/10.1190/1.3429998)
26. Dvorkin, J., Nur, A., 1996. Elasticity of high-porosity sandstones: Theory for two North Sea data sets. *Geophysics* 61: 1363-1370. doi: [10.1190/1.1444059](https://doi.org/10.1190/1.1444059)
27. Ellis, D., V., Singer, J., M. 2008. *Well Logging for Earth Scientists*. 2nd Edition, Springer, Berlin.
28. Ezekwe N. 2010. *Petroleum Reservoir Engineering Practice*. New Jersey, US: Prentice Hall.
29. Ferla, M., de Finis F., Bacenetti R. 2013. How seismic anisotropy improves the reliability of exploration DHI (AVO). *75th Conference and Exhibition, EAGE*, Extended Abstracts, doi: [10.3997/2214-4609.20130019](https://doi.org/10.3997/2214-4609.20130019).
30. Galybin, K, Dahlhaus, L. 2013. Walkaway VSP - Going beyond imaging. *ASEG Extended Abstracts*, 2013:1, 1-3, doi: [10.1071/ASEG2013ab119](https://doi.org/10.1071/ASEG2013ab119)
31. Gardner, G. H. F., Gardner, L.W., Gregory, A.R. 1974. Formation velocity and density – the diagnostic basics for stratigraphic traps. *Geophys.*, 39, 770–780. doi: [10.1190/1.1440465](https://doi.org/10.1190/1.1440465)
32. Gassmann, F., 1951. Über die Elastizität poröser Medien. *Vier. der Natur. Gesellschaft Zürich*, 96, 1–23.
33. Grechka, V. I. 2009. Applications of seismic anisotropy in the oil and gas industry. Houten, Netherlands: European Association of Geoscientists & Engineers EAGE.
34. Greenberg, M.L., Castagna, J.P. 1992. Shear-Wave Velocity Estimation in Porous Rocks: Theoretical Formulation, Preliminary Verification and Applications. *Geophysical Prospecting*, 40:195-209. doi: [10.1111/j.1365-2478.1992.tb00371.x](https://doi.org/10.1111/j.1365-2478.1992.tb00371.x)
35. Gretener P. 2003. AVO and Poisson's ratio. *The Leading Edge* 22: 70-72. doi: [10.1190/1.1888165](https://doi.org/10.1190/1.1888165)
36. Gretener, P. E. 1994. Reflections on the Keck Visiting Professorship at Colorado School of Mines and the interdisciplinary Dialog: TLE, Vol. 13, Oct., 1022-1026. *The Leading Edge* 13: 1022-1026. doi: [10.1190/1.1436990](https://doi.org/10.1190/1.1436990)
37. Hall M. 2015. What is anisotropy? *AgileScientific*. Feb 09. Available at: [What is anisotropy? — Agile \(agilescientific.com\)](https://www.agilescientific.com/what-is-anisotropy/)

38. Hardage, B. A. 1983. Vertical seismic profiling Part A: Principles, volume 14A, Geophysical Press, London-Amsterdam
39. Hertz, H. 1882. On the Fixed Elastic Body Contact. *Journal für die reine und angewandte Mathematik (Crelles Journal)*, 92, 156-171. doi: [10.1515/crll.1882.92.156](https://doi.org/10.1515/crll.1882.92.156)
40. Hooke, R. 1678. De Potentia Restitutiva, or of Spring. Explaining the Power of Springing Bodies, London.
41. Hornby B., Howle J., Ince D., 2003. Anisotropy correction for deviated-well sonic logs: Application to seismic well tie. *Geophysics*, Vol. 68, No. 2 (March-April 2003); P. 464–471, Doi: [10.1190/1.1567212](https://doi.org/10.1190/1.1567212)
42. Hornby, B. E., Miller, D. E., Esmersoy, C., and Christie, P. A. F., 1994, Ultrasonic-to-seismic measurements of shale anisotropy in a North Sea well: 65th Ann. Internat. Mtg., Soc. Expl. Geophys., Expanded Abstracts, 17–21.
43. Horne, S, A. 2013. A Statistical Review of Mudrock Elastic Anisotropy. *Geophysical Prospecting*, 2013, 61, 817–826 doi: [10.1111/1365-2478.12036](https://doi.org/10.1111/1365-2478.12036)
44. Johnston, J. E., and Christensen, N. I., 1995, Seismic anisotropy of shales: *J. Geophys. Res.*, 100, 5991–6003.
45. Jones, L. E. A., and Wang, H. F., 1981, Ultrasonic velocities in cretaceous shales from the Williston Basin: *Geophysics*, 46, 288–297, doi: [10.1190/1.1441199](https://doi.org/10.1190/1.1441199)
46. Kaarsberg, E. A., 1958, Introductory studies of natural and artificial argillaceous aggregates by sound-propagation and X-ray diffraction methods: *J. Geol.*, 67, 447–472.
47. Katahara, K. W., 1996, Clay mineral elastic properties: *66th Annual International Meeting, SEG*, Expanded Abstracts, 1691–1694, doi: [10.1190/1.1826454](https://doi.org/10.1190/1.1826454).
48. Klimentos, T, Schlumberger. 2007. New Sonic Technology as an Aid in Formation Evaluation and Completion Optimization of High Angle and Horizontal wells. *SPWLA India, 1st Annual Logging Symposium*, March 19-20, 2007
49. Knott, C.G., 1899. Reflection and refraction of elastic waves, with seismological applications. *Phil. Mag.*, London, 48(64–97), 567–569.
50. La Vigne, J., Herron, M, Hertzog, R. 1994. Density-neutron interpretation in shaly sands, *SPWLA 35th Annual Logging Symposium*, Paper 1994-EEE.
51. Larionov, V. V. 1969. Radiometry of boreholes.
52. Larner, K., 1993, Dip-moveout error in transversely isotropic media with linear velocity variation in depth: *Geophysics*, 58, 1442–1453.
53. Larner, K., and Cohen, J., 1993, Migration error in transversely isotropic media with linear velocity variation in depth: *Geophysics*, 58, 1454–1467.
54. Leaney, W.S, Schlumberger E.P. 1990. Parametric wavefield decomposition and applications. *SEG Technical Program Expanded Abstracts*: 1097-1100. doi: [10.1190/1.1889919](https://doi.org/10.1190/1.1889919)
55. Leslie, J.M., and Lawton, D.C., 1999, A refraction-seismic field study to determine the anisotropic parameters of shale, *Geophysics*, 64, 1247-1252, doi: [10.1190/1.1444631](https://doi.org/10.1190/1.1444631)
56. Li Y., Pickford S., 2002. Anisotropic well logs and their applications in seismic analysis. *SEG Int'l Exposition and 72nd Annual Meeting*, Salt Lake City, Utah. October 6-11, 2002. doi:[10.1190/1.1817216](https://doi.org/10.1190/1.1817216)
57. Li, Y. 2006. An empirical method for estimation of anisotropic parameters in clastic rocks. *The Leading Edge*. 25. 706-711. doi: [10.1190/1.2210052](https://doi.org/10.1190/1.2210052)
58. Li, Y.Y, Xu, Y., 2001, Utilizing conventional well logs to predict anisotropic information: A feasibility study, CSEG convention, Calgary.
59. Liner, C., Fei, T, W. 2006. Layer-induced seismic anisotropy from full-wave sonic logs: Theory, application, and validation. *Geophysics*, Vol. 71, No. 6 _November-December 2006_; P. D183–D190, doi: [10.1190/1.2356997](https://doi.org/10.1190/1.2356997)
60. Lo, T., Coyner, K. B., and Toksoz, M. N., 1989, Experimental determination of elastic anisotropy of Berea Sandstone, Chicopee shale and Chelmsford Granite, in Nur A., and Wang, Z., Eds., *Seismic and acoustic velocities in reservoir ricks: Soc. Expl. Geophys.*, 391–398.

61. Lockner, D.A., Walsh, J.B., Byerlee, J.D., 1977. Changes in velocity and attenuation during deformation of granite. *J. Geophys. Res.*, 82, 5374–5378. doi: [10.1029/JB082i033p05374](https://doi.org/10.1029/JB082i033p05374)
62. Lu, K., Chesnokov, M., E., 2015. Determination of the angle of cutting samples and C13 for VTI rocks. *SEG New Orleans Annual Meeting*. 2015. doi: [10.1190/segam2015-5867797.1](https://doi.org/10.1190/segam2015-5867797.1)
63. Lyons, L. 1991. *A Practical Guide to Data Analysis for Physical Science Students*. Cambridge: Cambridge University Press
64. Mavko, G., T. Mukerji, and J. Dvorkin, 2009, *The rock physics handbook*: Cambridge University Press, doi: [10.1017/CBO9780511626753](https://doi.org/10.1017/CBO9780511626753)
65. McDonal, F. J., Angona, F. A., Mills, R. L., Sengbush, R. L., van Nostrand, R. G., and White, J. E., 1958, Attenuation of shear and compressional waves in Pierre Shale: *Geophysics*, 23, 421–439, doi: [10.1190/1.1438489](https://doi.org/10.1190/1.1438489)
66. McNeil, L. E., and M. Grimsditch, 1993, Elastic moduli of muscovite mica: *Journal of Physics: Condensed Matter*, 5, 1681–1690, doi: [10.1088/0953-8984/5/11/008](https://doi.org/10.1088/0953-8984/5/11/008).
67. Melaku M. 2007. *Velocity Anisotropy of shales and sandstones from core sample and well log on the Norwegian Continental shelf*. Master's thesis. University of Oslo. Available at: www.duo.uio.no/handle/10852/12475
68. Miller, D. E., and Chapman, C. H., 1991, Incontrovertible evidence of anisotropy in crosswell data: 61st Ann. Internat. Mtg. Soc. Expl.Geophys., Expanded Abstracts, 825–828.
69. Miller, D.E, Spencer C 1994. An exact inversion for anisotropic moduli from phase slowness data, *J. Geophys. Res.*, 99 (B11), 21651– 21657, doi: [10.1029/94JB01848](https://doi.org/10.1029/94JB01848)
70. Mindlin, R.D., 1949. Compliance of elastic bodies in contact. *J. Appl. Mech.*, 16, 259–268. doi: [10.1115/1.4009973](https://doi.org/10.1115/1.4009973)
71. Naghiyev R, 2021. A review of models for wellbore elastic anisotropy analysis. Specialization Project. Norwegian University of Science and Technology (NTNU)
72. Norris, A. 1990. The speed of a tube wave. *The Journal of the Acoustical Society of America* 87, 414. doi: [10.1121/1.399262](https://doi.org/10.1121/1.399262)
73. NPD n.d. *NPD Factpages*. Available at: [Wellbore: 7220/8-1 - Factpages - NPD](http://Wellbore:7220/8-1-Factpages-NPD)
74. Nur, A. and Simmons, G., 1969a. Stress-induced velocity anisotropy in rocks: an experimental study. *J. Geophys. Res.*, 74, 6667. doi: [10.1029/JB074i027p06667](https://doi.org/10.1029/JB074i027p06667)
75. Okorie, I. P. C, Ebeniro J.O, Ehirim C, N. 2016. Anisotropy and Empirical Relations for the Estimation of Anisotropy Parameters in Niger Delta Depobelts. *International Journal of Geosciences*, 2016, 7, 345-352, doi: [10.4236/ijg.2016.73027](https://doi.org/10.4236/ijg.2016.73027)
76. Paive, M. F. B, Lupinacci, W. M, Freire A. F. M, Hansford J. 2019. Comparison of methodologies to estimate the clay content – A case study in the Roncador Field, Campos Basin. *16th International Congress of the Brazilian Geophysical Society*. Rio de Janeiro, Brazil. Available at: www.sbgf.org.br/mysbgf/Paiva
77. Pervukhina, M., Rasolofosaon N., J., P. 2017. Compaction Trend Versus Seismic Anisotropy in Shaly Formations. *Geophysical Prospecting*, 2017, 65, 1351–1365, doi: [10.1111/1365-2478.12486](https://doi.org/10.1111/1365-2478.12486)
78. Poisson, S.D. 1829. Mémoire sur l'équilibre et le Mouvement des Corps élastiques. *Mémoires de l'Académie Royal des Sciences de l'Institut de France*, 8, 357-570.
79. Postma, C. W., 1955. Wave propagation in stratified media, *Geophysics*, 20,780-806.
80. Pratt, R. G., and Chapman, C. H., 1992, Travelttime tomography in anisotropic media, -II. Application: *Geophys. J. Int.*, 109, 20–37.
81. Raven, M., Piane, C., Dewhurst, D., Siggins, A., 2011. Stress-induced anisotropy in brine saturated shale. *Geophys. J. Int.* 2011. 184, 897–906, doi: [10.1111/j.1365-246X.2010.04885.x](https://doi.org/10.1111/j.1365-246X.2010.04885.x)
82. Reuss, A. 1929. Berechnung der Fließgrenze von Mischkristallen auf Grund der Plastizitätsbedingung für Einkristalle. *Zeitschrift für Angewandte Mathematik und Mechanik*. 9: 49–58. doi: [10.1002/zamm.19290090104](https://doi.org/10.1002/zamm.19290090104).
83. Riznichenko, Yu.V., 1949. On seismic quasi-anisotropy. *Izvestiya USSR Akad. Sci., Ser. Geogr. and Geophys.*, No. 6, 518–543.

84. Robinson E., A., Treidel, S. 2008. Digital Imaging and Deconvolution. Chapter 7. *Society of Exploration Geophysicist SEG*. doi: [10.1190/1.9781560801610.ch7](https://doi.org/10.1190/1.9781560801610.ch7)
85. Ross, C. P., Kinman, D. L., 1995. Nonbright-spot AVO: Two examples. *Geophysics*, 60, no. 5, 1398–1408, doi: [10.1190/1.1443875](https://doi.org/10.1190/1.1443875)
86. Rothbauer, R., 1971, Untersuchung eines 2M1-muskovits mit neutronenstrahlen: Neues Jahrbuch für Mineralogie Monatshefte, 4, 143–154.
87. Rüger, A., 1997. P-wave reflection coefficients for transversely isotropic models with vertical and horizontal axis of symmetry. *Geophys.*, 62, 713–722. doi: <https://doi.org/10.1190/1.1444181>
88. Rüger, A., 2001. Reflection Coefficients and Azimuthal AVO Analysis in Anisotropic Media. Tulsa, OK: *Society of Exploration Geophysicists*
89. Rutherford, S.R, Williams, R.H. 1989. Amplitude-versus-Offset Variations in Gas Sands. *Geophysics*, 54, 680-688. doi: [10.1190/1.1442696](https://doi.org/10.1190/1.1442696)
90. Ryan – Grigor S. 1997. Empirical relationships between transverse isotropy parameters and Vp/Vs: Implications for AVO. *Geophysics* 1997 62 (5): 1359–1364, doi: [10.1190/1.1444239](https://doi.org/10.1190/1.1444239)
91. Ryan-Grigor S. 1998. Empirical relationships between anellipticity and Vp/Vs in shales: Potential applications to AVO studies and anisotropic seismic processing. *SEG Expanded Abstracts* 17, 208, doi: [10.1190/1.1820372](https://doi.org/10.1190/1.1820372)
92. Sams, M., Annamalai A. 2018. Inversion in a VTI medium: 88th Annual International Meeting. *SEG, Expanded Abstracts*, 436–440. doi: [10.1190/segam2018-2995238.1](https://doi.org/10.1190/segam2018-2995238.1).
93. Sayers, C. 1994. Elastic Anisotropy of Shales. *Journal Of Geophysical Research*, Vol. 99, No. B1, Pages 767-774, *American Geophysical Union*. 1994. doi: [10.1029/93JB02579](https://doi.org/10.1029/93JB02579)
94. Sayers, C., den Boer, L. 2016. The elastic anisotropy of clay minerals. *Geophysics*, Vol. 81, No. 5 (September-October 2016); P. C193–C203, doi: [10.1190/Geo2016-0005.1](https://doi.org/10.1190/Geo2016-0005.1)
95. Sayers, C., den Boer, L. 2019. The impact of different clay minerals on the anisotropy of clay matrix in shale. *Geophysical Prospecting*, 2019 doi: [10.1111/1365-2478.12829](https://doi.org/10.1111/1365-2478.12829)
96. Sayers, C., Den Boer, L. 2020. Effect Of Variations in Microstructure on Clay Elastic Anisotropy. *Geophysics*, Vol. 85, No. 2 (March-April 2020); P. Mr73–Mr82, doi: [10.1190/Geo2019-0374.1](https://doi.org/10.1190/Geo2019-0374.1)
97. Sayers, C.M., Van Munster, J.G., King, M.S., 1990. Stress-induced ultrasonic anisotropy in Berea sandstone. *Int. J. Rock Mech. Mining Sci. Geomech. Abstracts*, 27, 429–436. doi: [10.1016/0148-9062\(90\)92715-Q](https://doi.org/10.1016/0148-9062(90)92715-Q)
98. Schlumberger 2005. Sonic Scanner. Schlumberger. [Sonic Scanner \(slb.com\)](https://www.slb.com)
99. Schlumberger 2006. Elemental Capture Spectroscopy. Schlumberger. [ECS Elemental Capture Spectroscopy \(slb.com\)](https://www.slb.com)
100. Schlumberger 2012. Walk – away VSP processing & Anisotropic Estimation. [confidential]
101. Schlumberger Oilfield Glossary n.d. Neutron porosity. Available at. [neutron porosity | Oilfield Glossary \(slb.com\)](https://www.slb.com)
102. Schlumberger Oilfield Glossary n.d. Walk – away vertical seismic profiling. Available at. [walkaway vertical seismic profile | Oilfield Glossary \(slb.com\)](https://www.slb.com)
103. Shuey, R.T., 1985. A simplification of the Zoeppritz equations. *Geophys.*, 50, 609–614. doi: [10.1190/1.1441936](https://doi.org/10.1190/1.1441936)
104. Simm, R., and Bacon, M. 2014. Rock properties and AVO. In *Seismic Amplitude: An Interpreter's Handbook* (pp. 58-109). Cambridge: Cambridge University Press. doi: [10.1017/CBO9780511984501.006](https://doi.org/10.1017/CBO9780511984501.006)
105. Smith, G.C. and Gidlow, P.M., 1987. Weighted stacking for rock property estimation and detection of gas. *Geophys. Prospect.*, 35, 993–1014. doi: [10.1111/j.1365-2478.1987.tb00856.x](https://doi.org/10.1111/j.1365-2478.1987.tb00856.x)
106. Steiber RG., 1973. Optimization of shale volumes in open hole logs. *Jour Pet Tech* 31: pp. 147–162.
107. Suarez-Rivera R. and Bratton T. 2009. Estimating Horizontal Stress from Three-Dimensional Anisotropy. US

108. Thomsen, L. 1986. Weak elastic anisotropy. *Geophysics*, Vol. 51, No. 10 (October 1986); P. 1954-1966. doi: [10.1190/1.1442051](https://doi.org/10.1190/1.1442051).
109. Thomsen, L. 1990. Poisson was not a geophysicist! *The Leading Edge* 9: 27-29. doi: [10.1190/1.1439706](https://doi.org/10.1190/1.1439706)
110. Thomsen, L. 1996. Poisson was not a rock physicist, either! *The Leading Edge* 15: 852-855. doi: [10.1190/1.1437382](https://doi.org/10.1190/1.1437382)
111. Thomsen, L. 2014. Understanding Understanding Seismic Anisotropy in Exploration and Exploitation. 2nd edition, SEG. doi: [10.1190/1.9781560803270.fm](https://doi.org/10.1190/1.9781560803270.fm)
112. Tosaya, C. A., 1982, Acoustical properties of clay-bearing rocks: Ph.D.thesis, Stanford University.
113. Tosaya, C., and Nur, A., 1989, Effects of diagenesis and clays on compressional velocities in rocks, in Nur, A., and Wang, Z., Eds., Seismic and acoustic velocities in reservoir rocks: Soc. Expl. Geophys., 116-119. doi: [10.1029/GL009i001p00005](https://doi.org/10.1029/GL009i001p00005)
114. Vaughan, M. T., and S. Guggenheim, 1986, Elasticity of muscovite and its relationship to crystal structure: *Journal of Geophysical Research: Solid Earth*, 91, 4657-4664, doi: [10.1029/JB091iB05p04657](https://doi.org/10.1029/JB091iB05p04657).
115. Vernik, L., and Liu, X., 1997, Velocity anisotropy in shales: A petrophysical study, *Geophysics*, 62, 521-532, doi: [10.1190/1.1444162](https://doi.org/10.1190/1.1444162)
116. Vernik, L., and Nur, A., 1992, Ultrasonic velocity and anisotropy of hydrocarbon source rocks: *Geophysics*, 57, 727-735, doi: [10.1190/1.1443286](https://doi.org/10.1190/1.1443286)
117. Voigt, W. 1889. Ueber die Beziehung zwischen den beiden Elasticitätsconstanten isotroper Körper. *Annalen der Physik*. 274: 573-587. doi: [10.1002/andp.18892741206](https://doi.org/10.1002/andp.18892741206)
118. Walton, K., 1987. The effective elastic moduli of a random packing of spheres. *J. Mech. Phys. Solids*, 35, 213-226. doi: [10.1016/0022-5096\(87\)90036-6](https://doi.org/10.1016/0022-5096(87)90036-6)
119. Wang, Z. 2001, Seismic anisotropy in sedimentary rocks, SEG Expanded Abstracts.
120. Wang, Z. 2002. Seismic anisotropy in sedimentary rocks, part 2: Laboratory data. *Geophysics* 67(5), 1423-1440, doi: [10.1190/1.1512743](https://doi.org/10.1190/1.1512743).
121. White, J. E., Martineau-Nicoletis, L., and Monash, C., 1989, Measured anisotropy in Pierre Shale, in Nur, A., and Wang, Z., Eds., Seismic and acoustic velocities in reservoir rocks: Soc. Expl. Geophys., 374-390, doi: [10.1111/j.1365-2478.1983.tb01081.x](https://doi.org/10.1111/j.1365-2478.1983.tb01081.x)
122. Winterstein, D. F., and Paulsson, B. N. P., 1990, Velocity anisotropy in shale determined from cross hole seismic and vertical seismic profile data: *Geophysics*, 55, 470-479, doi: [10.1190/1.1442856](https://doi.org/10.1190/1.1442856)
123. Yan, F., Han, D., Sil, S., Chen, X. 2016. Analysis of Seismic Anisotropy Parameters for Sedimentary Strata *Geophysics*, Vol. 81, No. 5 (September-October 2016); P. D495-D502. [10.1190/Geo2016-0062.1](https://doi.org/10.1190/Geo2016-0062.1)
124. Yin, H., 1992. *Acoustic Velocity and Attenuation of Rocks: Isotropy, Intrinsic Anisotropy, and Stress-Induced Anisotropy*. Ph.D. dissertation, Stanford University. Available at: pangea.stanford.edu/departments/geophysics/Yin
125. Zamora, M., Poirier, J.P., 1990. Experimental study of acoustic anisotropy and birefringence in dry and saturated Fontainebleau sandstone. *Geophys.*, 55, 1455-1465.
126. Zoeppritz, K., 1919. Erdbebenwellen VIII B, On the reflection and propagation of seismic waves. *Göttinger Nachr.*, I, 66-84.

